NUMERICAL SOLUTION TO KINEMATIC WAVE EQUATION FOR SURFACE RUNOFF ANALYSIS USING SATELLITE BASED DEM DATA

A THESIS SUBMITTED TO
THE GRADUATE SCHOOL OF NATURAL AND APPLIED SCIENCES
OF
MIDDLE EAST TECHNICAL UNIVERSITY

BY

HASAN HÜSEYİN YILDIRIM

IN PARTIAL FULFILLMENT OF THE REQUIREMENTS
FOR
THE DEGREE OF MASTER OF SCIENCE
IN
CIVIL ENGINEERING

SEPTEMBER 2020

Approval of the thesis:

NUMERICAL SOLUTION TO KINEMATIC WAVE EQUATION FOR SURFACE RUNOFF ANALYSIS USING SATELLITE BASED DEM DATA

submitted by **HASAN HÜSEYİN YILDIRIM** in partial fulfillment of the requirements for the degree of **Master of Science** i**n Civil Engineering, Middle East Technical University** by,

Prof. Dr. Halil Kalıpçılar
Dean, Graduate School of **Natural and Applied Sciences** _____

Prof. Dr. Ahmet Türer
Head of the Department, **Civil Engineering** _____

Prof. Dr. İsmail Aydın
Supervisor, **Civil Engineering, METU** _____

Examining Committee Members:

Prof. Dr. Zuhal Akyürek
Civil Engineering, METU _____

Prof. Dr. İsmail Aydın
Civil Engineering, METU _____

Prof. Dr. Mete Köken
Civil Engineering, METU _____

Assoc.Prof. Dr. Ender Demirel
Civil Engineering, Eskişehir Osmangazi University _____

Assoc.Prof. Dr. Elif Oğuz
Civil Engineering, METU _____

Date: 23.09.2020

I hereby declare that all information in this document has been obtained and presented in accordance with academic rules and ethical conduct. I also declare that, as required by these rules and conduct, I have fully cited and referenced all material and results that are not original to this work.

Name, Last name : Hasan Hüseyin Yıldırım

Signature :

ABSTRACT

NUMERICAL SOLUTION TO KINEMATIC WAVE EQUATION FOR SURFACE RUNOFF ANALYSIS USING SATELLITE BASED DEM DATA

Yıldırım, Hasan Hüseyin
Master of Science, Civil Engineering
Supervisor : Prof. Dr. Ismail Aydın

September 2020, 133 pages

Modeling of rainfall runoff over large catchment areas is a critical step in flood analysis to estimate the time-wise variation of discharge at the outlet of hydrological basin. Outlet hydrograph of a basin is generally estimated using empirical formulations based on measurements from previous rainfall events. However, these empirical methods may not correctly model the surface flow dynamics over large and complex geometries. In this study, a fully distributed numerical model is developed that can deal with various flow conditions in natural domains. A structured computational grid is constructed on a Digital Elevation Model (DEM) that is derived from satellite data using appropriate transformations. The numerical algorithm switches between central and up-wind differencing to accurately simulate surface flow, accumulation around barriers and ponding inside cavities. Some numerical anomalies in regions of large bed slope were detected and cure is obtained in the code development stage. The code is optimized for parallel processing in multi-core computers which gives much faster solutions for large domains. Tests on hypothetical and natural domains are performed to validate the developed code.

Keywords: CFD, Kinematic Wave, Rainfall-Runoff, Satellite Based Data

ÖZ

UYDU KAYNAKLI VERİ KULLANILARAK YÜZEY AKIŞI ANALİZİNDE KİNEMATİK DALGA DENKLEMİNİN SAYISAL ÇÖZÜMÜ

Yıldırım, Hasan Hüseyin
Yüksek Lisans, İnşaat Mühendisliği
Tez Yöneticisi: Prof. Dr. İsmail Aydın

Eylül 2020, 133 sayfa

Taşkın analizinde, büyük toplanma alanlarındaki yüzey akışının modellenmesi ve hidrolojik havza çıkışlarındaki hidrografın zamana bağlı hesabı önemli bir rol oynamaktadır. Havza çıkış hidrografı genellikle geçmiş yağmur durumlarında yapılan ölçümleri temel alan ampirik formüller üzerinden yapılmaktadır. Fakat, ampirik hesaplamalar karmaşık ve geniş alanlardaki akış dinamiklerinin doğru modelleyemez. Bu çalışmada, doğal yüzeyler üzerinde çeşitli akış koşulları ile baş edebilen tam dağıtılmış sayısal model geliştirilmiştir. Uygun dönüşüm teknikleri kullanılarak sabit yapılandırılmış çözüm ağı uydu kaynaklı verilerden elde edilmiş olan sayısal yükseklik haritalarına yerleştirilir. Sayısal algoritmada, merkezi ve rüzgar yönlü çözümlemeleri dönüşümlü kullanılarak; yüzey akışı, engellerin etrafında birikim ve çukurluklarda göllenme durumlarının yüksek doğrulukta modellenmesi sağlanır. Yüksek eğimli bölgelerde sayısal çözümden kaynaklı sorunlar belirlenerek giderilmiştir. Büyük alanlarda yapılan çözümlerde sonuçların daha hızlı elde edilmesi için yazılım çok çekirdekli sistemlerde koşturulmak üzere optimize edilmiştir. Yazılım yapay ve doğal çözüm sahaları üzerinde test edilerek çözümler doğrulanmıştır.

Anahtar Kelimeler: HAD, Kinematik Dalga, Yağmur-Yüzey Aakımı, Uydu Kaynaklı Veri

To Future

ACKNOWLEDGMENTS

I would like to express my gratitude to Prof. Dr. Ismail Aydın. It was an honor for me to work with him. I owe this thesis to his endless support, guidance, and patience.

I also would like to thank the jury members of my thesis, Prof. Dr. Zuhal Akyürek, Prof. Dr. Mete Köken, Assoc. Prof .Dr. Ender Demirel and Assoc. Prof. Dr. Elif Oğuz for their contributions.

I would like to thank my family, friends and colleagues for their support and patience that have enabled me to complete this work.

Also, I am grateful to TUBİTAK for scholarship support. It allowed me to concentrate on study without struggling daily life financial problems.

TABLE OF CONTENTS

LIST OF TABLES

TABLES

LIST OF FIGURES

FIGURES

LIST OF SYMBOLS

Chapter 2 -3

x, y, z	spatial directions in cartesian coordinate system
u, v, w	velocity components in x, y, z directions respectively
Bx, By, Bz	body forces in x, y, z directions respectively
τ	viscous stresses
τ_0	bed shear stress
q	unit discharge
h	water depth
I	combination of all sources such as rainfall, lateral inflows and sinks
Z	bed elevation
E	energy elevation
w	water surface elevation
ρ	density
g	gravital acceleration
γ	unit weight
μ	viscosity
S_0	bed slope
S_f	friction slope
S_w	water surface slope
C_f	Chezy's friction coefficient

n	Manning's roughness
f	Darcy's friction factor
k_s	equivalent sand roughness height
D_H	hydraulic depth
R	hydraulic radius
A	crossection area
P	wetted perimeter
Re	Reynolds number
c	wave speed (celerity)
t	time
t_r	time of rain
t_c	time of concentration
t_p	time of propagation
x_w	wave location
dt	time step size in dicrete solution
dx	grid size in x direction in dicrete solution
dy	grid size in y direction in dicrete solution
Q	discharge
$\forall$	water volume
C_r	courant number
L	length
W	width

Chapter 5

a	equatorial radius (semi-major axis)
b	the polar radius (semi-minor axis)
f	flattening ratio
e^2	first eccentricity squared
e'^2	second eccentricity squared values
R	mean radius
d	distance between two points on an arc
σ	central angle of arc
φ	latitude
λ	longitude
β	reduced latitude in Lambert's Formula
θ	bearing angle
w	distance ratio in intermadiate point calculation
x	easting in rectangular coordinates
y	northing in rectangular coordinates
λ_0	longitude of central meridian in projections
φ_0	latitude of origin of rectangular coordinates in projections
x'	easting from false origin in UTM projection
y'	northing from false origin in UTM projection

CHAPTER 1

INTRODUCTION

1.1 Description of the Subject

Stream discharge is the basic parameter for most of the water resources developments and reclamation work. Discharge in natural streams may depend on many geographic, geologic and hydrologic parameters. Timewise variation of discharge at a given section of the river can be strongly related to rainfall histogram and physical characteristics of the catchment area. In general practice, engineers use empirical formulations such as hydrologic routing and unit hydrographs for estimating the outlet hydrograph of a basin. However, as flow dynamics over large and complex geometries is overcomplicated to solve with such empirical methods, accuracy of these methods is questionable. Thanks to the developed computing hardware and satellite-based data, it is possible to make a more comprehensive, multi-dimensional analysis on large areas using computational tools. Complete catchment area can be discretized using fine mesh to construct a fully distributed model for rainfall and surface runoff including source and sink terms to model phenomena such as evaporation, infiltration, groundwater recharge etc.

It is possible to consider different levels of approximation in the development of a mathematical model for the problem introduced above. There are modeling approaches in the literature (Bao et al., 2017; Fernández-Pato et al., 2016; Jia et al., 2019; Kazezyılmaz-Alhan & Medina, 2007; Singh et al., 2011, 2015) using full two-dimensional (2D) depth-averaged equations for shallow flows. The aim of such an approach is to be able to simulate all phases of flow; development of surface runoff, streamflow and flood inundations over wide flood plains. A more economical

approach may be to study the three phases of flow separately using appropriate solvers to make the problem more tractable.

1.2 Literature Review

As the problem studied in this thesis requires multidisciplinary combination of geography, hydrology, hydraulic and computer sciences, sources from these research areas are used together in the development of the computational approach proposed.

Fundamental information about hydrological simulation and analysis methods can be found from (Mu, 2013). This resource is used for understanding the basic principles in hydrological modeling.

The basic concept of wave equations are taken from (Miller, 1984). Full derivation of dynamic, gravity, diffusion and kinematic wave equations can be found at (Miller, 1984) and in this thesis the kinematic wave equation is derived, in the same manner, from momentum equation for shallow flows known as Saint-Venant equations. (Miller, 1984) indicated that the kinematic wave solution is adequate in calculation of surface flow over large areas and assumptions made in the solution are insignificant. However, in channel routing calculations, assumptions may become dominant and as water depths increase the results may diverge from the real solution.

(Chanson, 2004a; Eagleson, 1970; Henderson & M, 1966) are some fundamental books about hydrology and open channel hydraulics. (Henderson & M, 1966) is used for improvements of the mathematical model. Analytical solutions of kinematic wave equations are obtained from (Eagleson, 1970). Chezy's, Manning's, and Darcy's solutions for friction slope is obtained from (Chanson, 2004a).

(Bao et al., 2017) presented a study for two-dimensional kinematic wave solution of flood routing problem on distributed hydrological model. In this study, Kongjiapo basin in China is modeled and solved for flood simulation and forecasting. The study added five parameters for the estimation of flood peak time and peak discharge

volume. These parameters are calibrated with observations and measurements which are taken during a flood event.

(Wang et al., 2011) is a discussion paper which obtained coupled solution of Green-Ampt infiltration and two dimensional kinematic wave solution using implicit finite difference method for flood forecasting in semi-arid catchments. Kongjiapo basin in China is solved and in the solutions infiltration and surface roughness values were obtained from land cover material and topography is obtained from DEM.

(Fernández-Pato et al., 2016) obtained one and two-dimensional shallow water solutions for surface flow. Using one-dimensional models, studied three different cases for the calibration of infiltration parameters and compared the Horton and the Green-Ampt infiltration methods. Lastly, Arnás catchment in Spain is solved with calibrated infiltration parameters.

(Singh et al., 2011) obtained a two-dimensional numerical solution of shallow water equations for dam-break flow over natural terrain. In the solution a central explicit scheme is used, and Malpasset dam-break event in France is modeled.

(Singh et al., 2015) obtained numerical solution for two-dimensional surface flow using dynamic wave equations. The results are compared with diffusion and kinematic wave models and it was found that the outlet discharges from dynamic and diffusion wave solutions are similar. The method is tested with an experimental model in Niger, West Africa. Numerical solutions and observations from four different storm events are compared. Lastly, Goodwin Creek in Mississippi is modeled including Green-Ampt infiltration based on soil type and non-uniform Manning's roughness based on the land cover material. Results show that the method is appropriate for surface runoff modeling.

(Kazezyılmaz-Alhan & Medina, 2007) obtained numerical and analytical solutions of kinematic and diffusion wave equations using constant celerity for one-dimensional overland and open channel problems, and compared these numerical solutions with analytical solutions. In numerical solutions, MacCormack explicit

finite difference method is used and it is seen that the MacCormack method is excellent for a discrete solution in terms of efficiency and accuracy.

(Jia et al., 2019) obtained one and two-dimensional surface flow solutions of kinematic wave equations and compared the results to analytic solutions and experimental data. In the validation of the solver of this study, the same one-dimensional model is used and similar results are observed.

Especially in mountainous areas in temperate zone, surface runoff is majorly driven by snowmelt during the summer season and floods usually occurs during that period. Thus, depending on the physical properties of the study area, monitoring and modeling the accumulation of snowfall, and including the snowmelt in the solution may be required. (Akyürek & Şorman, 2002; Çiftçi et al., 2017; Tekeli et al., 2005) presented methods for estimating the snow coverage maps from satellite-based data. These studies show that the satellite-based snow coverage estimations are in close agreement with measurements and the satellite-based data is adequate in use for that purpose.

(Li et al., 2011) indicated that the hydrological simulations and especially surface runoff solutions in its nature can be parallelized with dynamic parallelization and domain decomposition techniques. A solution domain that contains a river network is decomposed to sub-basins to minimize the dependency of communication between decomposed areas. Using this method, in the code development stage the solver can be better parallelized to improve its ability to scale and handle larger problems efficiently. In this thesis, methods improved by (Li et al., 2011) are studied and already implemented.

The materials in (Grafarend & Krumm, 2006; Snyder, 1987; Veness, 2002) are used for geographical calculation methods and projection techniques. These calculation methods and projection techniques are discussed in chapter 5 and used in chapter 6.

(Buldur & Sarı, 2012) performed a study searching the reasons of a flood event occurred in 2010 in Çarşamba River in Konya province. In this thesis, small part of

the same study area is solved as a real case example. In future studies, the entire basin might be solved and results may be compared with the observation of (Buldur & Sarı, 2012).

1.3 Novelty

There are three phases of a flood event. The first phase is the surface flow which gets the water from the rainfall or the snowmelt and discharges to the streams. The second phase is stream flow which is the flow in natural or handmade channels. At some point, these channels may reach its maximum water level and excess water may exit from the sides of the channel which leads to the flood as the final phase. The final phase is the inundation of the flood.

This study is concentrated on the solution of the first phase. Using calculation methods, improved in this thesis, inputs for the streamflow calculations in large basins or outlet hydrographs of small basins can be prepared.

1.4 Scope of the Study

The main purpose of this thesis is to develop a computer program to estimate the time-wise variation of discharge in surface flow by numerically solving the depth-integrated kinematic wave equations for the rainfall-runoff problem. Computer codes will be developed to adopt topographic data extracted from satellite sources as Digital Elevation Model (DEM) to be used in numerical solution of the governing equations.

A two-dimensional kinematic wave solver is developed and written in Fortran language. Modeling of flow around obstructions and ponding in cavities are investigated. Numerical solutions are validated with available analytical solutions.

1.5 Arrangement of the Thesis

The mathematical model is discussed in Chapter 2. Numerical and analytical solutions for one-dimensional cases are compared and results are discussed in Chapter 3. Several two-dimensional test cases are described for testing the stability of the solver to estimate the grid size and time step size requirements.

Optimization of the solver for parallel processing is discussed in Chapter 4. A bunch of performance tests are performed to estimate the possible speedup of the parallelized solutions.

Geographical calculation and transformation methods used in the formation of the computational domain from the satellite data are presented in Chapter 5.

For the preparation of required inputs, a software is written in C# language. This software uses geographical calculation methods, image processing, and interpolation techniques, and all required inputs are prepared using this software without any outsourced software. Detailed information of this software is given in Chapter 6,

A part of the Çarşamba River basin in Konya province is solved as a real case simulation example. This real case solution is obtained to test the theoretical performance of the solver and the stability of the solver over the natural terrain. Detailed results of the solution are given in Chapter 7.

Conclusion and recommendations for future studies are given in Chapter 8.

CHAPTER 2

MATHEMATICAL MODELLING

There are two main descriptions of fluid flow, Lagrangian and Eulerian. In Eulerian description, Navier Stokes equations form a base mathematical model for most of the modern CFD applications. This model includes four equations; continuity and the three momentum equations for each spatial direction. For three dimensional solutions, these four equations must be simultaneously satisfied.

For an incompressible fluid the continuity equation is:

$$\frac{\partial u}{\partial x}+\frac{\partial v}{\partial y}+\frac{\partial w}{\partial z}=0 \tag{2.1}$$

and the momentum equations in shear stress form are:

$$\rho\left(\frac{\partial u}{\partial t}+u\frac{\partial u}{\partial x}+v\frac{\partial u}{\partial y}+w\frac{\partial u}{\partial z}\right) = \rho Bx-\frac{\partial P}{\partial x}+\left(\frac{\partial \tau_{xx}}{\partial x}+\frac{\partial \tau_{yx}}{\partial y}+\frac{\partial \tau_{zx}}{\partial z}\right) \tag{2.2}$$

$$\rho\left(\frac{\partial v}{\partial t}+u\frac{\partial v}{\partial x}+v\frac{\partial v}{\partial y}+w\frac{\partial v}{\partial z}\right) = \rho By-\frac{\partial P}{\partial y}+\left(\frac{\partial \tau_{xy}}{\partial x}+\frac{\partial \tau_{yy}}{\partial y}+\frac{\partial \tau_{zy}}{\partial z}\right) \tag{2.3}$$

$$\rho\left(\frac{\partial w}{\partial t}+u\frac{\partial w}{\partial x}+v\frac{\partial w}{\partial y}+w\frac{\partial w}{\partial z}\right) = \rho Bz-\frac{\partial P}{\partial z}+\left(\frac{\partial \tau_{xz}}{\partial x}+\frac{\partial \tau_{yz}}{\partial y}+\frac{\partial \tau_{zz}}{\partial z}\right) \tag{2.4}$$

Here P is the pressure, u, v, w are the velocity components, B_x, B_y, B_z are the body forces and τ terms are the viscous stresses in x, y, and z directions, respectively. The above equations are integrated in vertical direction for shallow flows assuming the acceleration in vertical direction is negligible. As a consequence of this assumption

hydrostatic pressure distribution is also accepted. Complete derivation of shallow water equations can be found in (Mu, 2013) and (Miller, 1984). From this point on, in this thesis, integral equations will be considered. The velocity components $u(x, y, t)$, $v(x, y, t)$ will represent depth integrated values and water depth will be shown by $h(x, y, t)$.

In flood inundation analysis, lateral extent of the flow is much larger than the vertical extent and thus, velocity in the vertical, z-direction can be ignored. By neglecting z-directional velocity, the momentum equation in z-direction could be dropped from the analysis. Then the other two components in horizontal directions are integrated over the vertical to obtain the depth-averaged flow equations. Moreover, shear stresses other than the bed shear stress are ignored in the solution.

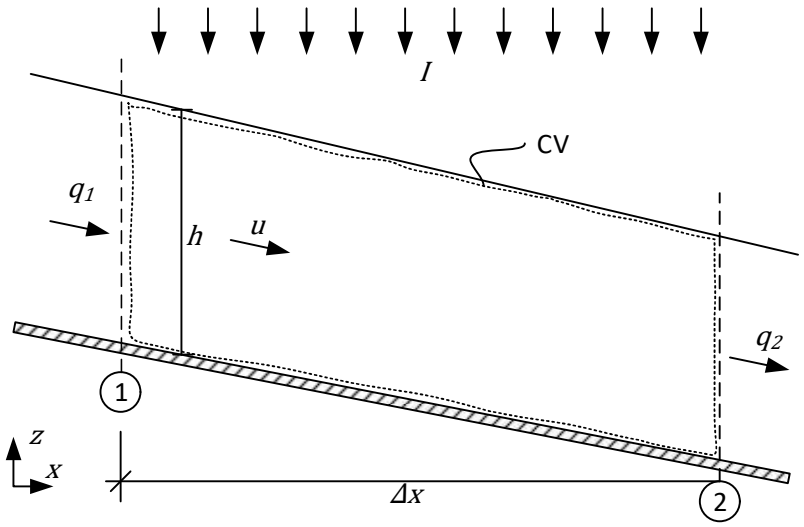

Figure 2.1 Control volume for one-dimensional flow

For the control volume shown in Figure 2.1, the rate of change of the fluid in the control volume is the difference between the inflow and the outflow rates. The depth-integrated continuity equation for such a one-dimensional flow can be written as:

$$\frac{\partial h}{\partial t} + \frac{\partial q}{\partial x} = I \tag{2.5}$$

where

$$q = hu \tag{2.6}$$

is the volume flux per unit width called as unit discharge in x-direction and *I* is the combination of all sources such as rainfall, lateral inflows and sinks such as ground infiltration, evapotranspiration etc..

The depth-integrated continuity equation can be written in two-dimensional form as:

$$\frac{\partial h}{\partial t} + \frac{\partial q_x}{\partial x} + \frac{\partial q_y}{\partial y} = I \tag{2.7}$$

For one-dimensional system, the velocity is only in x-direction and v and w are zero. For the system given in Figure 2.2, bed shear stress can be written as:

$$\frac{\tau_0}{h} = \frac{\partial \tau_{zx}}{\partial z} \tag{2.8}$$

Depth integrated momentum equation for one-dimensional flow for the system shown in Figure 2.2, can be derived from x-momentum equation (2.2):

$$\rho\left(\frac{\partial u}{\partial t} + u\frac{\partial u}{\partial x}\right) = \rho g(-s_0) - \frac{\partial P}{\partial x} + \frac{\tau_0}{h} \tag{2.9}$$

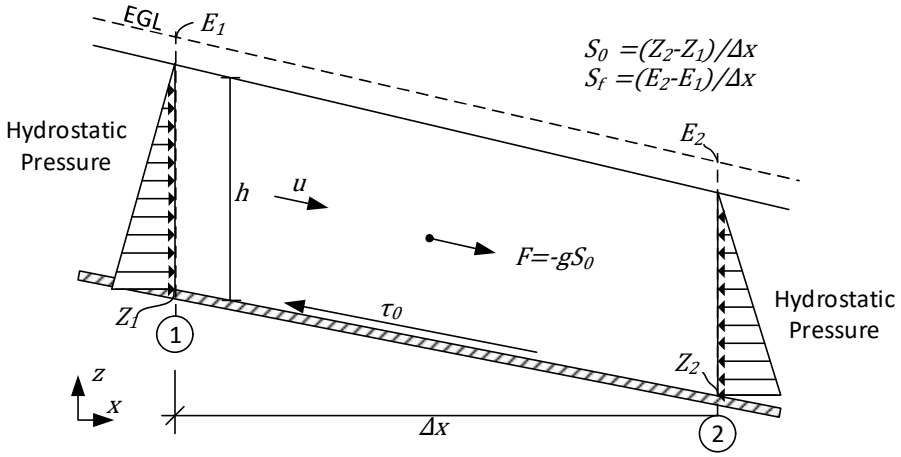

Figure 2.2 Forces on the control volume

where S_0 is the bed slope. Dividing both sides of the equation by ρg, Equation (2.9) can be put in the following form:

$$\frac{1}{g}\frac{\partial u}{\partial t}+\frac{u}{g}\frac{\partial u}{\partial x}=(-S_0)-\frac{1}{\rho g}\frac{\partial P}{\partial x}+\frac{\tau_0}{\rho g h} \tag{2.10}$$

The pressure is hydrostatic and can be found from

$$P=h\gamma=h\rho g \tag{2.11}$$

and the friction slope is directly related to the bottom shear stress, and for a wide channel it can be expressed as (Henderson & M, 1966):

$$S_f=\frac{\tau_0}{\gamma h}=\frac{\tau_0}{\rho g h} \tag{2.12}$$

Equation (2.10) can be simplified by back substitution of Equations (2.11) and (2.12).

$$\frac{1}{g}\frac{\partial u}{\partial t}+\frac{u}{g}\frac{\partial u}{\partial x}+\frac{\partial h}{\partial x}=-S_0+S_f \tag{2.13}$$

This final form is named as the Saint-Venant equation. (Miller, 1984) has derived the same equation from energy principle. All the terms are collected on the left side of the equation and re-grouped as:

$$\underbrace{\frac{1}{g}\frac{\partial u}{\partial t}}_{\text{I}}+\underbrace{\frac{u}{g}\frac{\partial u}{\partial x}}_{\text{II}}+\underbrace{\frac{\partial h}{\partial x}}_{\text{III}}+\underbrace{(S_0-S_f)}_{IV}=0 \tag{2.14}$$

In Equation (2.14), "I" is the local inertia, "II" is the convective inertia, "III" is the pressure differential and "IV" is the friction and bed slopes (Miller, 1984). The final form of the wave equation can further be simplified for different approximation levels and different wave models are obtained (Miller, 1984):

- Kinematic wave $IV=0$
- Diffusion Wave $\text{III}+IV=0$
- Steady dynamic wave $\text{II}+\text{III}+IV=0$
- Dynamic wave $\text{I}+\text{II}+\text{III}+IV=0$
- Gravity wave $\text{I}+\text{II}+\text{III}=0$

Dynamic wave model is the full form of the wave equation and it is generally used in the simulation of flood inundations as all the terms may be significant in different regions of the simulation area. However, in contrary to flood inundation, in rainfall-runoff system studied in this thesis, velocities are changing slowly and smoothly. So that the convective and local acceleration terms are relatively small values. Moreover, compared to the horizontal scale of the system the vertical scale is insignificant. Since pressure is hydrostatic and directly related to water depth, the pressure differential term can also be assumed negligible. In conclusion, the dominant terms in the momentum equation are only gravity and the bed shear stress.

While the solution of the continuity equation is the same for all wave models, there are critical differences in the equation of motion. Solution for the velocity field between nodal points requires the solution of the momentum equation, in our case, it is the simplified version named as the kinematic wave equation. The main assumption of the kinematic wave equation is the balance of the driving force of gravity and the resisting friction force resulting from the bed shear stresses. Thus, the fourth term in Equation (2.14) can be written as a balance between the bed slope, S_0, and the friction slope S_f:

$$S_0 = S_f \tag{2.15}$$

2.1 Computation of Bed Friction

Friction force for one-dimensional free surface flow can be calculated from Chezy's, Manning's, or Darcy's equation in terms of the depth-averaged velocity.

The solution of depth-averaged velocity from Chezy's equation can be written as:

$$u = C_f\sqrt{RS_0} \tag{2.16}$$

Where R is the hydraulic radius. Manning has proposed a better fit to available channel data using $R^{2/3}$ instead of $R^{1/2}$.

$$u = \frac{1}{n} R^{2/3} \sqrt{S_0} \tag{2.17}$$

and the relation between Manning's roughness n and Chezy's friction coefficient C_f are related by:

$$C_f = \frac{1}{n} R^{1/6} \tag{2.18}$$

Utilizing Equation (2.15) Manning's equation can be written in terms of friction slope:

$$u = \frac{1}{n} R^{2/3} \sqrt{S_f} \tag{2.19}$$

In our case, the solution domain can be considered as a wide channel for rainfall-runoff solution and Manning's equation can be simplified further:

$$u = \frac{1}{n} h^{2/3} \sqrt{S_f} \tag{2.20}$$

Both solutions, from the Manning's and the Chezy's equations, are based on similar assumptions, estimate empirical friction coefficients for surface materials from experiments, and the same amount of friction loss for a given velocity independent of the shape effects of the channel. (Chanson, 2004b) expressed that "*In open channels, the Darcy equation is the only sound method to estimate the friction loss. For various reasons, empirical resistance coefficients (e.g. Chézy coefficient, Gauckler–Manning coefficient) were and are still used. Their use is highly inaccurate and most improper in man-made channels. Most friction coefficients are completely empirical and they are limited to fully rough turbulent water flows.*".

In nature, modeling turbulent effects is the main step in the formulation of the flow velocity. Resultant shear forces are in direct proportion to the velocity square and hydraulic depth. As velocities and water depths are small in rainfall-runoff systems, laminar flow conditions may occur especially at the early development of the overland flow. Manning's solution is based on only a fully turbulent flow and this

assumption for surface flow changes the outflow hydrograph. As Darcy's solution includes both laminar and turbulent flow regimes, the results might be more realistic. However, in practical cases where a large flow depth occurs Manning's formula can be used due to its simplicity.

For better accuracy and especially for flow over man-made materials friction should be calculated from Darcy's formulation for better prediction. Average boundary shear stress from Darcy's friction factor can be calculated by (Chanson, 2004a):

$$\tau_0 = \frac{f}{8}\rho u^2 \tag{2.21}$$

In Darcy's solution friction slope for pipe flow defined as (Chanson, 2004a):

$$S_f = \frac{f}{8g\frac{D_H}{4}} u\,|u| \tag{2.22}$$

and the solution for averaged velocity is:

$$u = \sqrt{\frac{8g}{f}}\sqrt{\frac{D_H}{4}S_0} \tag{2.23}$$

Darcy's solution can be applied to the open channel flow similar to the pipe flow. D_H is the hydraulic diameter or equivalent pipe diameter, and it can be calculated for channel flow as (Chanson, 2004b):

$$D_H = 4R = 4\frac{A}{P} \tag{2.24}$$

For channel flow Darcy's equation can be written as:

$$u = \sqrt{R\frac{8g}{f}}\sqrt{S_0} \tag{2.25}$$

For wide channel solution Darcy's equation can be simplified further:

$$u = \sqrt{h\frac{8g}{f}}\sqrt{S_0} \tag{2.26}$$

Darcy's friction factor f is a function of Reynolds number and relative roughness and can be calculated for laminar flows by (Chanson, 2004a):

$$f = \frac{64}{Re} \quad where \;\; Re < 2x10^3 \tag{2.27}$$

Darcy's friction factor can be calculated for turbulent flow from Colebrook-White formula by (Chanson, 2004a):

$$\frac{1}{\sqrt{f}} = -2\log_{10}\left(\frac{k_S}{3.71\,D_H} + \frac{2.51}{Re\sqrt{f}}\right) \quad where\; Re > 1x10^4 \tag{2.28}$$

where k_s is the equivalent sand roughness height and Re is the Reynolds number and can be calculated by:

$$Re = \frac{\rho u D_H}{\mu} \tag{2.29}$$

Note that calculation of Darcy's friction factor in Equation (2.28) requires iterations as f appears on both sides of the equation. More explicit but less accurate calculation of Darcy's friction factor can be done by Altsul's formula (Chanson, 2004a):

$$f = 0.1\left(1.46\frac{k_s}{D_H} + \frac{100}{Re}\right)^{1/4} \quad where \quad Re > 1x10^4 \tag{2.30}$$

2.2 Analytical Solution of Kinematic Wave Model

In some special cases, the analytical solution of kinematic wave equations is available. (Eagleson, 1970) obtained analytical solutions for simple cases. Analytical solution of kinematic wave equations is only based on Manning's formula because of the simplicity. Darcy's solution is over complicated to solve analytically.

For wide channels, Manning's equation can be regrouped as:

$$q = ah^m \tag{2.31}$$

where

$$a = \frac{1}{n}\sqrt{S_0} \qquad m = \frac{5}{3} \tag{2.32}$$

By combining Equation (2.5) and Equation (2.31), the continuity equation can be written as:

$$\frac{\partial h}{\partial t} + a\frac{\partial (h^m)}{\partial x} = I \tag{2.33}$$

Using the total differential, these two equations can be added.

$$dq = \frac{\partial q}{\partial x}dx + \frac{\partial q}{\partial t}dt \tag{2.34}$$

$$dh = \frac{\partial h}{\partial x}dx + \frac{\partial h}{\partial t}dt \tag{2.35}$$

From the determinant of Equations, wave speed c (celerity) can be written as:

$$\frac{\partial x}{\partial t} = amh^{m-1} = c \tag{2.36}$$

and

$$\frac{\partial q}{\partial t} = c\frac{\partial h}{\partial t} \tag{2.37}$$

Consider an infinite duration of lateral inflow to a uniform and one-dimensional system. In this condition, water depths in the system raise in the same amount of lateral inflow. Except at the inlet of the system the discharge comes from upstream is equal to discharges at the downstream everywhere at the beginning. Water depths can be calculated by:

$$\frac{\partial h}{\partial t} = I \tag{2.38}$$

and in integral form:

$$\int_{h_0}^{h} dh = \int_{t_0}^{t} I\, dt \tag{2.39}$$

And a kinematic wave starts to propagate from inlet to downstream with wave speed c which can be calculated from Equation (2.36). Location of this kinematic wave can be found combining Equations (2.36) and (2.39) as:

$$\int_{x_0}^{x} dx = am \int_{t_0}^{t} h^{m-1}\, dt = am \int_{t_0}^{t} \left[\int_{t_0}^{t} I\, dt\right]^{m-1} dt \tag{2.40}$$

While water depths are rising at the downstream of this wave, water depths remain constant at the upstream and the discharges at the upstream can be calculated as:

$$\frac{\partial q}{\partial x} = I \tag{2.41}$$

and in integral form:

$$\int_{q_0}^{q} dq = \int_{x_0}^{x} I\, dx = Ix \tag{2.42}$$

by combining with Equation (2.31) Water depths can be calculated as:

$$h = \left(\frac{1}{a}\int_{x_0}^{x} I\, dx\right)^{1/m} = \left(\frac{Ix}{a}\right)^{1/m} \tag{2.43}$$

This integral forms must be specialized for the solution of different specific problems.

The time required for the wave to reach the outlet named as time of concentration t_c and can be calculated from the solution of Equation (2.40) using the length of the channel.

Water surface profile for $t \leq t_c$ can be calculated from Equation (2.43) for the upstream, and from Equation (2.39) for the downstream of the wave of which location x_w can be found from Equation (2.40). The system reaches the steady-state condition at $t = t_c$, water surface profile and discharges in the system remains constant until the end of the rain.

For finite duration t_r of rain, after the end of the rain, water surface profile propagates to the downstream with wave speed. Thus, if $t_r \geq t_c$, after the end of the rainfall entire surface calculated from Equation (2.43) will propagate with wave speed. The water surface profile can be calculated by inserting Equation (2.40) into Equation (2.43).

In $t_r \leq t_c$ condition, as the lateral inflow stops before the system reaches the steady-state condition, water surface profile at $t = t_r$ will propagate to the downstream. In hydrograph analysis at the outlet, although the system is not in steady-state condition, the water discharge at the outlet remains constant until the wave reaches the outlet. The time that wave reaches the outlet named as time of propagation t_p. It can be calculated from Equation (2.40).

2.2.1 Analytical Solution of Surface Runoff

The simplest model to adapt the integral form of equations is the finite duration of steady and uniform rainfall over a one-dimensional plane.

$$I = \begin{cases} I = constant & 0 \leq t \leq t_r, x \geq 0 \\ I = 0 & t < 0, t > t_r, x < 0 \end{cases} \tag{2.44}$$

Initial water depths are zero and there is no flow from the inlet.

$$h = 0 \quad at \quad \begin{matrix} 0 \leq x < L, t = 0 \\ x = 0, t > 0 \end{matrix} \tag{2.45}$$

Water surface profile at any time $t \leq t_r$ can be found from Equation (2.43) for the upstream of the wave and from Equation (2.39) for the downstream of the wave as:

$$h = \begin{cases} \left(\frac{xI}{a}\right)^{\frac{1}{m}} & 0 \leq x \leq x_w \\ I_* t & x > x_w \end{cases} \tag{2.46}$$

where x_w is the location of the wave and can be found from Equation (2.40) as:

$$x_w = am\int_0^t h^{m-1}\,dt = \frac{t^m a}{I_*^{1-m}} \tag{2.47}$$

And water surface profile at $t > t_r$ can be found from the implicit relation between final water surface profile and wave speed as:

$$x = \frac{ah^m}{I_*} + amh^{m-1}(t - t_r) = ah^{m-1}\left(hI_*^{-1} + m(t - t_r)\right) \tag{2.48}$$

At the outlet of the system, Water depth can be found from the solution of Equations (2.46) and (2.48) for $x = L$. Then, the outflow hydrograph can be calculated by solving Equation (2.31) to find the discharges.

$$\begin{Bmatrix} h_L = I_* t & ,0 \le t \le t_c \\ h_L = \left(\frac{LI_*}{a}\right)^{\frac{1}{m}} & ,t_c \le t \le t_r \\ L = ah_L^{m-1}[h_L I_*^{-1} + m(t - t_r)] & ,t > t_r \end{Bmatrix} \tag{2.49}$$

where

$$t_c = \left(\frac{LI_*^{1-m}}{a}\right)^{1/m} \tag{2.50}$$

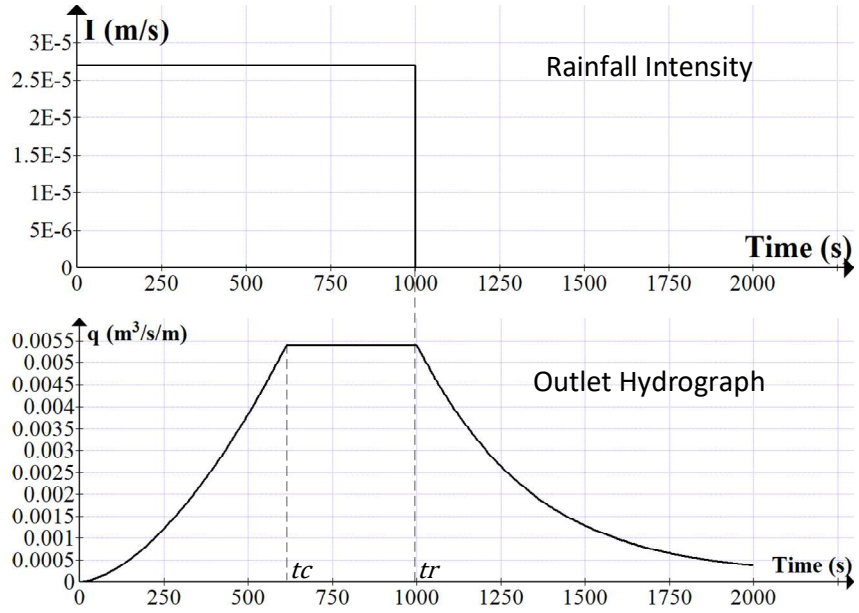

Figure 2.3 Outlet hydrograph for $tc < tr$ condition

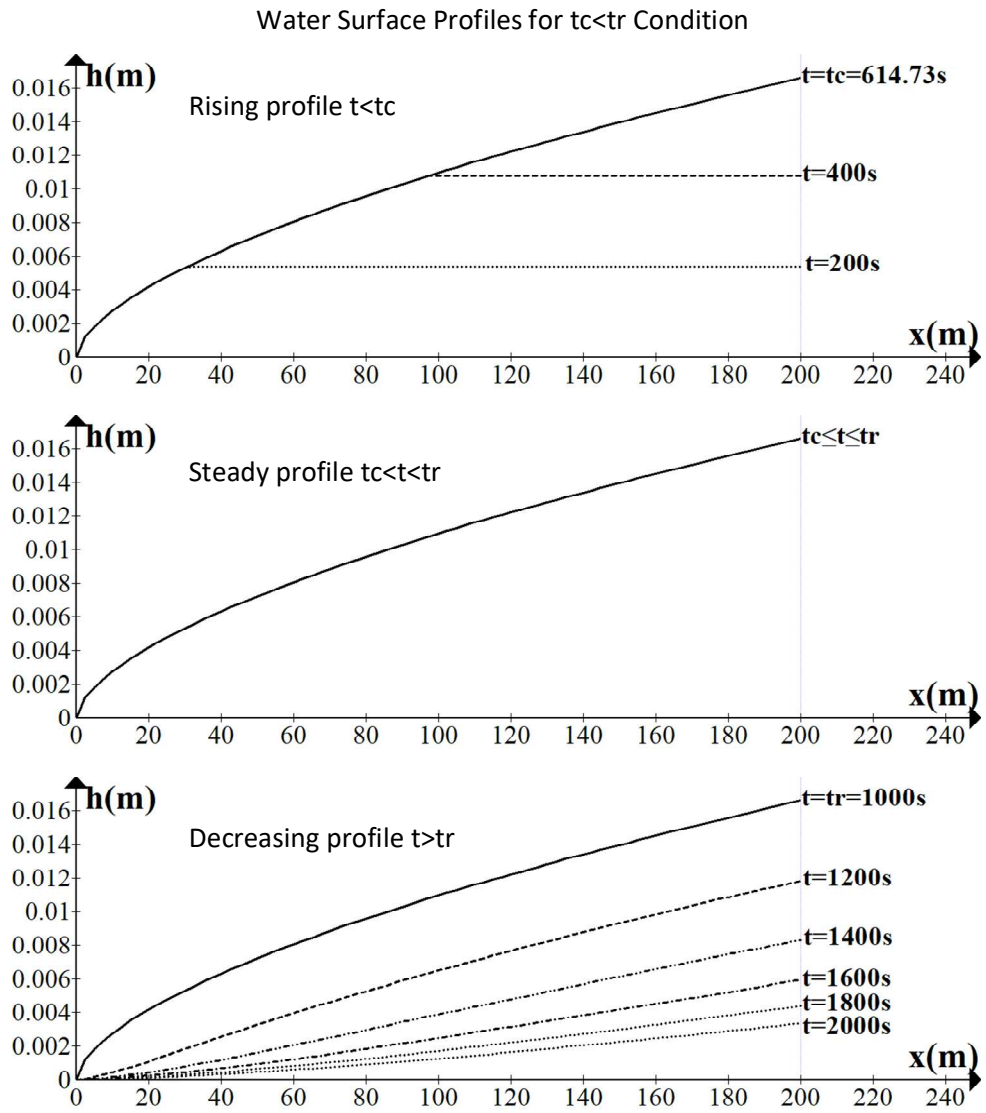

Figure 2.4 Water surface profiles for $tc < tr$ condition

If the rainfall duration is shorter than the time of concentration, the rainfall ends before the wave reaches to the outlet and decreasing profile occurs without reaching the steady-state. As the rainfall is zero at $t > t_r$, entire water surface profile at $t = t_r$ starts to propagate to the downstream after the end of the rainfall.

In this condition, water depths at the outlet can be found as:

$$\begin{Bmatrix} h_L = I_* t & , 0 \le t \le t_r \\ h_L = I_* t_r & , t_r \le t \le t_p \\ L = a h_L^{m-1}[h_L I_*^{-1} + m(t - t_r)] & , t > t_p \end{Bmatrix} \quad (2.51)$$

where

$$t_p = t_r + \frac{L - a h_{Lr}^m / I_*}{a m h_{Lr}^{m-1}} \quad (2.52)$$

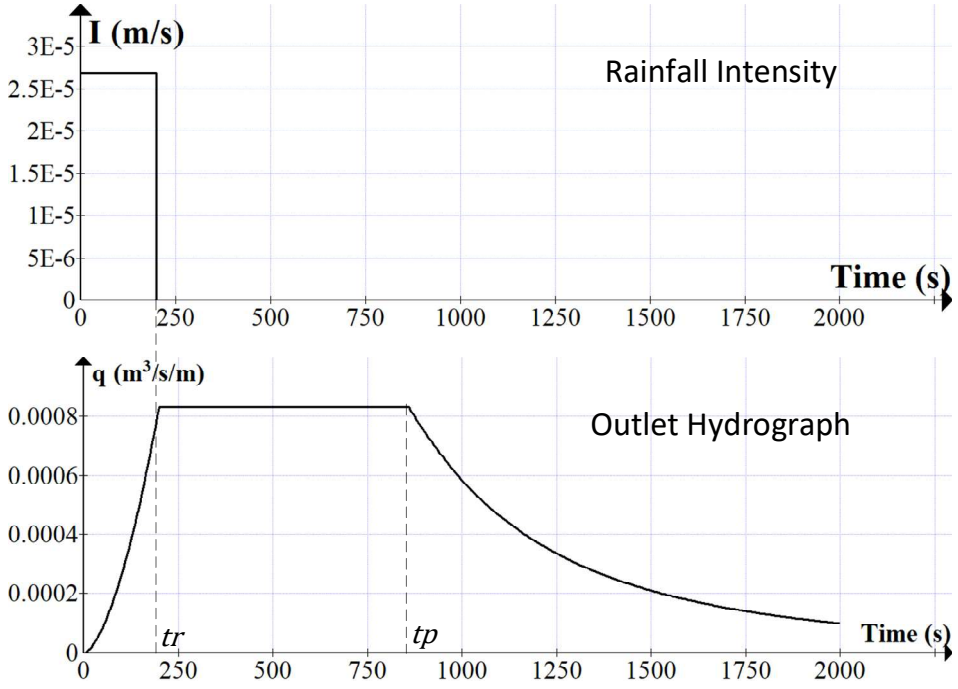

Figure 2.5 Outlet hydrograph for $tr < tc$ condition

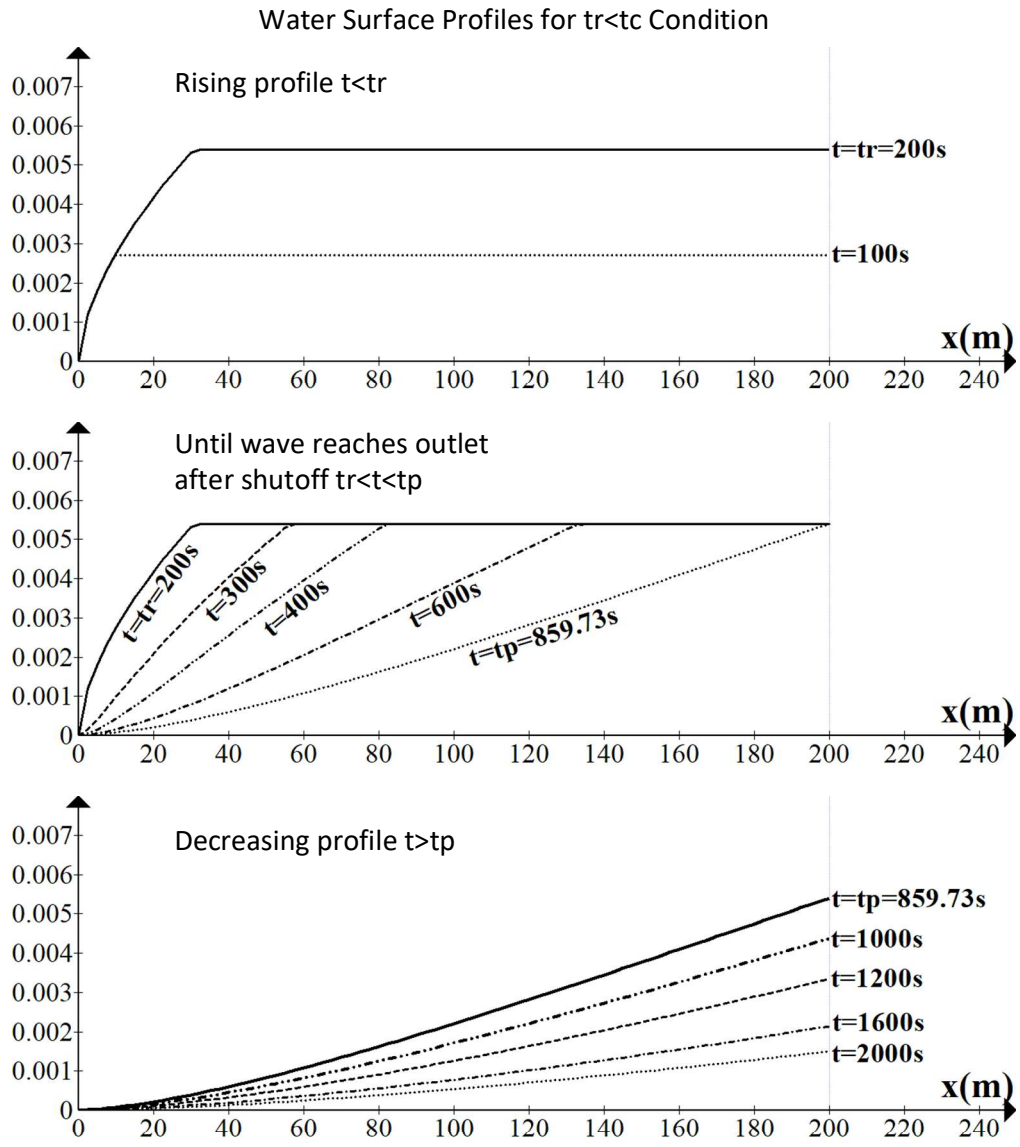

Figure 2.6 Water surface profiles for $tr < tc$ condition

2.2.2 Analytical Solution of Channel Flow

Using the same principle, analytical solution of a channel flow also can be prepared. In the scope of this thesis, channel flow solution is not studied. However, an analytical solution for channel flow can be described with similar simplification.

Continuity equation for channels can be rewritten by multiplying Equation (2.5) to the width in other horizontal direction (in y-direction) as:

$$\frac{\partial A}{\partial t} + \frac{\partial Q}{\partial x} = q_I \tag{2.53}$$

Continuity equation can be rewritten for channel flow, to apply similar simplification of Equation (2.33) as:

$$\frac{\partial A}{\partial t} + a_c \frac{\partial (A^{m_c})}{\partial x} = q_I \tag{2.54}$$

Discharge calculation from manning's equation for channel flow can be written as:

$$Q = \frac{A^{5/3}}{n\, P^{2/3}} \sqrt{S_0} \tag{2.55}$$

As wet perimeter must be written in terms of cross-section area, simplification can only be adapted to the triangular or elliptical channels. Solution for a triangular channel is shown in Figure 2.7.

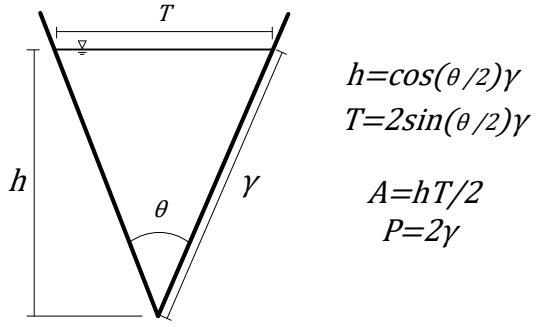

Figure 2.7 Triangular channel cross-section

P can be written in terms of A as:

$$P = 2\sqrt{\frac{2}{\sin\theta}A} \tag{2.56}$$

Thus the equation of motion can be written as:

$$Q = a_c\, A^{m_c} \tag{2.57}$$

Where

$$a_c = \frac{(\sin(\theta))^{1/3}}{2\,n}\sqrt{S_0} \qquad m_c = \frac{4}{3} \tag{2.58}$$

The solution procedure is the same as the surface flow, for uniform lateral inflow condition. The system can be solved by replacing h and q in the surface flow system with A and Q.

CHAPTER 3

NUMERICAL SOLUTION

3.1 Numerical Solution of Kinematic Wave Model

3.1.1 Numerical Solution of One-Dimensional Surface Flow

In this thesis one-dimensional solvers will be used for only validation of test cases. The computational grid for solution of one-dimensional model is given in Figure 3.1.

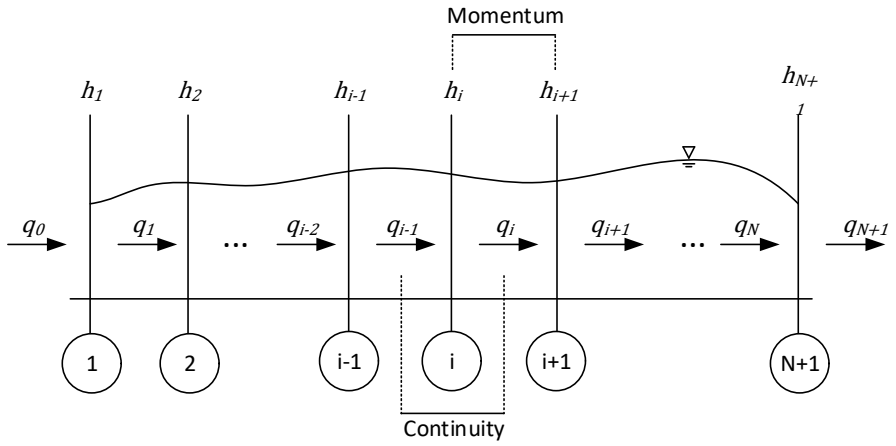

Figure 3.1 Grid structure for the one-dimensional model.

Note that, in numerical solutions, n used as superscript of the parameters indicates the time level of discretization.

For solution of one-dimensional model, the continuity equation is discretized as:

$$h_i^{n+1} = h_i^n + dt(I_i^n + (q_{i-1}^n - q_i^n)/dx) \tag{3.1}$$

For solution of kinematic wave equation, two different formulations from Darcy's and Manning's equations can be used. While the continuity equation is the same for these two methods, the solution of the equation of motion differs.

The Manning's equation is discretized for upwind method as:

$$\begin{bmatrix} u_i^n = \frac{1}{n} {h^n}_i^{2/3} \sqrt{S_i^n} \;\; and \;\; q_i^n = u_i^n \, h_i^n, & S_i^n \leq 0 \\ u_i^n = \frac{1}{n} {h^n}_{i+1}^{2/3} \sqrt{S_i^n} \;\; and \;\; q_i^n = u_i^n \, h_{i+1}^n, & S_i^n > 0 \end{bmatrix} \tag{3.2}$$

for central space method:

$$u_i^n = \frac{1}{n_{man}} \left(\frac{h_i^n + h_{i+1}^n}{2} \right)^{2/3} \sqrt{S_i^n} \;\; and \;\; q_i^n = u_i^n \, \frac{h_i^n + h_{i+1}^n}{2} \tag{3.3}$$

Numerical solution of one-dimensional model also can be obtained from Darcy's equation. However, as friction factor calculation requires iterations and as there is not an analytical solution, in practical reasons, the Darcy's discretization is prepared but solution is not obtained in the scope of this thesis.

The Darcy's equation is discretized for upwind method as:

$$\begin{bmatrix} u_i^n = \sqrt{h_i^n 8g/f_i^n} \sqrt{S_i^n} \;\; and \;\; q_i^n = u_i^n \, h_i^n, & S_i^n \leq 0 \\ u_i^n = \sqrt{h_{i+1}^n 8g/f_i^n} \sqrt{S_i^n} \; and \;\; q_i^n = u_i^n \, h_{i+1}^n, & S_i^n > 0 \end{bmatrix} \tag{3.4}$$

for central space solution:

$$u_i^n = \sqrt{\left(\frac{h_i^n + h_{i+1}^n}{2} \right) 8g/f_i^n} \sqrt{S_i^n} \;\; and \;\; q_i^n = u_i^n \, \frac{h_i^n + h_{i+1}^n}{2} \tag{3.5}$$

where f_i^n values are calculated from Equation (2.27) and (2.28) by iterating the Reynolds number values calculated from u_i^n and hydraulic depth ${D_h}_i^n$ which is approximated by $4h_i$.

Solution is obtained using the central difference and upwind methods. These two methods are compared with the analytical solutions and the differences are explained under the validation title.

As negative slope leads flow in positive direction, square root of slope must be written in solver as:

$$\sqrt{S_i} = -sign(S_i)\sqrt{abs(S_i)} \tag{3.6}$$

and as Manning's and Darcy's solutions only valid for positive water depth and non-zero slope condition. Velocity calculated for these conditions can be taken as zero.

Solution can be obtained by using bed slopes as it is used in analytical solution. However, using the bed slope, reverse flow condition, or flow in accumulation zones cannot be solved. To allow reverse flow and accumulation in local depressions, water surface slope S_w or friction slope S_f must be used.

3.1.2 Numerical Solution of One-Dimensional Channel Flow

For channel flow solution the continuity equation is discretized as:

$$A_i^{n+1} = A_i^n + dt(q_{I_i}^n + (Q_{i-1}^n - Q_i^n)/dx) \tag{3.7}$$

In channel solution, Manning's equation is discretized as:

$$\begin{bmatrix} u_i = \frac{1}{n} R_i^{2/3} \sqrt{S_{0_i}^n} \quad and \quad Q_i = u_i\, A_i, & S_{0_i}^n \le 0 \\ u_i = \frac{1}{n} R_{i+1}^{2/3} \sqrt{S_{0_i}^n} \quad and \quad Q_i = u_i\, A_{i+1}, & S_{0_i}^n > 0 \end{bmatrix} \tag{3.8}$$

for central space solution:

$$u_i = \frac{1}{n}\left(\frac{R_i + R_{i+1}}{2}\right)^{2/3} \sqrt{S_{0_i}^n} \quad and \quad Q_i = u_i\, \frac{A_i + A_{i+1}}{2} \tag{3.9}$$

In channel solution, Darcy's equation is discretized as:

$$\begin{bmatrix} u_i^n = [8g/f_i^n]^{\frac{1}{2}} * \left[S_{0_i}^n {D_{h_i}}^n/4\right]^{\frac{1}{2}} \quad and \quad Q_i = u_i\, A_i, & S_{0_i}^n \le 0 \\ u_i^n = [8g/f_i^n]^{\frac{1}{2}} * \left[S_{0_i}^n {D_{h_{i+1}}}^n/4\right]^{\frac{1}{2}} and \quad Q_i = u_i\, A_{i+1}, & S_{0_i}^n > 0 \end{bmatrix} \tag{3.10}$$

for central space solution:

$$u_i^n = [8g/f_i^n]^{\frac{1}{2}} * \left[S_{0_i}^n D_{h_i}{}^n/4\right]^{\frac{1}{2}} \quad and \;\; Q_i = u_i \, \frac{A_i + A_{i+1}}{2} \qquad (3.11)$$

In general, there is no reverse flow condition in channel flow. Thus the solution can be obtained using only bed slopes. In addition to that, as the lateral inflow is much higher than the surface flow, the Water depths are higher so that the central space solution is more applicable.

3.1.3 Numerical Solution of Two-Dimensional Surface Flow

For the solution of continuity and momentum equation different types of solution schemes are improved. As there are no dependencies between neighbor nodes, these different solution schemes can be used for different portions of the domain, or solutions schemes can be used selectively decided by the solver.

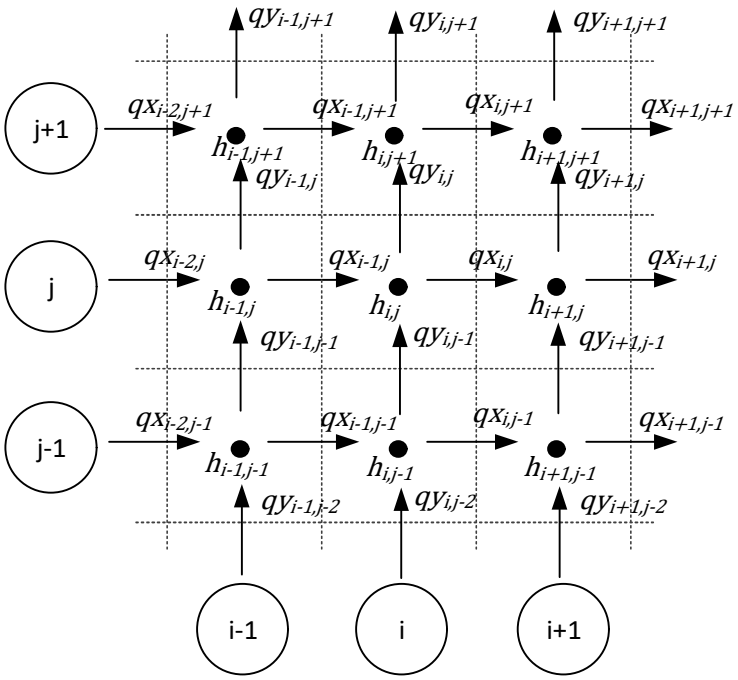

Figure 3.2 Grid structure used for the solution of two-dimensional model.

Grid structure for the solution of two-dimensional model is shown in Figure 3.2. As seen in the grid structure, water depths located at the center of the computational cells and the discharges are located at the side surfaces of the cells. Same grid structure is used in all solution schemes.

3.1.3.1 Solution of Continuity in Two-Dimensional Model

Continuity equation is discretized in various schemes. Basic solution for continuity is forward time solution which has first-order time accuracy and discretized as:

$$h_i^{n+1} = h_i^n + dt\left(I_i^n + \frac{{q_x}_{i-1,j}^{\,n} - {q_x}_{i,j}^{\,n}}{dx} + \frac{{q_y}_{i,j-1}^{\,n} - {q_y}_{i,j}^{\,n}}{dy}\right) \tag{3.12}$$

While the forward time solution for continuity can be preferred because of its computational simplicity. If unsteady effects are important in solution, higher-order time accuracies might be achieved by using time-stepping technique. This solution performs second-order accuracy in time by taking the fluxes at half time step forward for the calculation of full step, and it is discretized as:

$$h_{i,j}^{n+\frac{1}{2}} = h_{i,j}^n + \frac{dt}{2}\left[I_{i,j}^n + \frac{{q_x}_{i-1,j}^{\,n} - {q_x}_{i,j}^{\,n}}{dx} + \frac{{q_y}_{i,j-1}^{\,n} - {q_y}_{i,j}^{\,n}}{dy}\right] \tag{3.13}$$

$$h_{i,j}^{n+1} = h_{i,j}^n + dt\left[I_{i,j}^{n+1/2} + \frac{{q_x}_{i-1,j}^{\,n+\frac{1}{2}} - {q_x}_{i,j}^{\,n+\frac{1}{2}}}{dx} + \frac{{q_y}_{i,j-1}^{\,n+\frac{1}{2}} - {q_y}_{i,j}^{\,n+\frac{1}{2}}}{dy}\right] \tag{3.14}$$

For further accuracy in time, trapezoidal scheme can be used. As half of the flux term is calculated at $n+1$ level, this solution requires iteration. So that the computational cost of trapezoidal scheme is higher compared to the two-step and forward time schemes. Trapezoidal scheme solution of continuity equation discretized as:

$$F^n x_{i,j} = \frac{{q_x}_{i-1,j}^{\,n} - {q_x}_{i,j}^{\,n}}{dx} \quad and \; F^n y_{i,j} = \frac{{q_y}_{i,j-1}^{\,n} - {q_y}_{i,j}^{\,n}}{dy} \tag{3.15}$$

$$h_{i,j}^{n+1} = h_{i,j}^{n} + dt\ I_{i,j}^{n+1/2} + \frac{dt}{2}\left[Fx_{i,j} + Fy_{i,j}\right]^{n+1} + \frac{dt}{2}\left[Fx_{i,j} + Fy_{i,j}\right]^{n} \tag{3.16}$$

3.1.3.2 Solution of Momentum Equation in Two-Dimensional Model

In two-dimensional systems, the equation of motion is solved for each special direction separately. For the solution of equation of motion, Manning's equation is solved in x and y directions. Manning's equation is discretized in central space and forward upwind methods.

In central space solution velocity components and discharges are solved using water depths at sides of the nodes, which leads second-order accuracy in space. Central space solution is discretized as:

$$u_{i,j}^{n} = \frac{1}{n_{man}}\left(\frac{h_{i,j}^{n} + h_{i+1,j}^{n}}{2}\right)^{\frac{2}{3}}\sqrt{S_{x_{i,j}}^{n}}\ and\ {q_x}_{i,j}^{n} = u_{i,j}^{n}\ \frac{h_{i,j}^{n} + h_{i+1,j}^{n}}{2} \tag{3.17}$$

$$v_{i,j}^{n} = \frac{1}{n_{man}}\left(\frac{h_{i,j}^{n} + h_{i,j+1}^{n}}{2}\right)^{\frac{2}{3}}\sqrt{S_{y_{i,j}}^{n}}\ \ and\ \ {q_y}_{i,j}^{n} = v_{i,j}^{n}\ \frac{h_{i,j}^{n} + h_{i,j+1}^{n}}{2} \tag{3.18}$$

In upwind solution velocity components and discharges are solved using water depths at upstream of the nodes, which leads first-order accuracy in space. Upwind solution is discretized as:

$$\begin{bmatrix} u_{i,j}^{n} = \frac{1}{n_{man}}{h_{i,j}^{n}}^{2/3}\sqrt{S_{x_{i,j}}^{n}}\ and\ \ {q_x}_{i,j}^{n} = u_{i,j}^{n}\ h_{i,j}^{n} & ,{S_x}_{i,j}^{n} \le 0 \\ u_{i,j}^{n} = \frac{1}{n_{man}}{h_{i+1,j}^{n}}^{2/3}\sqrt{S_{x_{i,j}}^{n}}\ \ and\ \ {q_x}_{i,j}^{n} = u_{i,j}^{n}\ h_{i+1,j}^{n} & ,{S_x}_{i,j}^{n} > 0 \end{bmatrix} \tag{3.19}$$

$$\begin{bmatrix} v_{i,j}^n = \frac{1}{n_{man}} {h_{i,j}^n}^{2/3} \sqrt{{S_y}_{i,j}^n} \; and \; {q_y}_{i,j}^n = v_{i,j}^n \, h_{i,j}^n & , {S_y}_{i,j}^n \leq 0 \\ v_{i,j}^n = \frac{1}{n_{man}} {h_{i,j+1}^n}^{2/3} \sqrt{{S_y}_{i,j}^n} \; and \; {q_y}_{i,j}^n = v_{i,j}^n \, h_{i,j+1}^n & , {S_y}_{i,j}^n > 0 \end{bmatrix} \quad (3.20)$$

Calculation of slope requires the calculation of energy or water surface elevations.

Water surface elevation can be calculated as:

$$w_{i,j}^n = z_{i,j} + h_{i,j}^n \quad (3.21)$$

Total energy level can be calculated as:

$$E_{i,j}^n = z_{i,j} + h_{i,j}^n + \frac{1}{2g}\left(\left(\frac{u_{i-1,j}^n + u_{i,j}^n}{2}\right)^2 + \left(\frac{v_{i,j-1}^n + v_{i,j}^n}{2}\right)^2\right) \quad (3.22)$$

Slopes in x and y direction can be calculated from bed, water surface or total energy as:

$${S_x^n}_{i,j} = \begin{bmatrix} (z_{i+1,j} - z_{i,j})/dx & Bed\ Slope \\ (w_{i+1,j}^n - w_{i,j}^n)/dx & Surface\ Slope \\ (E_{i+1,j}^n - E_{i,j}^n)/dx & Energy\ Slope \end{bmatrix} \quad (3.23)$$

$${S_y^n}_{i,j} = \begin{bmatrix} (z_{i,j+1} - z_{i,j})/dy & Bed\ Slope \\ (w_{i,j+1}^n - w_{i,j}^n)/dy & Surface\ Slope \\ (E_{i,j+1}^n - E_{i,j}^n)/dy & Energy\ Slope \end{bmatrix} \quad (3.24)$$

3.1.3.3 Boundary Conditions

Boundary conditions are defined as cell-based conditions. So that, cells are grouped in different roles with different behaviors in calculation. Those roles can be interior (I_{cell}), wall (W_{cell}), outlet (O_{cell}) or out of calculation (X_{cell}). Wall cells are used for no inflow condition or for solid boundaries in the domain. Outlet cells are used for outlet and acts like sink. Out of calculation cells behave same as outlet cells. Different from the outlet cells, out of calculation cells are not used for the calculation

of discharges or cumulative discharge volume. Only in real case solution, it is used for boundaries other than outlet to test the performance of the catchment area algorithm.

Solution of continuity is only operated in interior cells. Water depths at wall or outlet cells are set as zero without calculation.

$$\begin{bmatrix} h_{i,j} \Rightarrow Continuity\ Eqn & , Cell_{i,j} = I_{cell} \\ h_{i,j} = 0 & , Cell_{i,j} = O_{cel} \\ h_{i,j} = 0 & , Cell_{i,j} = W_{cell} \end{bmatrix} \tag{3.25}$$

Discharges are defined depending on cell interfaces. Discharge at the interface between interior cells or between interior and outlet cell must be calculated. There is no discharge at W_{cell} faces.

In x-direction;

$$\begin{bmatrix} q_{x_{i,j}} \Rightarrow Manning's\ Eqn & , Cell_{i,j} = I_{cell}\ and\ Cell_{i+1,j} = I_{cell} \\ q_{x_{i,j}} \Rightarrow Manning's\ Eqn & , Cell_{i,j} = O_{cell}\ and\ Cell_{i+1,j} = I_{cell} \\ q_{x_{i,j}} \Rightarrow Manning's\ Eqn & , Cell_{i,j} = I_{cell}\ and\ Cell_{i+1,j} = O_{cell} \\ q_{x_{i,j}} = 0 & , Cell_{i,j} = W_{cell}\ or\ Cell_{i+1,j} = W_{cell} \end{bmatrix} \tag{3.26}$$

and in y-direction;

$$\begin{bmatrix} q_{y_{i,j}} \Rightarrow Manning's\ Eqn & , Cell_{i,j} = I_{cell}\ and\ Cell_{i,j+1} = I_{cell} \\ q_{y_{i,j}} \Rightarrow Manning's\ Eqn & , Cell_{i,j} = O_{cell}\ and\ Cell_{i,j+1} = I_{cell} \\ q_{y_{i,j}} \Rightarrow Manning's\ Eqn & , Cell_{i,j} = I_{cell}\ and\ Cell_{i,j+1} = O_{cell} \\ q_{y_{i,j}} = 0 & , Cell_{i,j} = W_{cell}\ or\ Cell_{i,j+1} = W_{cell} \end{bmatrix} \tag{3.27}$$

3.1.3.4 Calculation of Other Parameters

As the equations solved in this thesis describes a rainfall-runoff system, and inflow only comes from the rainfall, the inflow discharge can be calculated from the summation of effective inflow to interior cells as follows:

$$Q_{in}^{n} = dx * dy * \sum_{I_{cell}} I_{i,j}^{n} \tag{3.28}$$

Outflow from system only occurs at interfaces between interior and outlet cells. Outflow discharges can be calculated from the summation of discharges at interfaces between I_{cell} and O_{cell} as:

$$Q_{out}^{n} = dy * \sum_{I_{cell} \Rightarrow O_{cell}} qx_{i,j}^{n} \; + dx * \sum_{I_{cell} \Rightarrow O_{cell}} qy_{i,j}^{n} \tag{3.29}$$

Water volume in the system can be calculated from water depths at interior cells as:

$$\forall_{sys}^{n} = dx * dy * \sum_{I_{cell}} h_{i,j}^{n} \tag{3.30}$$

Cumulative inflow and cumulative outflow volumes are calculated as:

$$\forall_{in}^{n+1} = \forall_{in}^{n} + dt * Q_{in}^{n} \tag{3.31}$$

$$\forall_{out}^{n+1} = \forall_{out}^{n} + dt * Q_{out}^{n} \tag{3.32}$$

Instead of calculating residuals of h, u or v at each time step, the steady-state condition can be defined from the difference of inflow and outflow discharges or difference in change of water volume in the system.

$$Q_{in}^{n} \cong Q_{out}^{n} \;\; or \;\; \forall_{sys}^{n+1} \cong \forall_{sys}^{n} \tag{3.33}$$

Continuity can be checked as:

$$\forall_{in}^{n} \cong \forall_{out}^{n} + \forall_{sys}^{n} \tag{3.34}$$

Courant number is the main stability condition for solutions. It is calculated as:

$$C_r = \text{Max}\left(\frac{Max(|u|)\; dt}{dx}, \frac{Max(|v|)\, dt}{dy}\right) \leq 1 \tag{3.35}$$

Cr is the courant number, and it must be equal or less than one for a stable solution.

3.1.3.5 Solvers

Different types of solution schemes are prepared for the solution of the 2D models. Each scheme has advantages and disadvantages. These solution schemes are tested on complex geometries to validate stability and reliability of the solver to run on actual cases.

3.1.3.5.1 Explicit FTCS Scheme Solution

Forward time central space (FTCS) solution has second-order accuracy in space and first-order accuracy in time.

In rainfall-runoff solutions, water depths are small compared to the size of the domain. Even if the water depth is zero at the upstream, the energy slope can be negative. When central space discretization is used in the calculation, the solution may lead forward flow, and as a result of that negative water depths are observed. As the time step sizes and grid sizes decrease, the solution leads to smaller negative Water depths in magnitude. The solution requires impractically finer mesh with smaller time step sizes to solve the rainfall-runoff systems with non-negative water depths. However, as it has second-order accuracy, solutions are more stable. Especially in the rising profile, central space solution leads to more accurate results. It can be used for solutions in milder areas, local accumulation zones, channel flow or areas with higher water depths to never cause negative values in the analysis.

3.1.3.5.2 Explicit Central Space Trapezoidal Scheme Iterative Solution

Similar to the FCTS solution, velocity components are calculated from the central space solution. In this solution, the continuity equation is solved by a trapezoidal scheme to improve the time accuracy. As trapezoidal continuity equation takes half of the components from past iteration and half of the components from present

iteration, continuity equation must be iterated. In conclusion, the solution requires more computational time. It can be used for the solution of small and critical areas.

3.1.3.5.3 Explicit Forward Time Upwind Scheme Solution

Upwind solution is a flow direction dependent solution which has first-order accuracy in space and the time. Solution takes the water depths at the upstream for the calculation of velocity and discharges at the sides of the cells. In its characteristic, upwind scheme restricts negative water depths independently from the grid sizes. So that, this scheme can be used with coarser mesh. It is suitable for calculation over large domains efficiently. However, as always upstream water depths are used in the solution, in local depression zones the solution may lead dynamic instabilities, especially in coarser mesh.

3.1.3.5.4 Explicit Two-Step Up-Wind Scheme Solution

In this scheme, calculation of velocity and discharges are similar to the upwind solution. In contrary to upwind solution to achieve higher time accuracy time-stepping technique is used. Flux terms in continuity equation are taken from the half step solution to find the water depths at the full step. It leads to second-order accuracy in time.

3.1.3.5.5 Combined Solver

In order to merge the advantages of the central and the upwind solution, a combined method is improved. As there is no dependency in calculations between neighbor nodes at the same time step. Up-wind solution and central space solution can be used for different portions of the domain. In order to keep the dynamic stability of central space solution and non-negative water depth calculation of up-wind solution, if a negative Water depth condition occurs at a node, solver can correct the negative

depth calculation by using the upwind solution at discharging faces of that node. Using that method, negative depths can be filtered from central space solution.

In central space solver, after the solution of continuity equation, if $h_{i,j} < 0$ discharges at faces are corrected by replacing with upwind solution:

$$\begin{bmatrix} East\ Face & q_{x_{i,j}} = q_{upwind}{}_{x_{i,j}} & , q_{x_{i,j}} > 0 \\ West\ Face & q_{x_{i-1,j}} = q_{upwind}{}_{x_{i-1,j}} & , q_{x_{i-1,j}} < 0 \end{bmatrix}$$
$$\begin{bmatrix} North\ Face & q_{y_{i,j}} = q_{upwind}{}_{y_{i,j}} & , q_{y_{i,j}} > 0 \\ South\ Face & q_{y_{i,j-1}} = q_{upwind}{}_{y_{i,j-1}} & , q_{y_{i,j-1}} < 0 \end{bmatrix} \quad (3.36)$$

Then, the continuity equation must be resolved with corrected discharges. This process is repeated until the is no negative water depth in the domain.

It is seen from the solutions that this correction only takes place in steeper slopes or during the decreasing water profile after the end of the rain.

3.2 Validation of the Solver with One-Dimensional Models

(Jia et al., 2019) obtained simulations for rainfall-runoff systems using kinematic wave equations. The rainfall-runoff solution obtained in this thesis for the same conditions and similar results are observed. Numerical solutions are based upwind and central space methods for the solution of Manning's formula. For all solutions, Manning's roughness $n = 0.02\ (m^{-1/3}s)$, the bed slope is 0.01. All solutions are obtained for uniform and steady rain condition, rainfall intensity is $I = 2.7x10^{-5}\ m/s = 97.2\ mm/hour$. In each case, outflow hydrographs are printed out to see the unsteady effects for different conditions. For all cases, the time step size is the same and checked that the courant condition is satisfied.

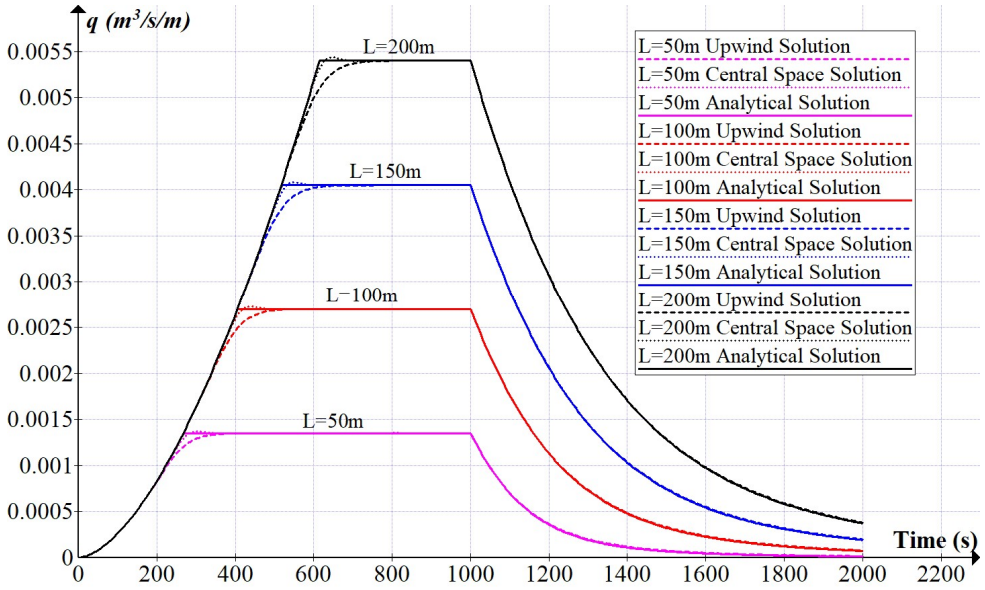

Figure 3.3 Outlet hydrograph from analytical and numerical solution of $t_r \geq t_c$ condition for different lengths. $t_r = 1000s$

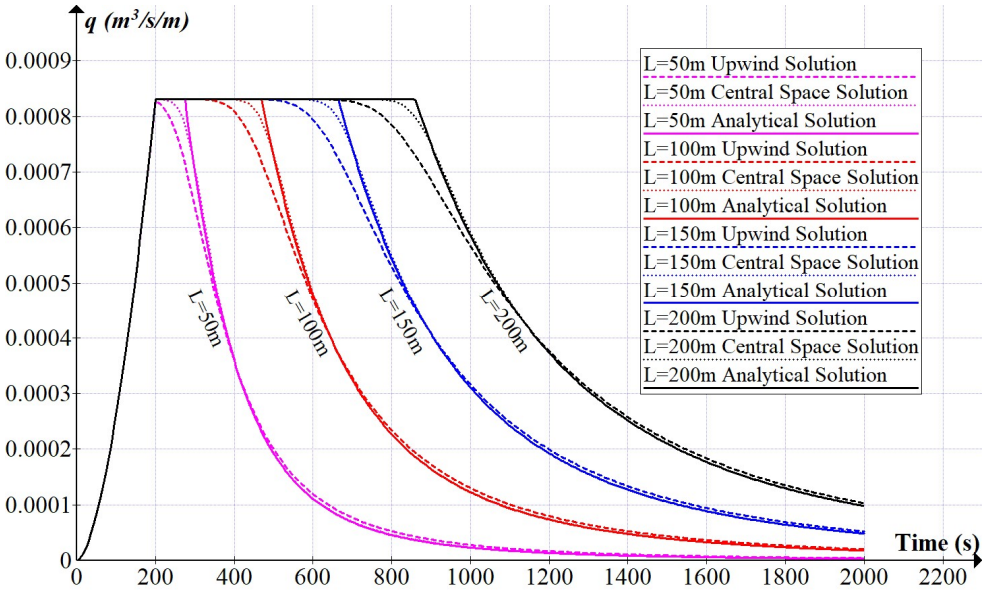

Figure 3.4 Outlet hydrograph from analytical and numerical solution of $t_r < t_c$ condition for different lengths. $t_r = 200s$

In order to test the effects of the length of the domain, outlet hydrographs for different lengths of domains are printed out for both $t_r > t_c$ and $t_r < t_c$ conditions as shown in Figure 3.3 and Figure 3.4. It is seen that the numerical solutions match with the analytical solution.

There are small differences around $t \sim t_c$ in $t_r > t_c$ condition and around $t \sim t_p$ in $t_r < t_c$ condition. As explained under the analytical solution title, the kinematic wave resulted from the inlet boundary reaches to the outlet at $t = t_c$ in $t_r > t_c$ and at $t = t_p$ in $t_r < t_c$ conditions. Thus, the difference may result from the propagation of that wave. As numerical solution methods are discrete methods, a continuous solution with an abrupt change in time or in space cannot be represented without truncation errors. For better representation, higher-order methods or finer mesh must be used.

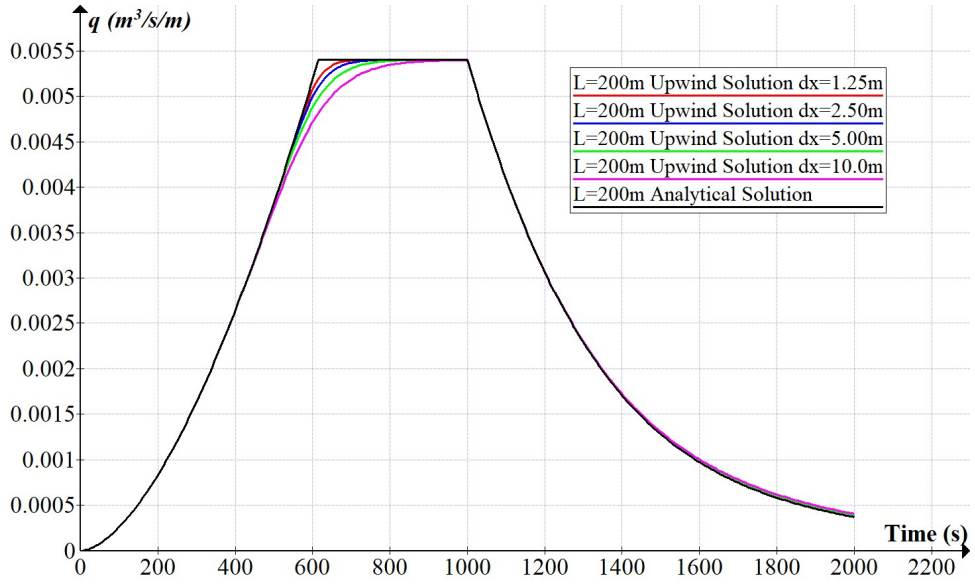

Figure 3.5 Outlet hydrograph from upwind solution for $t_r > t_c$ condition for different grid sizes. $L = 200m$ and $t_r = 1000s$.

In order to test the grid size requirement, $L = 200m$ and $t_r = 1000s$ condition is solved for different grid sizes and results are printed out in Figure 3.5 and Figure 3.6. It is seen that the grid size has an effect on the solution and finer mesh leads to more accurate results.

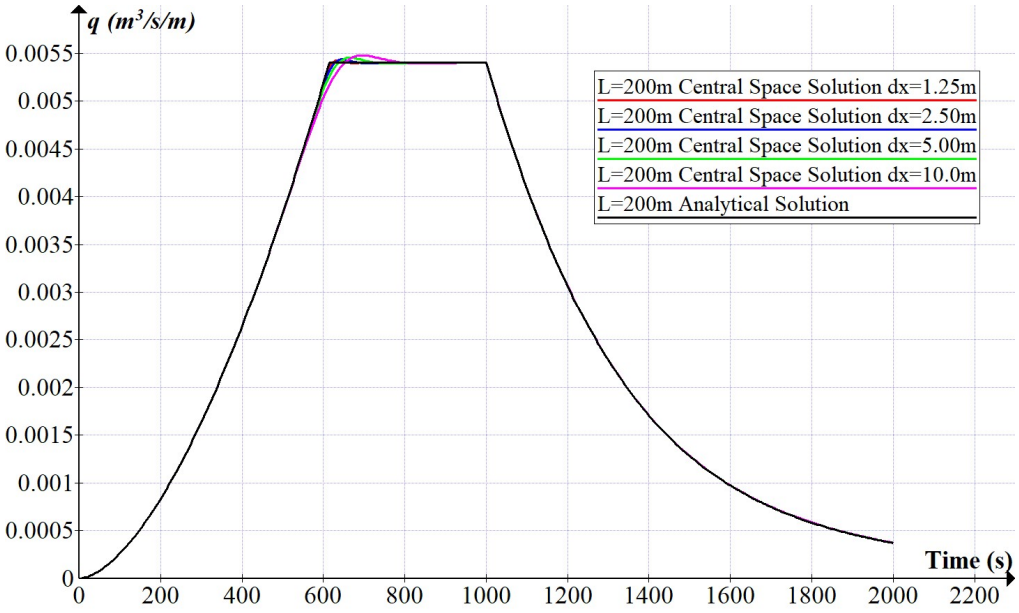

Figure 3.6 Outlet hydrograph from central space solution for $t_r > t_c$ condition for different grid sizes. L=200m and t_r=1000s.

While there is no observable difference in decreasing hydrograph, especially right before it reaches the steady-state condition the difference between analytical and numerical solutions increases.

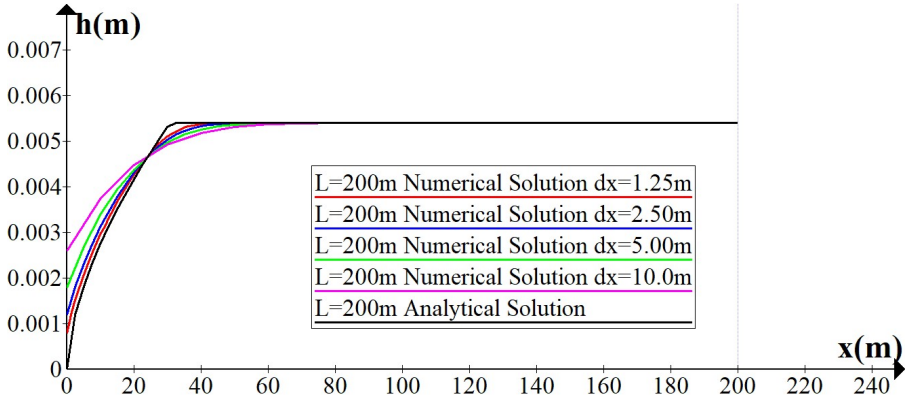

Figure 3.7 Water surface profile from analytical and upwind solutions with different mesh sizes at $t = 200s$.

As mentioned before, the difference may have resulted from the numerical solution of the wave. The wave seems to be smoothened in numerical solutions. Thus, to see the effect of the mesh sizes on water surface profile, water surface profile at $t = 200s$ is printed as shown in Figure 3.7. It is seen that the first guess was true, and this phenomenon has resulted from the discrete solution of the wave.

The error that comes from the discrete solution can be calculated from water depths for a given time as:

$$e = \frac{1}{N+1}\sum_{i=1}^{N+1}\left|h_{i_{analytic}} - h_{i_{numeric}}\right| / h_{i_{analytic}} \qquad (3.37)$$

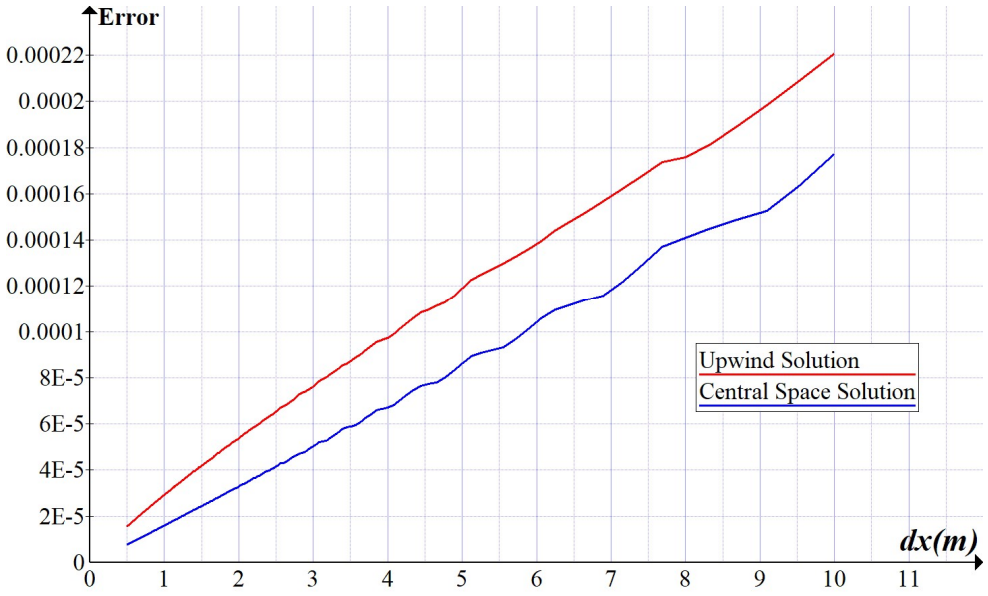

Figure 3.8 Error vs grid size. $t = 200s$, $L = 200m$

The same model has solved for different grid sizes between 0.5m and 10m at $t = 200m$ and $L = 200m$, and error values are calculated as shown in Figure 3.8. As can be seen in the figure finer solutions up to 0.5 m resulted in more accurate results and central space solution is more accurate than the upwind solution.

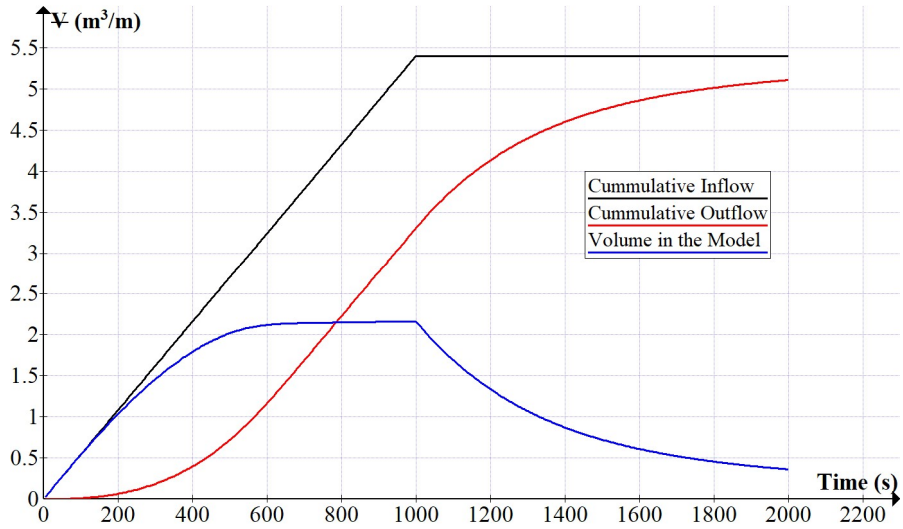

Figure 3.9 Cumulative inflow, cumulative outflow and water volume in the model. $L = 200m$ and $t_r = 1000s$.

In order to check the continuity, cumulative inflow, cumulative outflow, and water volumes in the model is checked for all cases. It is seen that the difference between inflow and summation of outflow and volume in the system is insignificant. So, the numerical solution satisfies continuity. Volumetric changes of inflow, outflow, and water in the model are printed out for one case solution from upwind method and it is shown in Figure 3.9.

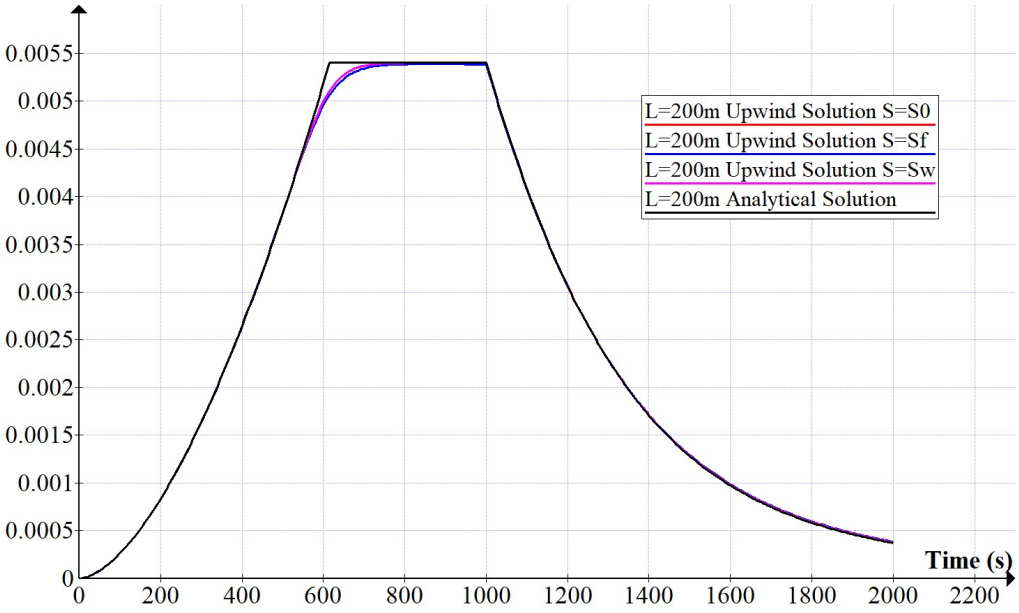

Figure 3.10 Effects of different slopes. $L = 200m$ and $t_r = 1000s$

As geometries in actual cases are complex, and possibly contains small accumulation zones or reverse flow conditions, solutions must be carried out using friction or water surface slopes. As can be seen in Figure 3.10, in order to see the effects of the usage of S_f or S_w rainfall-runoff system is solved with upwind method and based on different slope definitions. Results are clear that there is not a significant difference between numerical solutions for flow over a flat surface. However, from this comparison it cannot be said that it is valid for complex geometries, it may due to the simplicity of selected computational domain.

3.3 Test Cases

3.3.1 Test Case Geometries

General shape of the domain is given in Figure 3.11. As seen in the figure, the domain is symmetric around $y = W/2$ line, and main bed surface has two different slopes in x and y directions. The main bed surface is formed from these two slopes.

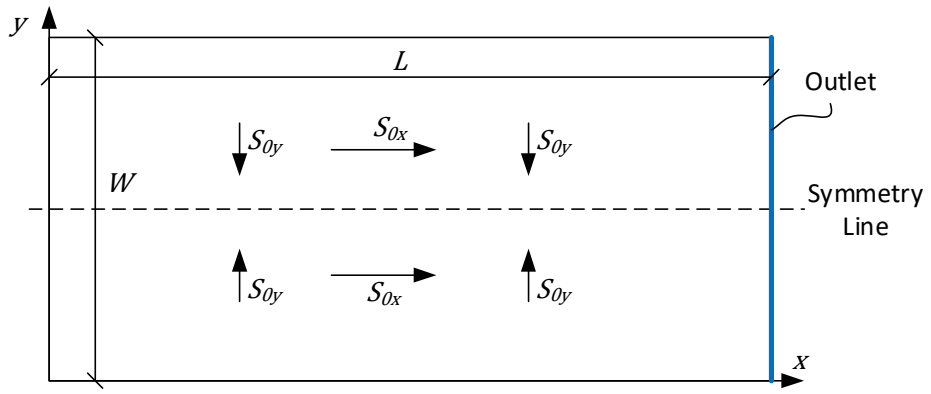

Figure 3.11 Main bed surface geometry.

The bed surface elevation without any obstacles can be calculated from:

$$Z = (L - x)S_{0x} + (|W/2 - y|)S_{0y} \tag{3.38}$$

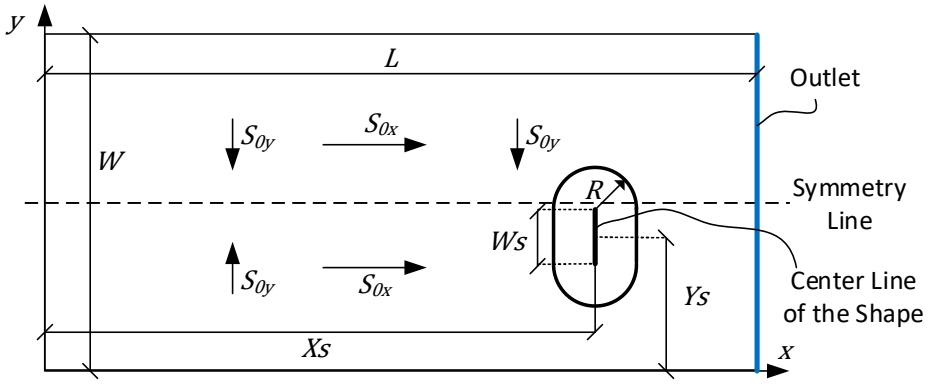

Figure 3.12 Geometry and important distances in test cases

Except the first case, obstructions having different cross-section curvatures are placed in the domain to generate complex geometries. Distance of that obstacle is in x-axis Xs, in y-axis Ys. Width of the centerline of that obstacle is Ws. If $Ws = 0$ the shape is formed around the point (Xs, Ys) as shown in Figure 3.13.

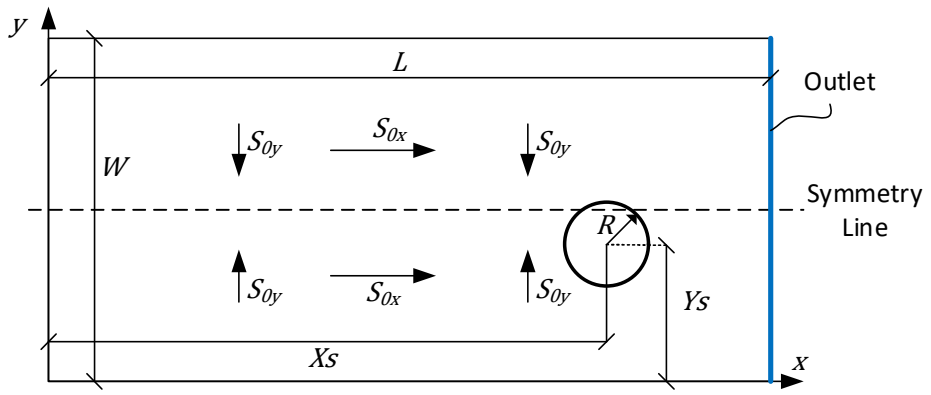

Figure 3.13 Test case geometry with $Ws = 0\ m$.

As shown in Figure 3.14 the vertical extent of these obstacles are defined with three different curvatures.

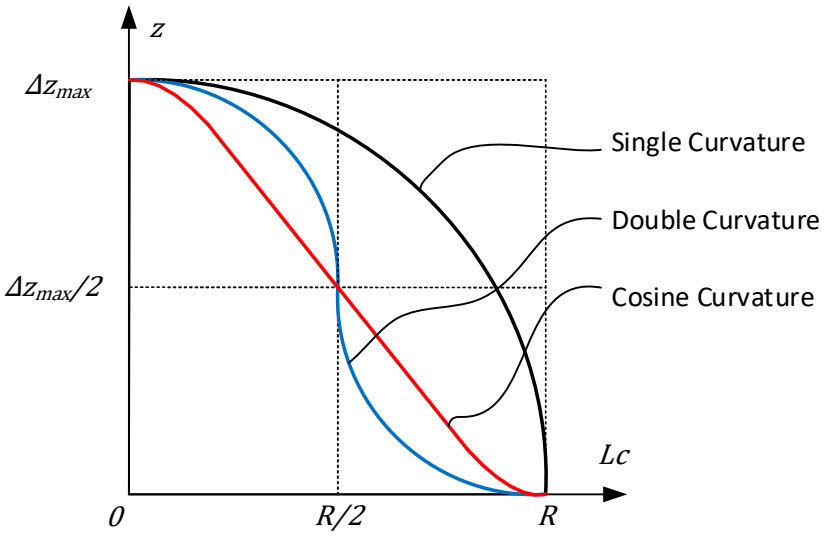

Figure 3.14 Shape profiles for $\Delta z_{max} = R$.

R indicates the radius of the obstacle in the horizontal plane. Δz_{max} is the maximum height of the obstacle at its peak point. Δz_{max} can be taken positive to form a bump or negative to form a cavity on the main ground surface. Profile given in Figure 3.14 is prepared for $\Delta z_{max} = R$ condition. For the generation of different size obstructions these profiles are $\Delta z_{max}/R$ times scaled in vertical direction.

In this definition, Lc is the closest distance to the centerline of the obstruction. Lc can be calculated from (x, y) location of a point as:

$$Lc = \begin{bmatrix} |Xs - x| & , \quad |Ys - y| \leq \dfrac{Ws}{2} \\ \sqrt{(Xs - x)^2 + \left(\dfrac{Ws}{2} - |Ys - y|\right)^2} & , \quad |Ys - y| > \dfrac{Ws}{2} \end{bmatrix} \tag{3.39}$$

Single curvature cross-section is designed to see the effects of an abrupt change in bed surface. Slope of the curve is zero at $Lc = 0$ and infinite at $Lc = R$. Height difference that is created by obstacle can be calculated as:

$$\Delta z = \frac{\Delta z_{max}}{R}\sqrt{R^2 - Lc^2} \quad , \qquad Lc \leq R \tag{3.40}$$

Double curvature cross-section is designed to see the effects of a smooth change in bed surface with infinite slope at $Lc = R/2$. Height difference that is created by obstacle can be calculated as:

$$\Delta z = \begin{bmatrix} \dfrac{\Delta z_{max}}{R}\left(\dfrac{R}{2} + \sqrt{(R/2)^2 - Lc^2}\right) & , \quad Lc \leq \dfrac{R}{2} \\ \dfrac{\Delta z_{max}}{R}\left(\dfrac{R}{2} - \sqrt{(R/2)^2 - (R - Lc)^2}\right), & \dfrac{R}{2} < Lc \leq R \end{bmatrix} \tag{3.41}$$

The cosine curve is designed to see the effects of the smooth change in bed surface. The maximum slope in the cosine curve is $\Delta z_{max}/R$. Height difference that is created by obstacle can be calculated as:

$$\Delta z = \frac{\Delta z_{max}}{2}\left(1 + \cos\left(\frac{Lc}{R}\pi\right)\right) \quad , \qquad Lc \leq R \tag{3.42}$$

The final shape of the ground can be calculated by adding the height difference from the shapes to the main ground level as:

$$z = z_{bed} + \Delta z \tag{3.43}$$

3.3.2 Test Runs for Flow over Simple Geometries

In order to compare the accuracy and stability of all solution schemes, a set of two-dimensional test cases are described with different geometric characteristics. Manning's formula is used in evaluation of friction slope and water surface slope is used in solutions. In solutions for Test Cases 1,2 and 3, Manning's roughness $n = 0.02\ (m^{-1/3}s)$, length of the domain is 500 m and the width of the domain is 250 m. Bed slope in x direction is $S_{0x} = 0.01$ and in y direction is $S_{0y} = 0.005$. Obstacles are located along x-axis $Xs = 375\ m$, and y-axis at the half-width of the domain and $Ws = 10\ m$ as centerline width of the obstacle. All solutions are obtained in steady uniform rainfall condition with rainfall intensity $I = 2.7x10^{-5} m/s = 97.2\ mm/hour$.

Solutions are obtained using different time steps and grid sizes and results are compared. Solutions are printed out as outflow hydrographs at the outlet to see the time-wise variations. Results are obtained with time step sizes that ensure the courant number limitation as Cr ≤ 0.2 since the upwind solver becomes unstable for Cr > 0.25.

3.3.2.1 Test Case-1: Tilted V-Catchment

In this test case, model does not contain any obstacle and known as Tilted V-Catchment. Three-dimensional shape of the ground geometry is shown in Figure 3.15.

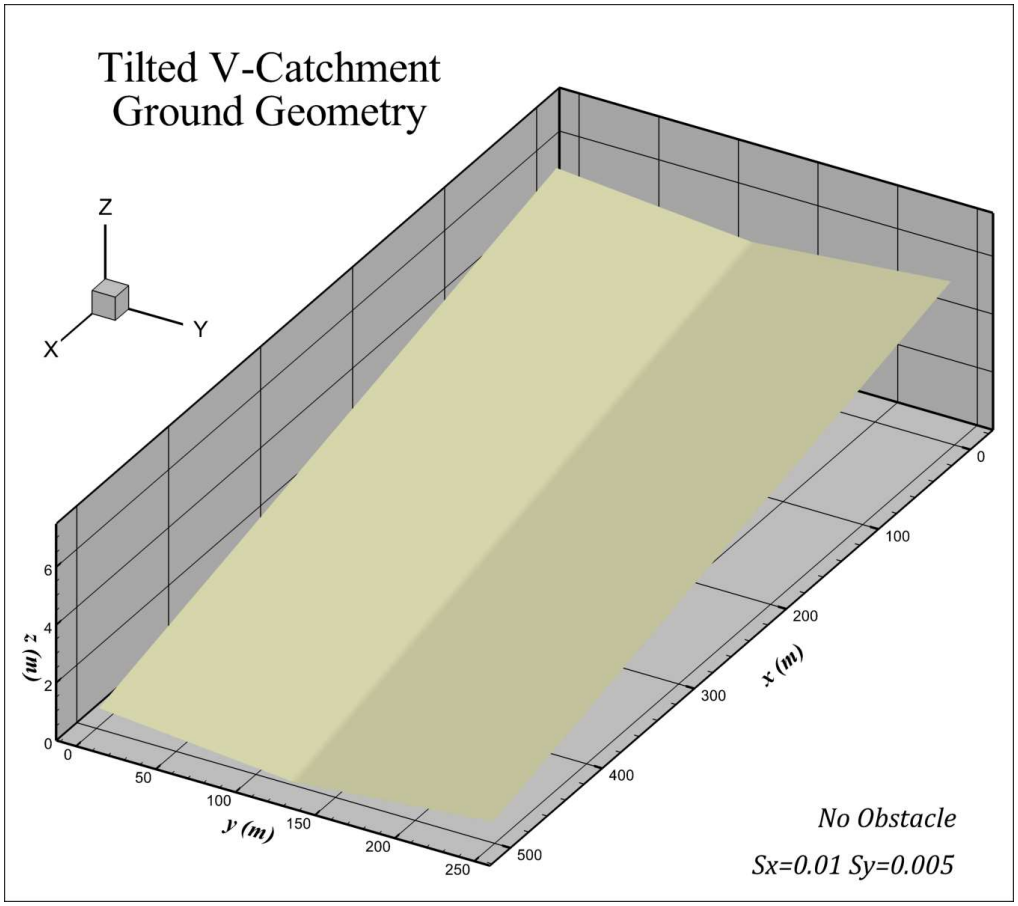

Figure 3.15 Test Case-1: 3D Ground geometry for tilted v-catchment model.

Time required for the steady-state in steady and uniform rainfall condition is considered to be 1000 seconds. After the steady-state condition, rainfall is stopped and numerical simulation is continued until $t = 2600\ s$ to see the decreasing water profile.

This case is solved with different solvers for different grid sizes to obtain the grid size requirements and behavior of solvers for different grid sizes.

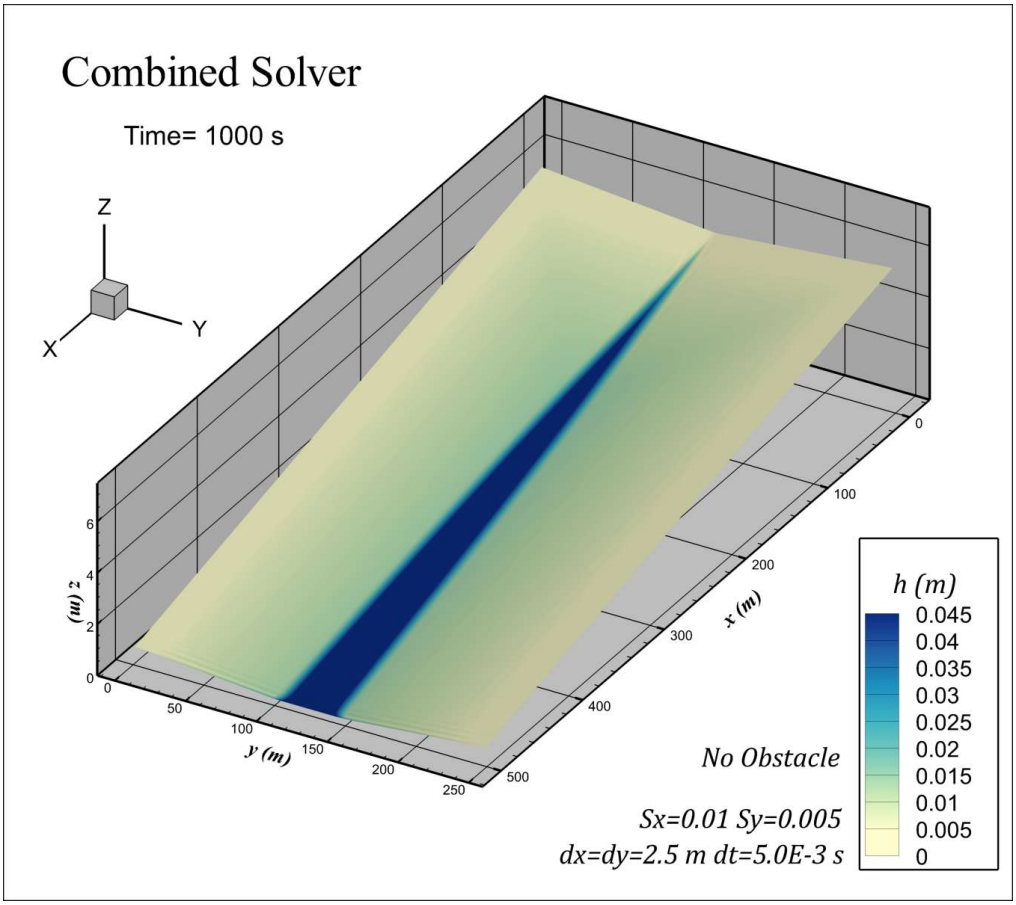

Figure 3.16 3D Water depth plot from combined solver for tilted v-catchment model at $t = 1000s$ (Test Case-1).

Combined solver solution for Test Case-1 is shown in Figure 3.16 and Figure 3.17. Water depth scale is given on the figures. Solutions at different time steps are shown in Figure 3.17.

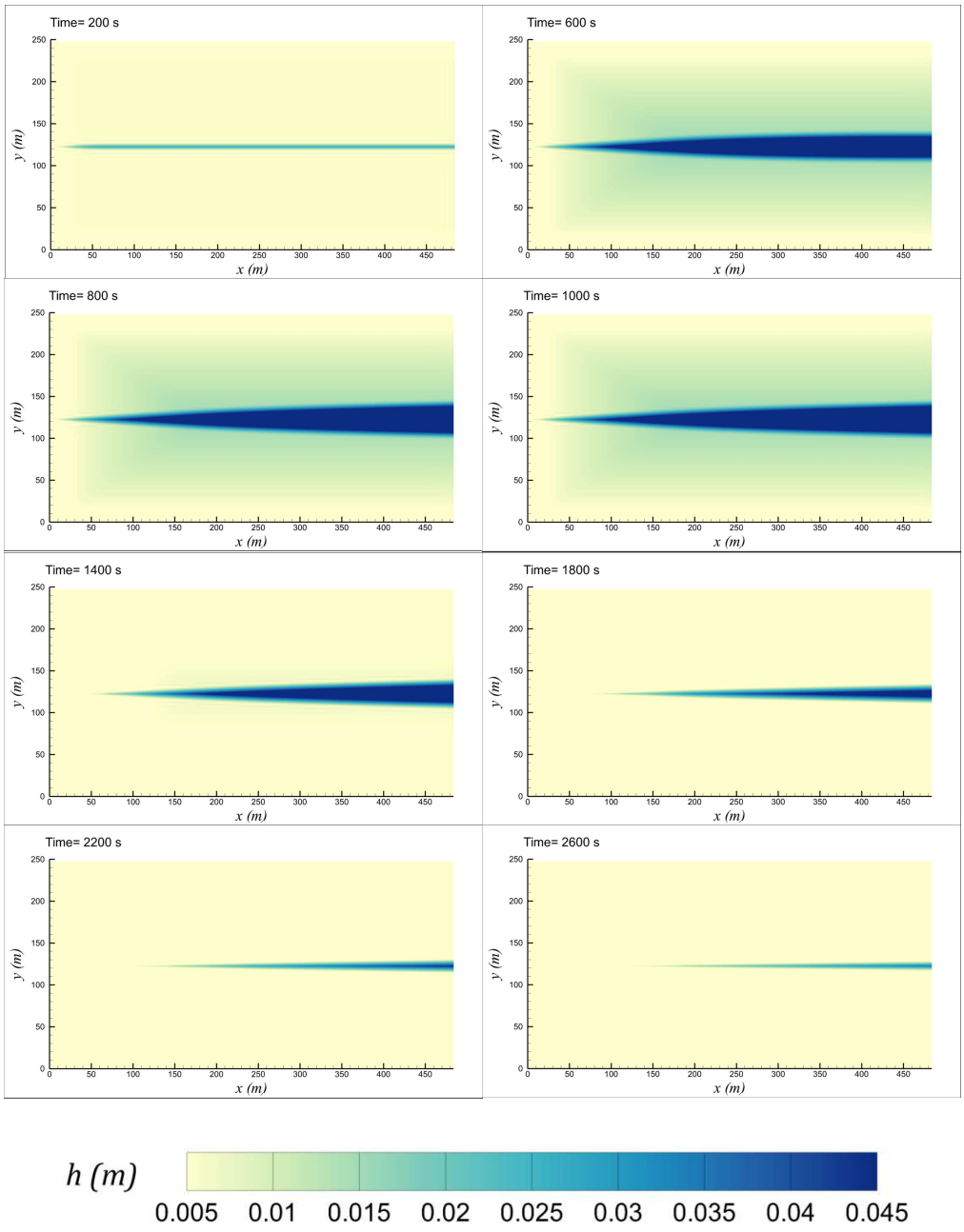

Figure 3.17 2D Water depth contour plot at different times for Test Case-1 from combined solver.

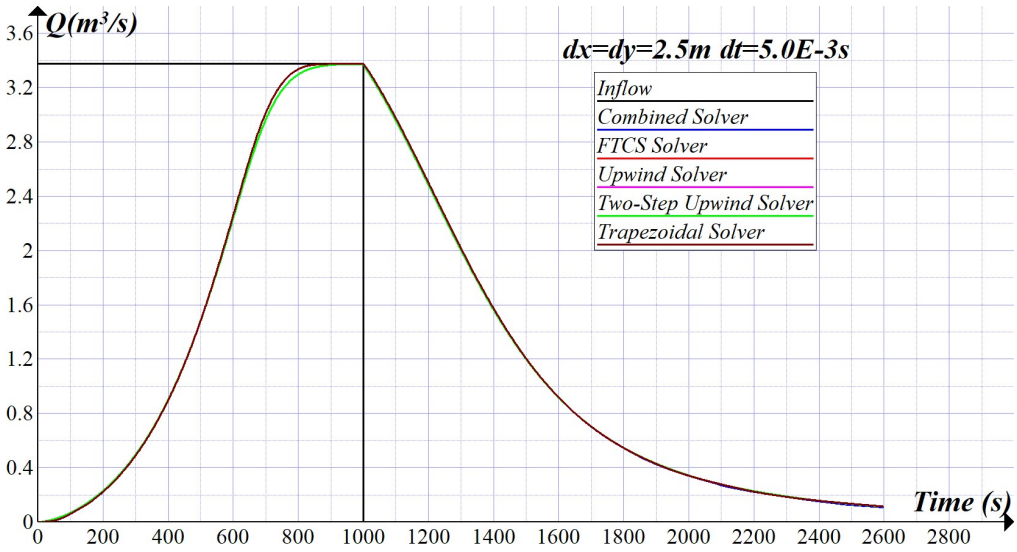

Figure 3.18 Outlet hydrograph for Test Case-1from different solvers.

Outflow hydrographs for Test Case-1 are printed out in Figure 3.18. Solutions from FTCS, combined and trapezoidal solvers just overlap, and two-step and single-step upwind solutions fit each other.

As can be seen in Figure 3.18, there are small differences between upwind and central space solutions in rising curve. As the mesh is refined upwind solution approaches to the central space solution which proves that the central space solution is more accurate.

To understand the behavior of solvers for solutions with coarser meshes outlet hydrographs from FTCS, upwind and combined solvers are shown out for different grid sizes in Figure 3.19, 3.27 and 3.28. It is observed that for solution over flat surfaces, the FTCS solver is more fragile when coarser mesh is used. Especially, in decreasing curve FTCS solution may lead to unrealistic outflow discharges.

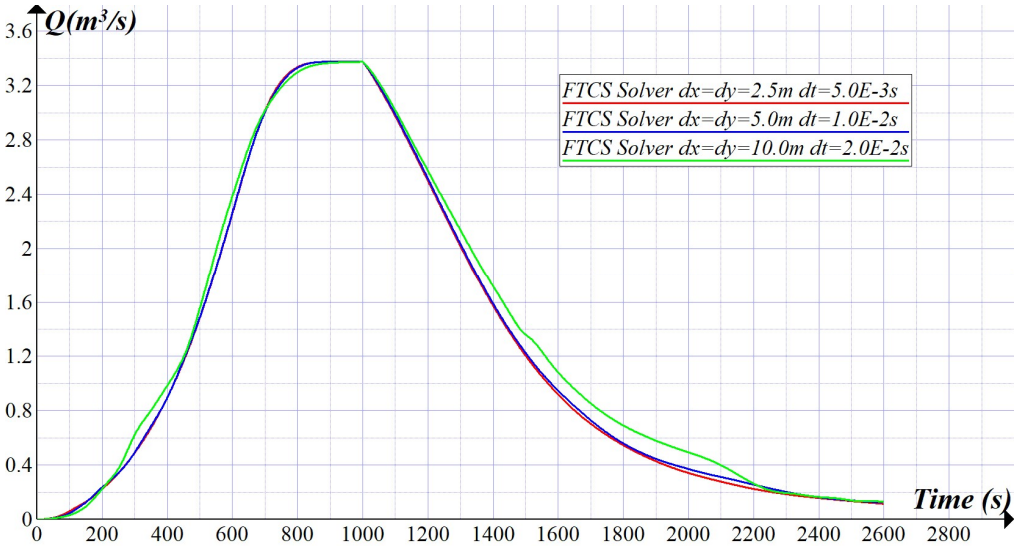

Figure 3.19 Outlet hydrograph obtained from FTCS solver for different grid sizes.

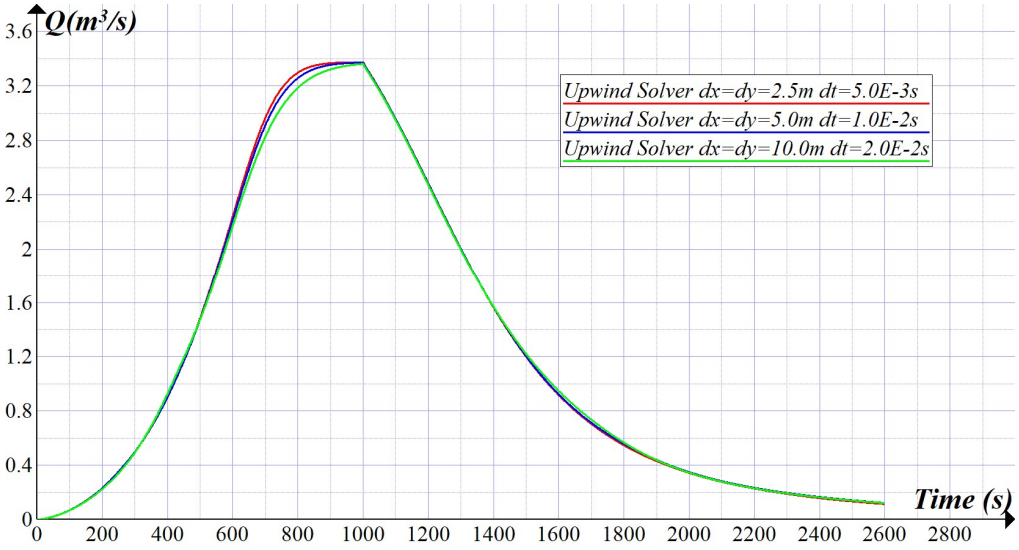

Figure 3.20 Outlet hydrograph obtained from upwind solver for different grid sizes.

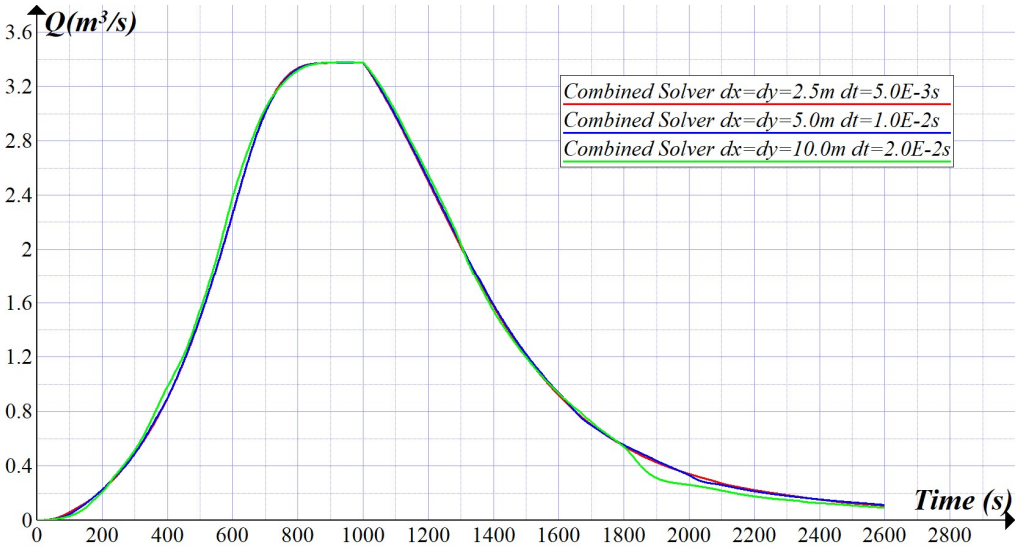

Figure 3.21 Outlet hydrograph obtained from combined solver for different grid sizes.

In Figure 3.22 coarser mesh solution for Test Case-1 from different solvers are compared with a finer solution. It is seen that in coarser solutions, the central space solution is more accurate in rising curve, upwind solution is more accurate in decreasing curve and combined solver is accurate in both conditions.

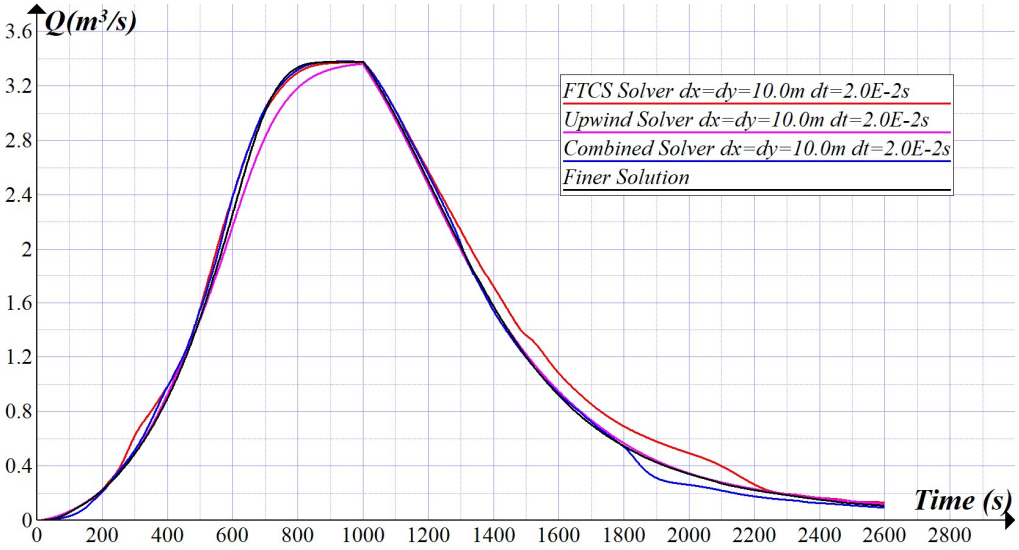

Figure 3.22 Comparison with finer mesh solution. Finer mesh solution obtained from the combined solver for $dx = dy = 2.5m$ and $dt = 5.0E - 3s$.

Cumulative inflow, cumulative outflow and water volume in the system at the end of solution from different solvers is given in Table 3.1 and Table 3.2.

Table 3.1 Cumulative inflow, cumulative outflow, and water volume in the system at $t = 2600s$ for finer solution ($dx = dy = 2.5m\ dt = 5.0E-3s$).

Solver	$\forall_{in}^{n}\ (m^3)$	$\forall_{out}^{n}\ (m^3)$	$\forall_{sys}^{n}\ (m^3)$	$100 * \frac{\forall_{out}^{n} + \forall_{sys}^{n}}{\forall_{in}^{n}}$
FTCS	3375.016	3273.269	101.747	100
Upwind	3375.016	3258.844	116.172	100
Combined	3375.016	3270.345	104.672	100
Two-Step Upwind	3375.016	3258.843	116.174	100
Trapezoidal	3375.016	3273.267	101.749	100

Table 3.2 Cumulative inflow, cumulative outflow, and water volume in the system at $t = 2600s$ for coarser solution ($dx = dy = 10m\ dt = 2.0E-2s$).

Solver	$\forall_{in}^{n}\ (m^3)$	$\forall_{out}^{n}\ (m^3)$	$\forall_{sys}^{n}\ (m^3)$	$100 * \frac{\forall_{out}^{n} + \forall_{sys}^{n}}{\forall_{in}^{n}}$
FTCS	3375.016	3455.619	-80.549	100
Upwind	3375.016	3232.623	142.446	100
Combined	3375.016	3266.670	108.399	100
Two-Step Upwind	3375.016	3232.617	142.452	100
Trapezoidal	3375.016	3455.578	-80.510	100

As it is understood from Cumulative inflow, cumulative outflow and water volume in the system at the end of solution from different solvers is given in Table 3.1 and Table 3.2.

Table 3.1 and Table 3.2, coarser solution from FTCS solver leads negative volumes. The non-physical results from FTCS solution at decreasing curves in outlet hydrographs are seems to be due to negative water depth calculations of that method.

3.3.2.2 Test Case-2: Tilted V-Catchment with a Bump

In this test case, the model contains a bump at $Ls = 375\ m$. Radius of the bump is 60 m and has double curvature profile. Three-dimensional shape of the ground geometry for Test Case-2 is shown in Figure 3.23.

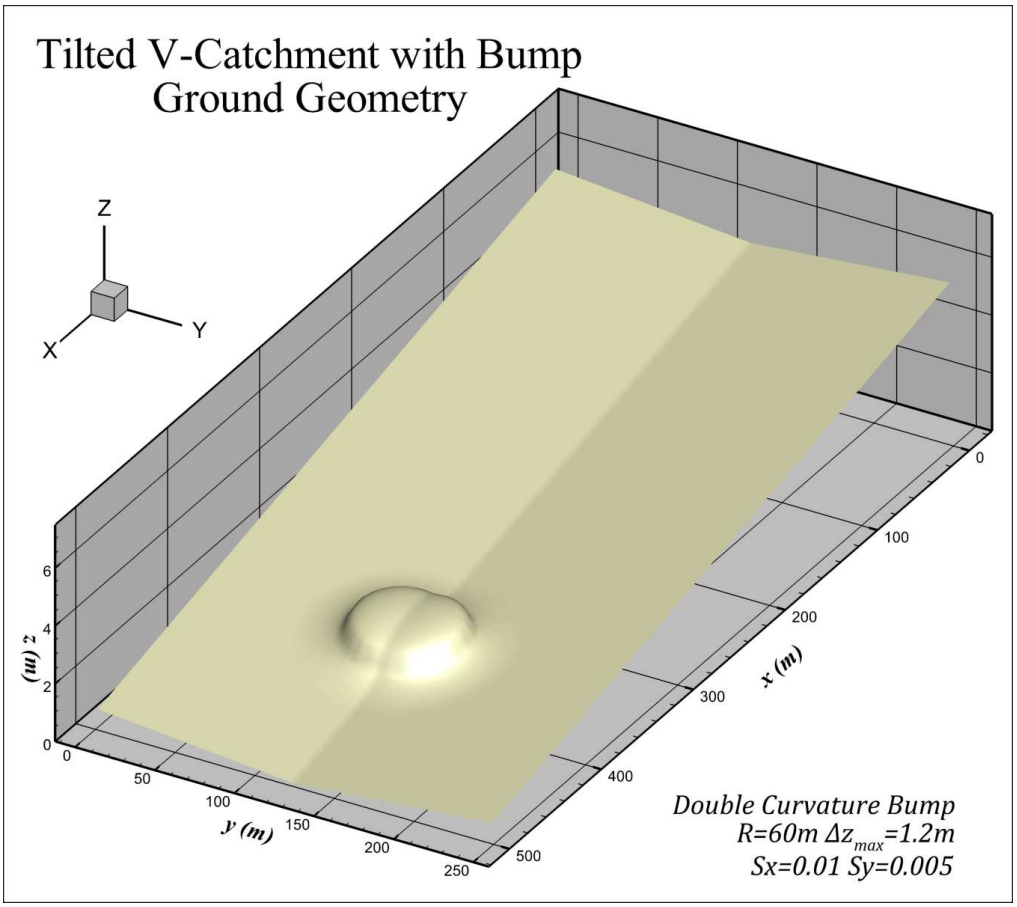

Figure 3.23 3D Ground geometry for Test Case-2

Time required for the steady-state in steady and uniform rainfall condition is considered to be 1200 seconds. After the steady-state condition, rainfall is stopped and simulation is continued until $t = 3600\ s$ to see the decreasing water profile.

This case has been solved with different solvers for different time step sizes to obtain the effects of the time step size and behavior of solvers for different time-step sizes.

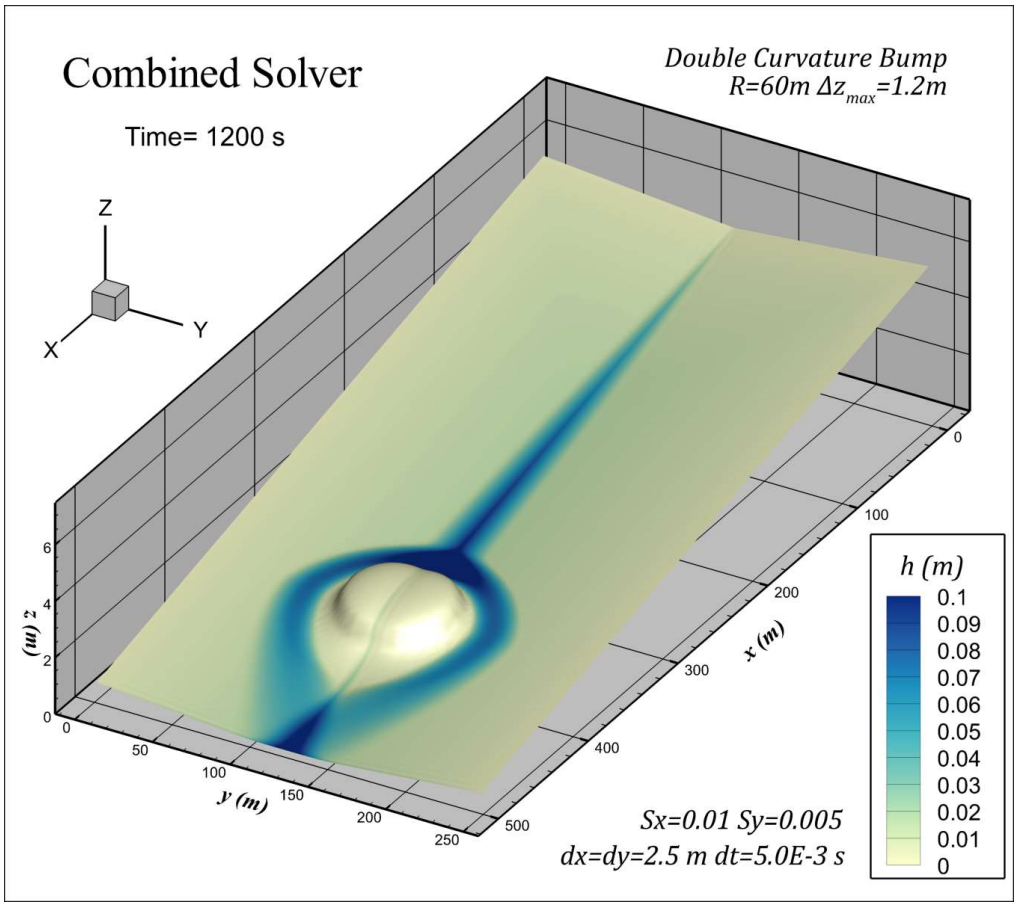

Figure 3.24 3D Water depth plot from combined solver for Test Case-2 at $t = 1200\ s$.

In Figure 3.24 and Figure 3.25, combined solver solution for Test Case 2 is shown. Water depths are scaled by color density and legend is given on the bottom of the figures. Solution at different time steps are shown in Figure 3.25.

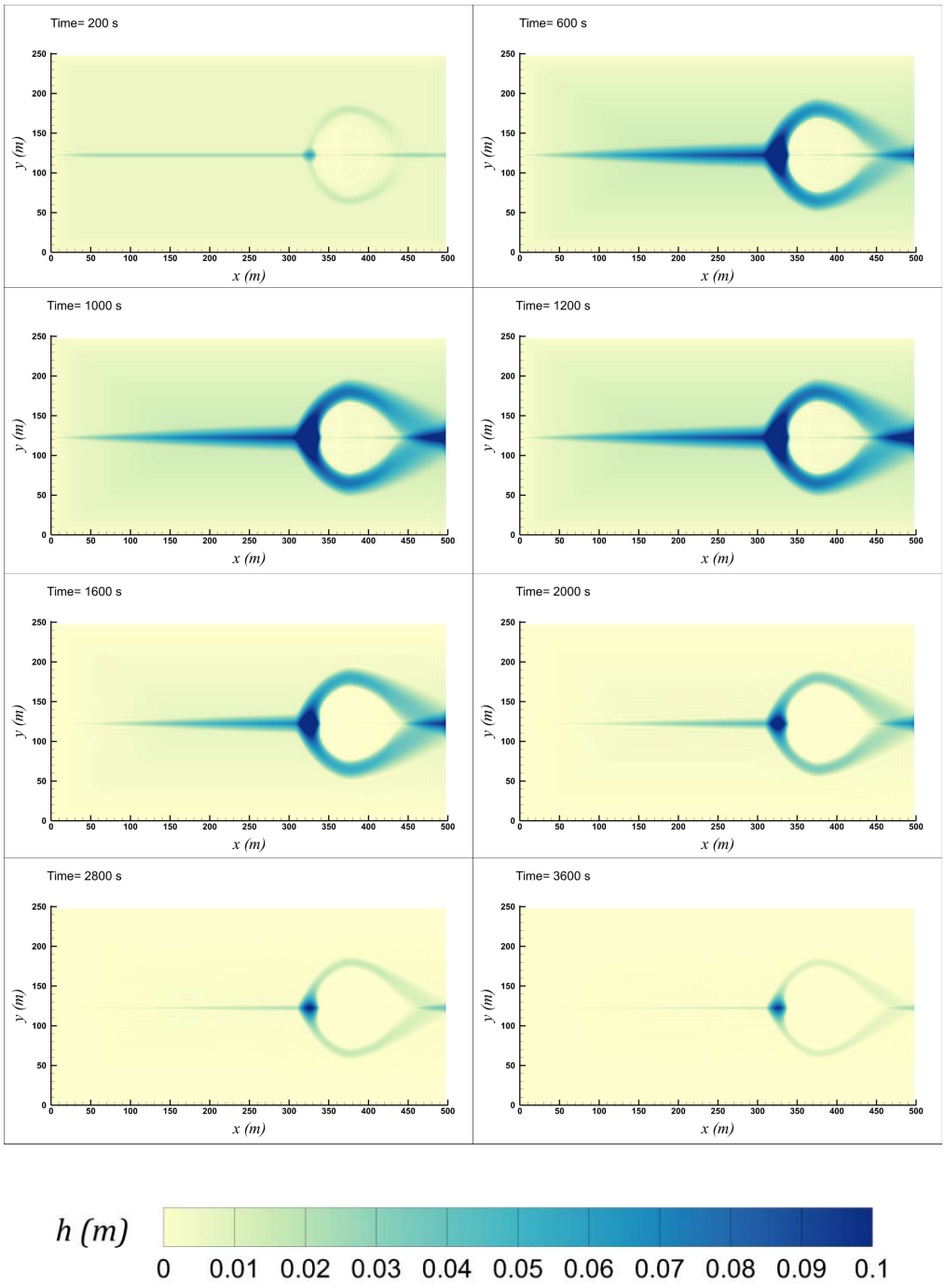

Figure 3.25 2D Water depth contour plot at different times for Test Case-2 from combined solver.

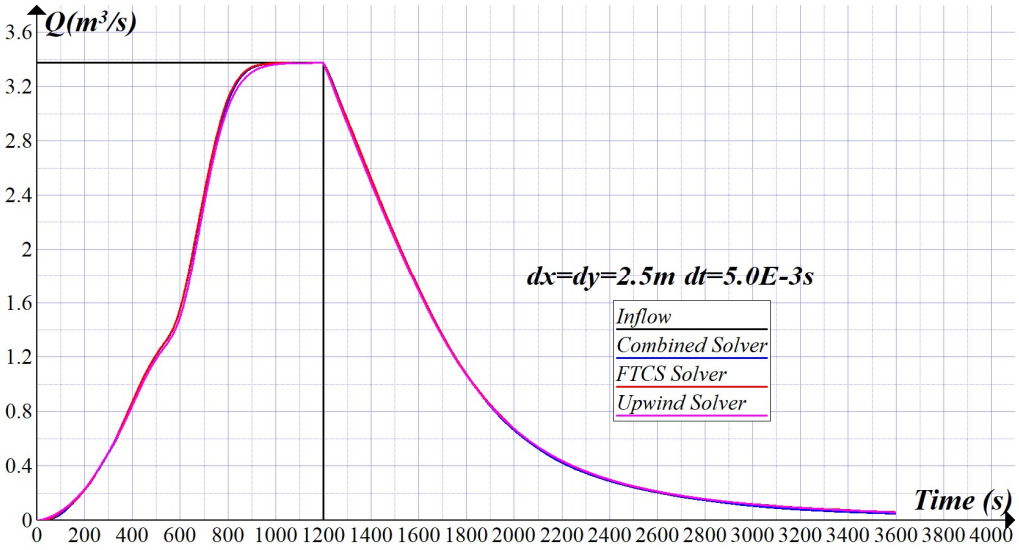

Figure 3.26 Outlet hydrograph for fine mesh solution of Test Case-2 from FTCS, upwind and combined solvers.

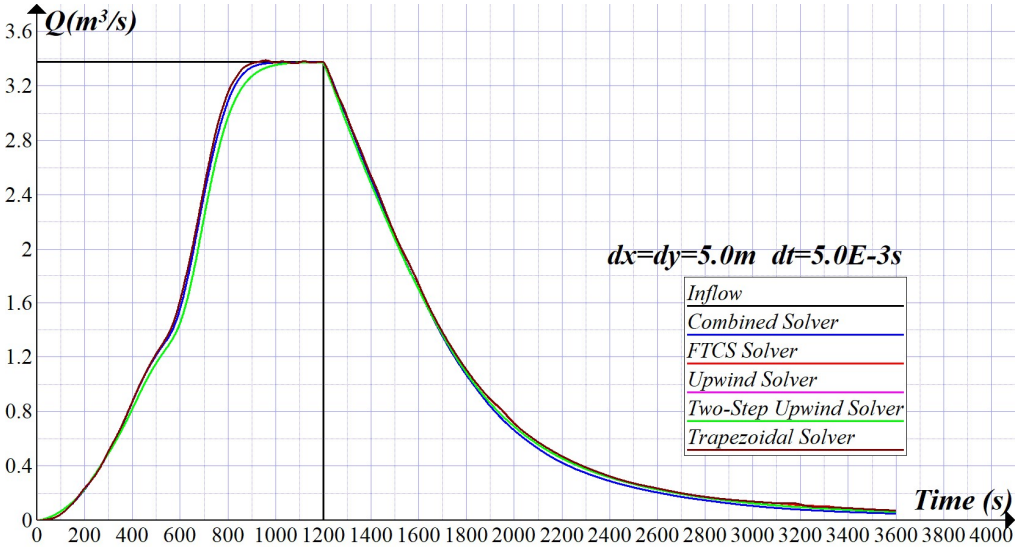

Figure 3.27 Outlet hydrograph for coarser mesh solution of Test Case-2 from all solvers.

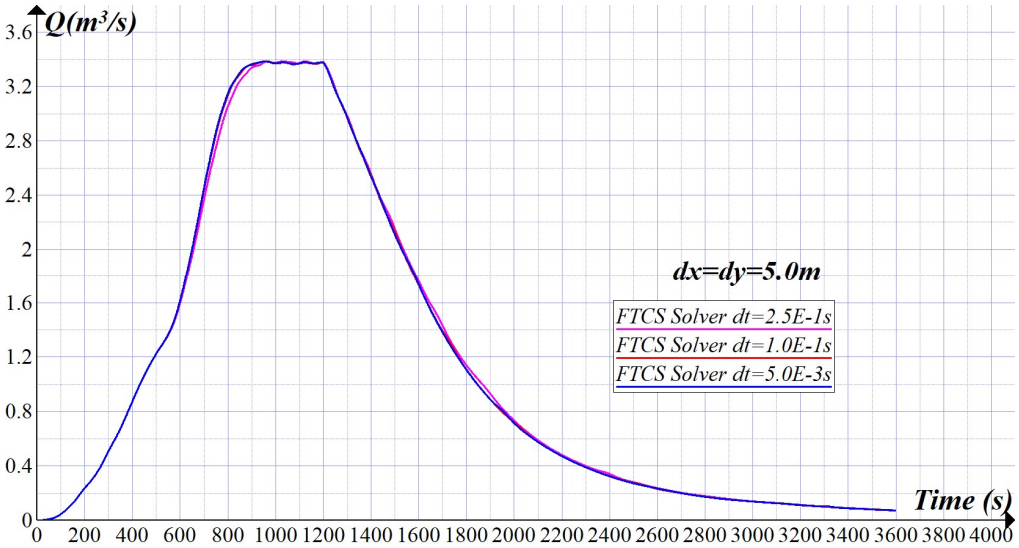

Figure 3.28 Outlet hydrograph for Test Case-2 obtained from FTCS solver for different time-step sizes.

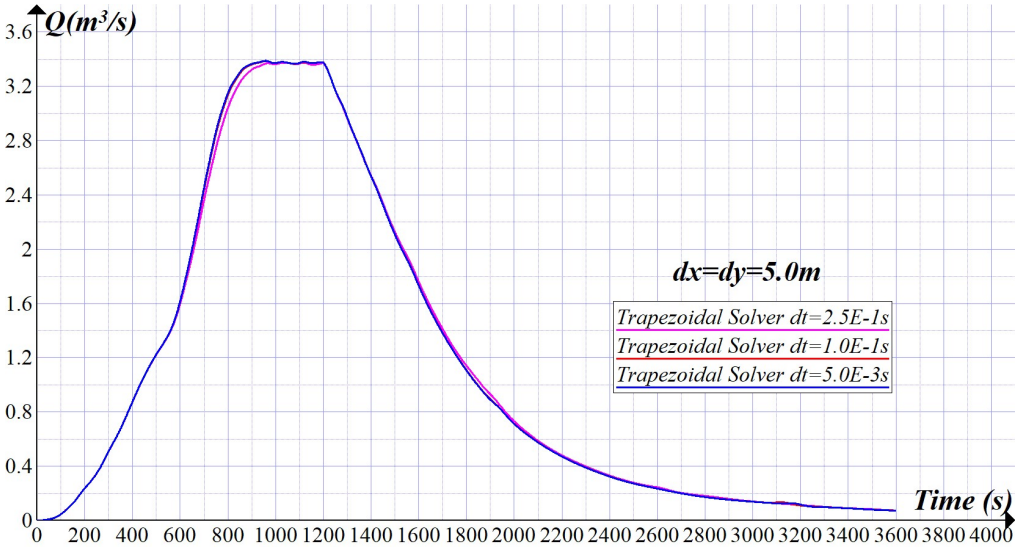

Figure 3.29 Outlet hydrograph for Test Case-2 obtained from trapezoidal central space solver for different time-step sizes.

As can be seen in Figure 3.28 and Figure 3.29, central space solution leads to fluctuations in outlet hydrograph colose to steady-state condition and there is no difference between forward time and trapezoidal solution.

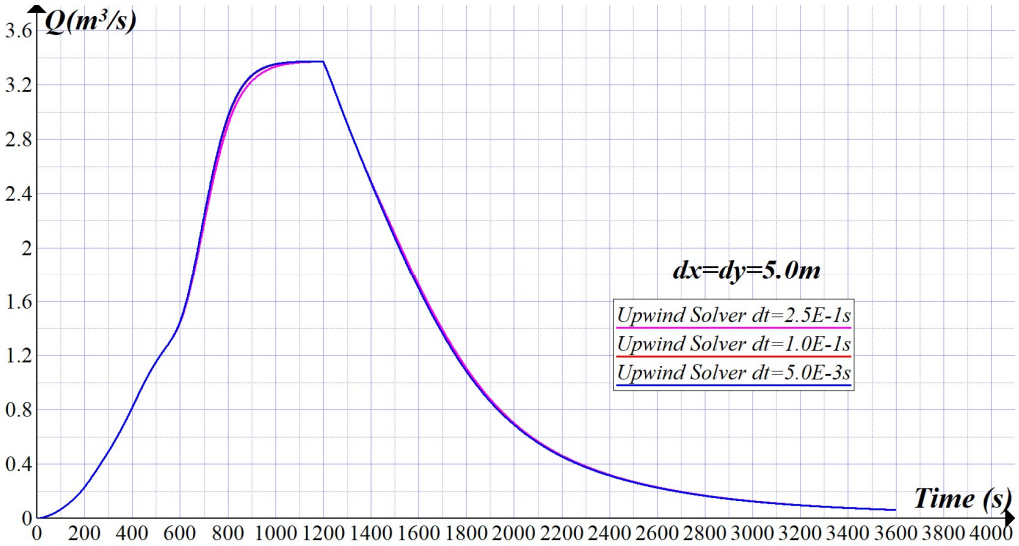

Figure 3.30 Outlet hydrograph for Test Case-2 obtained from upwind solver for different time step sizes.

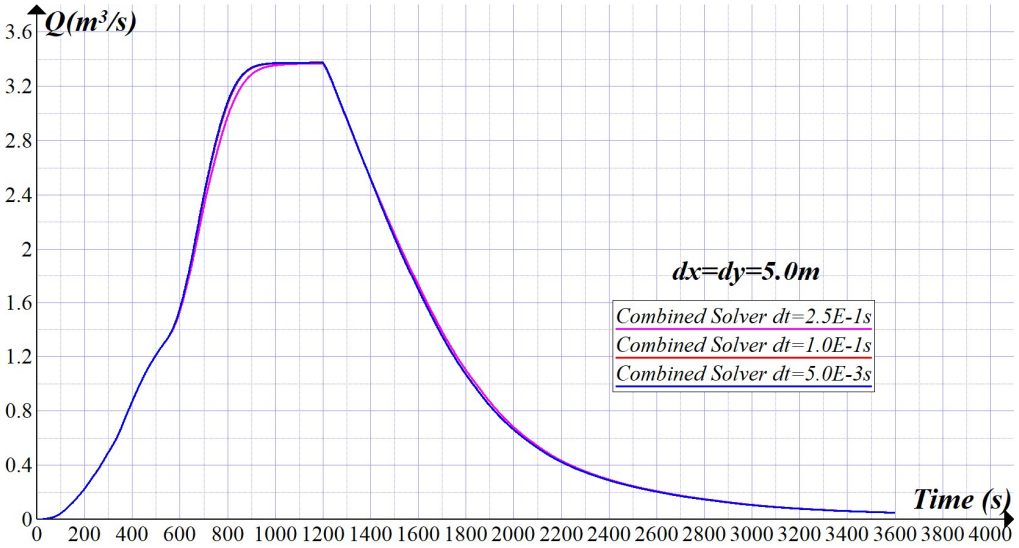

Figure 3.31 Outlet hydrograph for Test Case-2 obtained from combined solver for different time step sizes.

As can be seen in Figure 3.30 and Figure 3.31, combined solver solution leads more reasonable results in rising hydrograph and filters the fluctuations in central space solution. Outlet hydrograph obtained by combined solver has advantage of using both upwind and the central space solutions in appropriate regions.

From outlet discharge plots it can be observed that the trapezoidal or two-step solution has no advantage on forward time solution. As the model in this test case is relatively large and water levels are changing slowly, there is no need to use higher-order accurate method for the solution of the continuity equation. As long as stability condition is satisfied all the solvers generate meaningful results.

3.3.2.3 Test Case-3: Tilted V-Catchment with Cavity

In this case, the model contains a double curvature cavity. Three-dimensional ground geometry for V-Catchment with a cavity is shown in Figure 3.32.

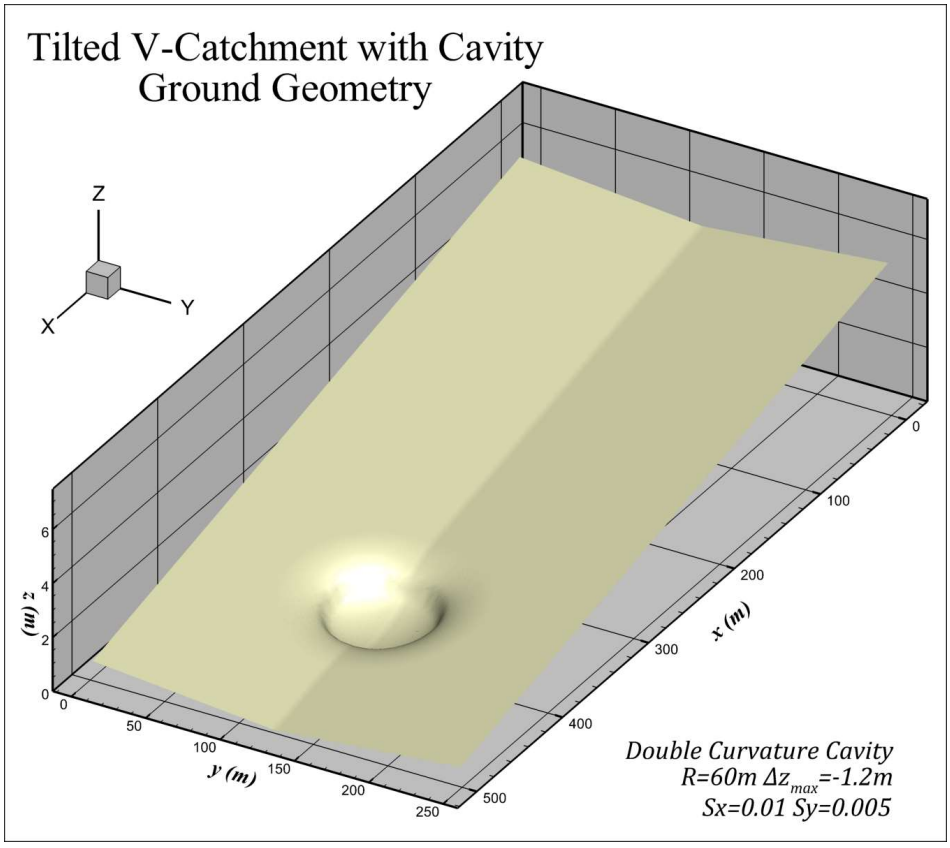

Figure 3.32 3D Ground geometry for Test Case-3.

Time required for the steady-state condition is found to be 2200 seconds. After the steady-state condition at $t = 2200\ s$, rainfall is stopped. The simulation is continued until $t = 4400\ s$ to see the decreasing water depth profile.

Test Case-3 is solved with different solvers for different grid sizes to obtain the effects of the grid sizes and behavior of solvers for different grid sizes.

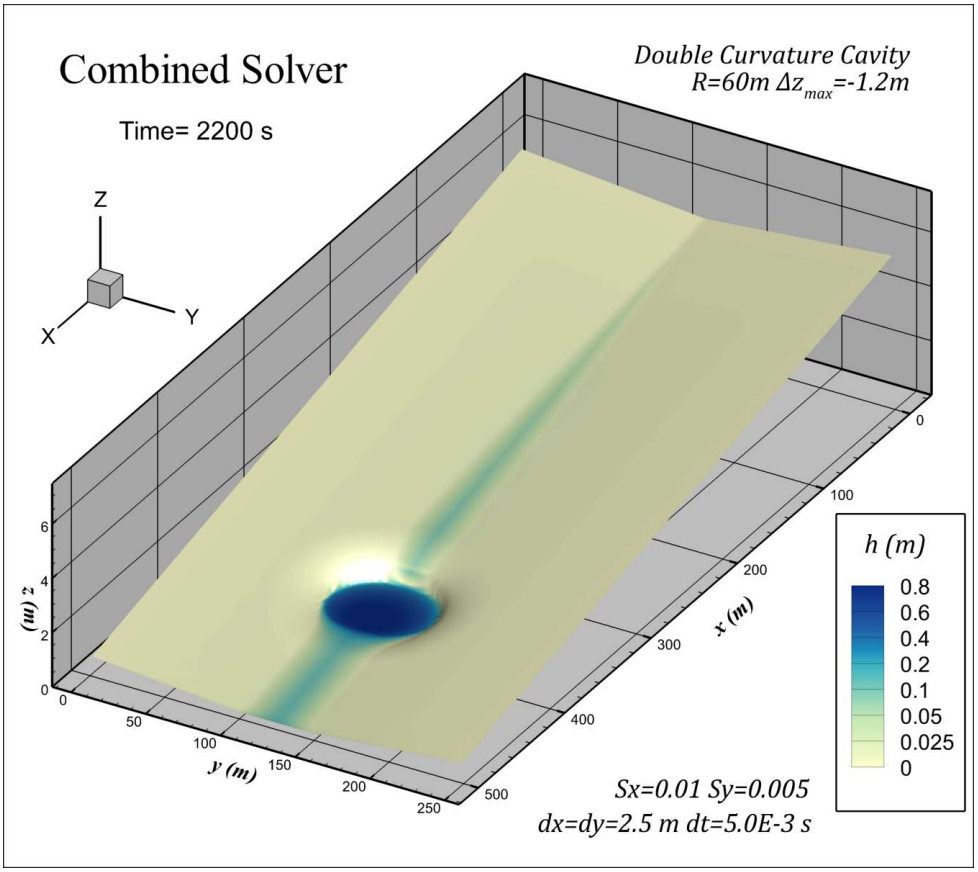

Figure 3.33 Water surface profile for Test Case-3 from combined solver at $t = 2200\ s$.

In Figure 3.33 and Figure 3.34, combined solver solution for Test Case-3 is shown. Solutions at different time steps are also show in Figure 3.34.

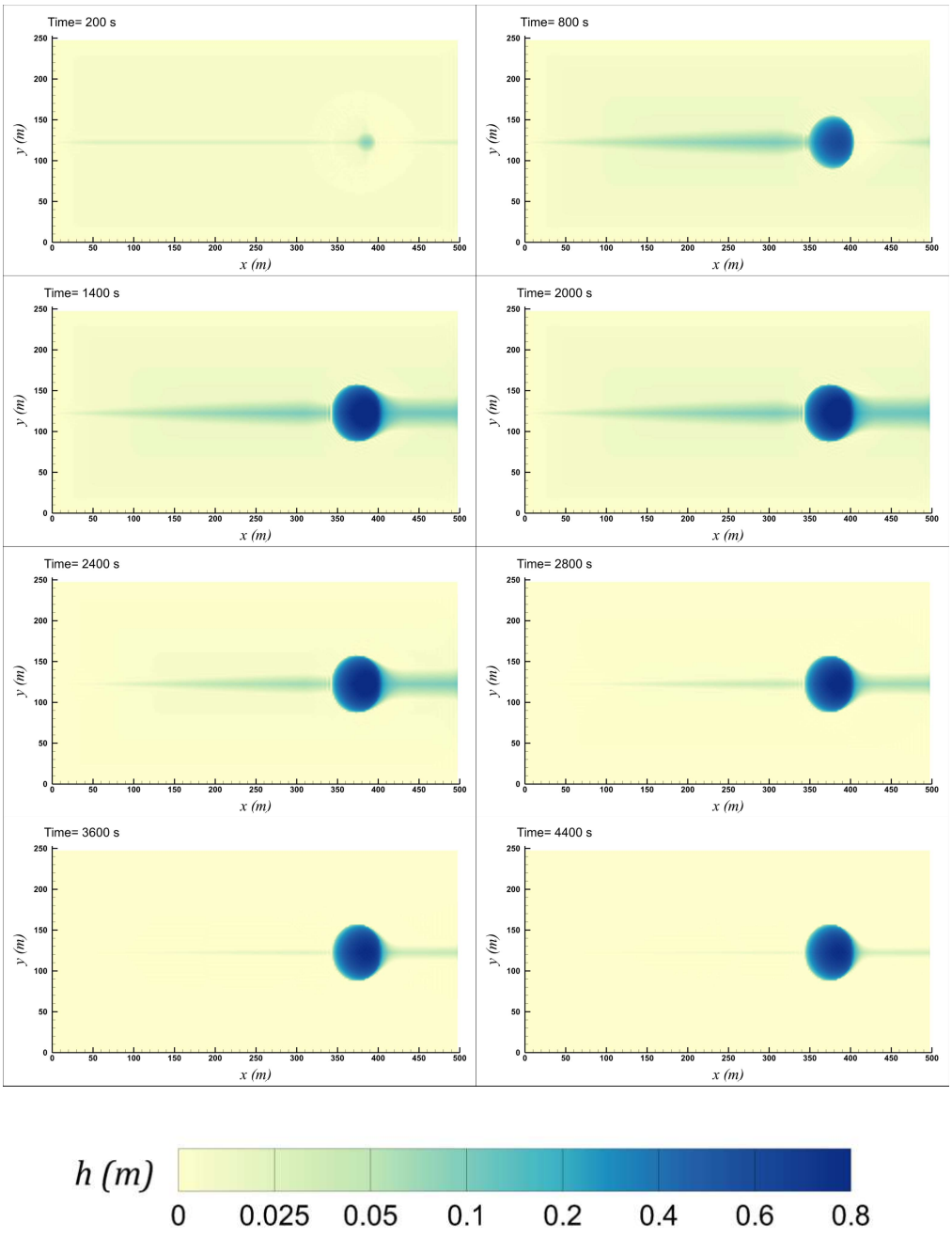

Figure 3.34 2D Water depth contour plots at different times for Test Case-3 from combined solver.

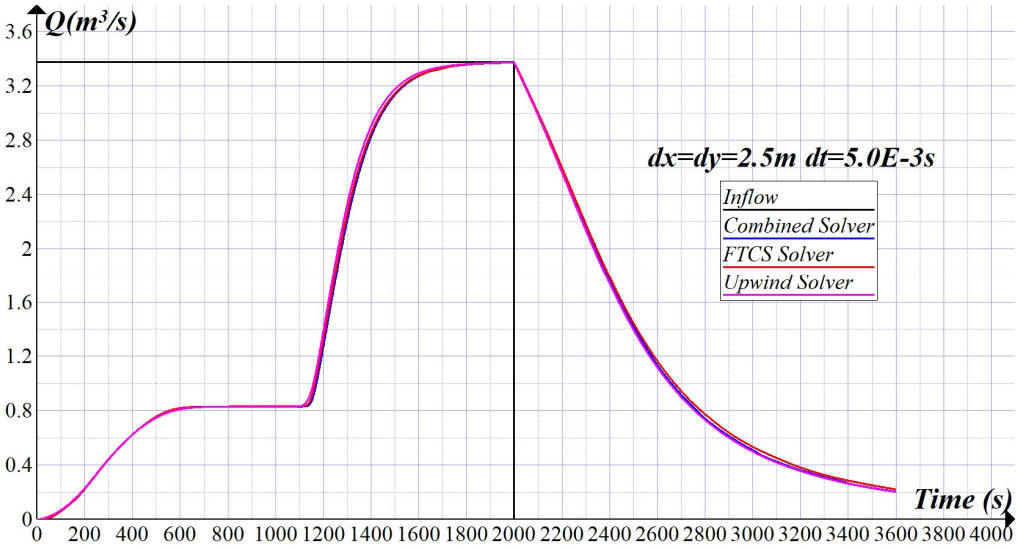

Figure 3.35 Outlet hydrograph for fine mesh solution of Test Case-3 from FTCS, upwind and combined solvers.

As seen in Figure 3.35, outlet hydrograph shows a plato between 600s and 1100s. This plato section shows the time required for filling the cavity.

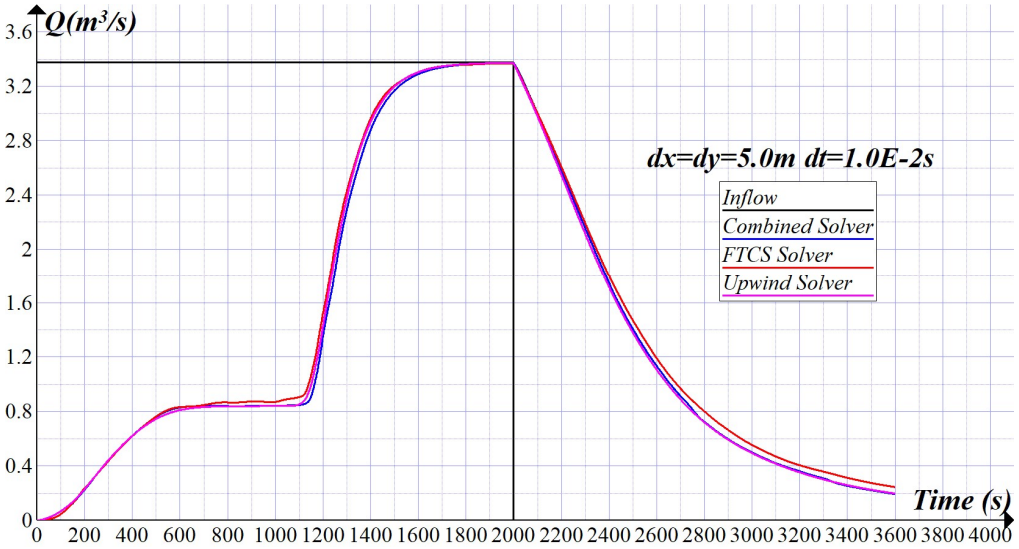

Figure 3.36 Outlet hydrograph for coarser mesh solution of Test Case-3 from FTCS, upwind and combined solvers.

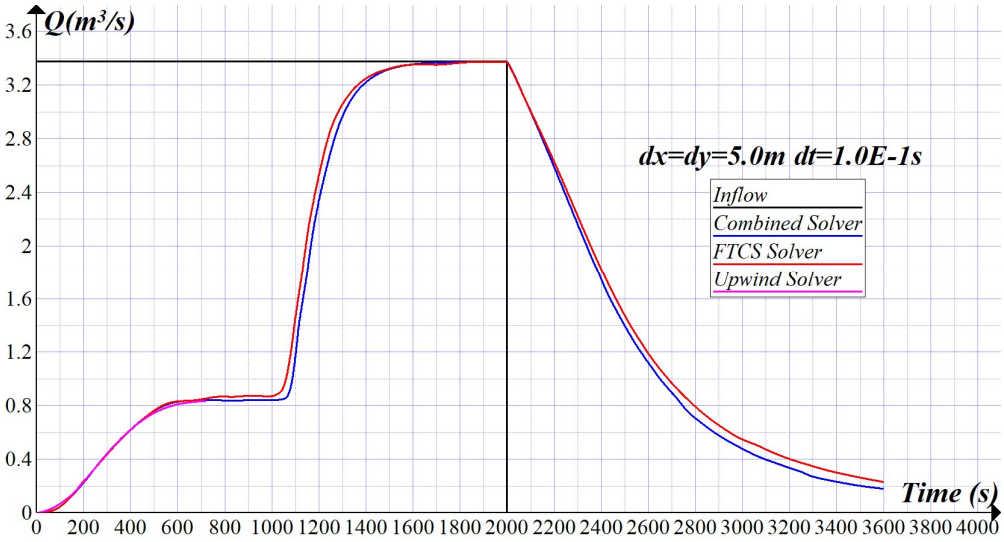

Figure 3.37 Outlet hydrograph for coarser mesh solution of Test Case-3 from FTCS, upwind and combined solvers.

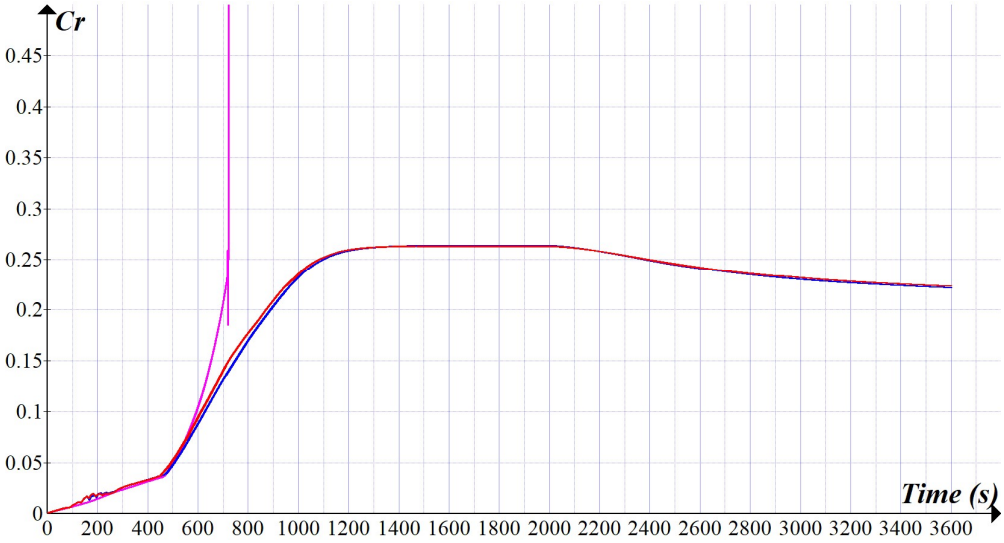

Figure 3.38 Courant number plot for the solution given in Figure 3.37.

In solution given in Figure 3.37, upwin solver fall at t=713s because of dynamic instability and it can be seen in courant number plot shown in Figure 3.38. Combined and FTCS solvers are stable.

3.4 Test Runs for Flow over Combined Bump-Cavity Geometries

More complex ground geometry is generated by superposition of bump and cavity using the previous definitions. In contrary to previous cases, there are multiple obstructions in the domain. In solutions for Test Cases 4 and 5, Manning's roughness $n = 0.02\ (m^{-1/3}s)$, length of the domain is 500 m and width of the domain is 300 m, bed slope in x direction is $S_{0x} = 0.01$ and in y direction is $S_{0y} = 0.005$. Locations and sizes of the obstructions are given in Table 3.3.

Table 3.3 Locations and sizes of obstructions in Test Case-4 and Test Case-5

Curvature	*Xs(m)*	*Ys(m)*	*Ws(m)*	R(m)	Δz_{max}*(m)*
Double Curvature	375	150	10	75	-0.8
Single Curvature	325	85	10	30	1.2
Double Curvature	340	235	0	50	1.2
Cosine Curvature	290	170	10	60	1.6
Cosine Curvature	260	100	10	25	-0.9

The combined solver only will be used for the numerical solutions since the combined solver generated better results in the previous cases.

Solutions are obtained using constant grid size $dx = dy = 2.5m$ for all solutions and time step size is increased with rainfall intensity to keep the courant number same for different solutions and ensured that the courant number limitations defined in previous solutions are exceeded.

Solutions are printed out as outflow hydrographs at the outlet to see the time wise variations.

3.4.1.1 Test Case-4: Tilted V-Catchment with Multiple Bumps and Cavities

Three-dimensional shape of the ground geometry is shown in Figure 3.39.

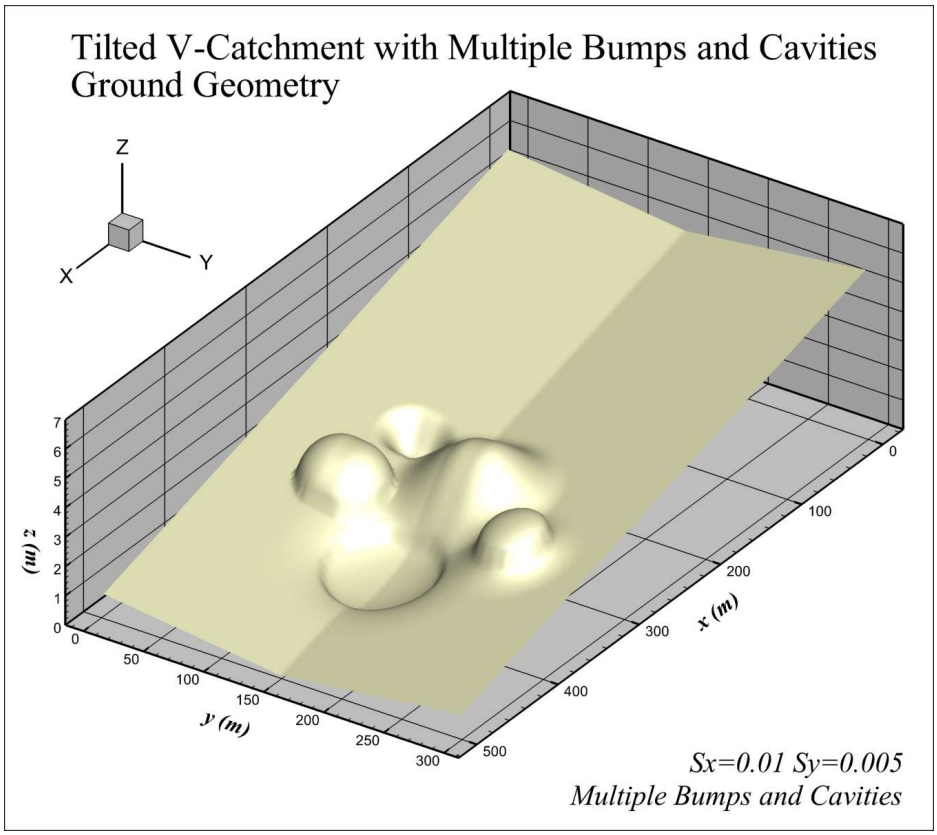

Figure 3.39 3D Ground geometry for Test Case-4.

In order to see the effects of the rainfall intensity and to check the stability and behavior of the solver over complex geometries numerical solution is obtained for different rainfall intensities.

- Violent Rain $I = 8.1x10^{-5} m/s = 291.6\ mm/hour$
- Heavy Rain $I = 2.7x10^{-5} m/s = 97.2\ mm/hour$
- Moderate Rain $I = 9.0x10^{-6} m/s = 32.4\ mm/hour$
- Low Rain $I = 3.0x10^{-6} m/s = 10.8\ mm/hour$

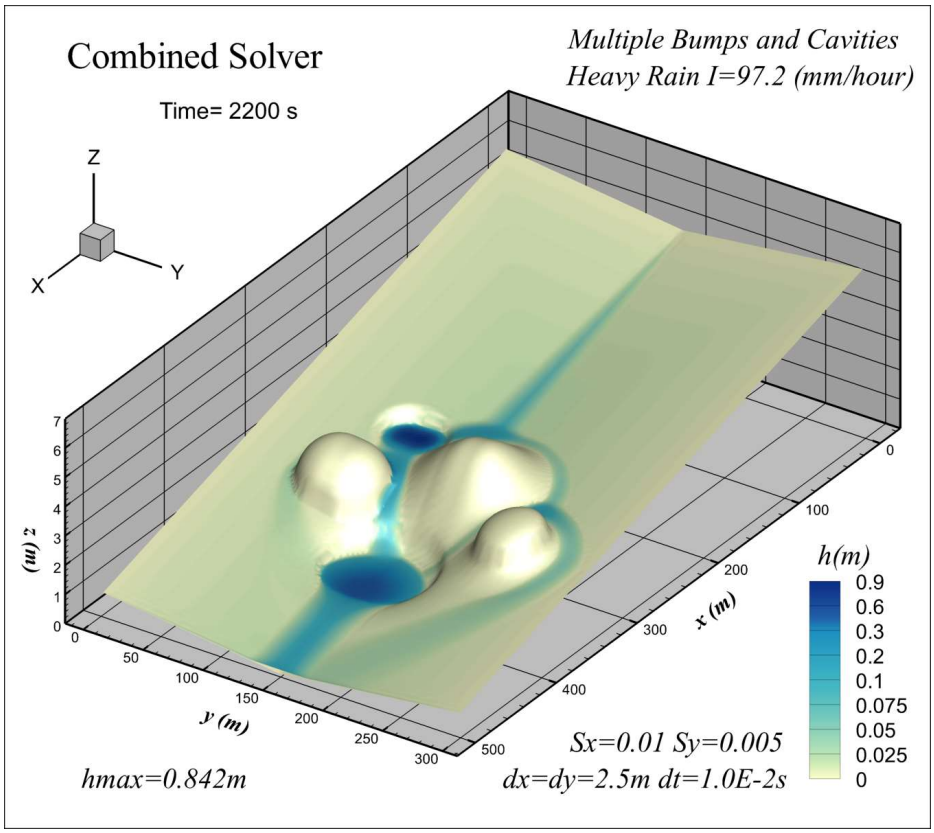

Figure 3.40 Water surface profile from combined solver for Test Case-4 at $t = 2200s$

Time required for the steady-state in steady and uniform rainfall condition is considered to be 2200 seconds. At $t = 2200\ s$ rainfall is stopped and numerical simulation is continued until $t = 4400\ s$ to see the decreasing water profile.

Combined solver solution for Test Case-4 in heavy rain condition is shown in Figure 3.40 and solution at different time steps are shown in Figure 3.43.

Solution for different rainfall conditions is shown in Figure 3.41 and outlet hydrograph is given in Figure 3.42. It is seen that the solver is stable in all rainfall conditions. In low rain and moderate rain conditions time of rain was not enough for system to reach the steady state.

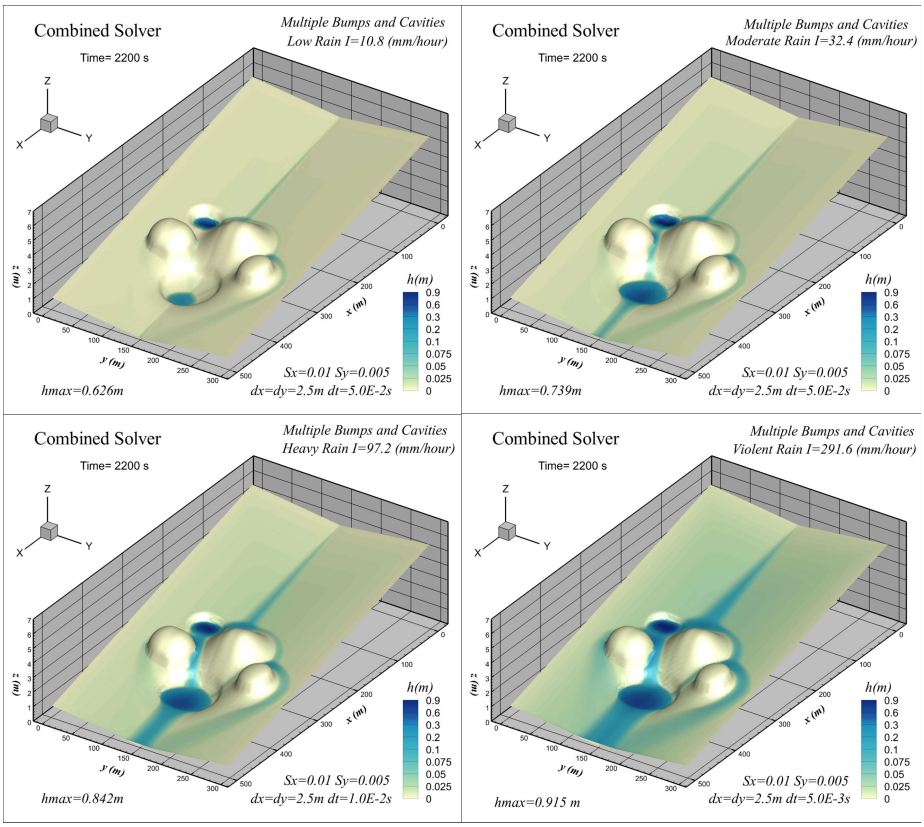

Figure 3.41 3D water depth plots from combined solver for Test Case-4 for different rain intensities at $t = 2200s$.

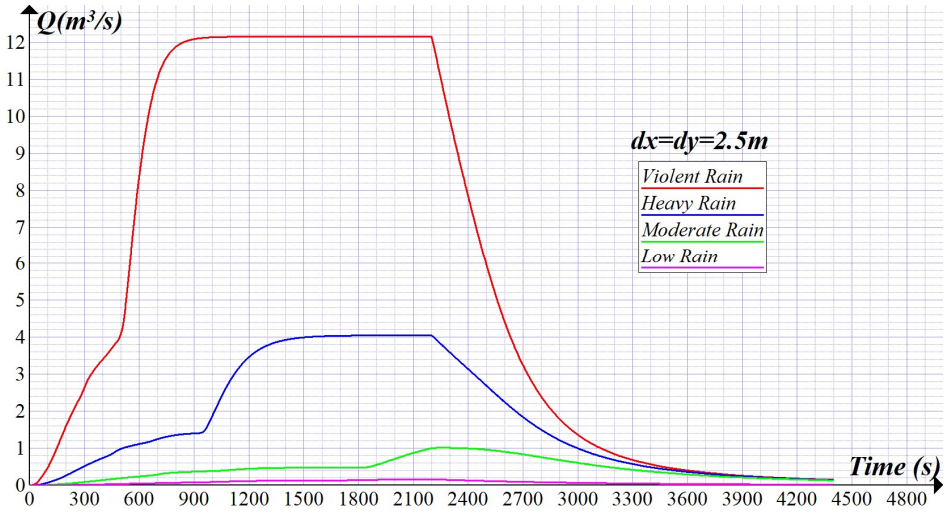

Figure 3.42 Outlet hydrograph for Test Case-4.

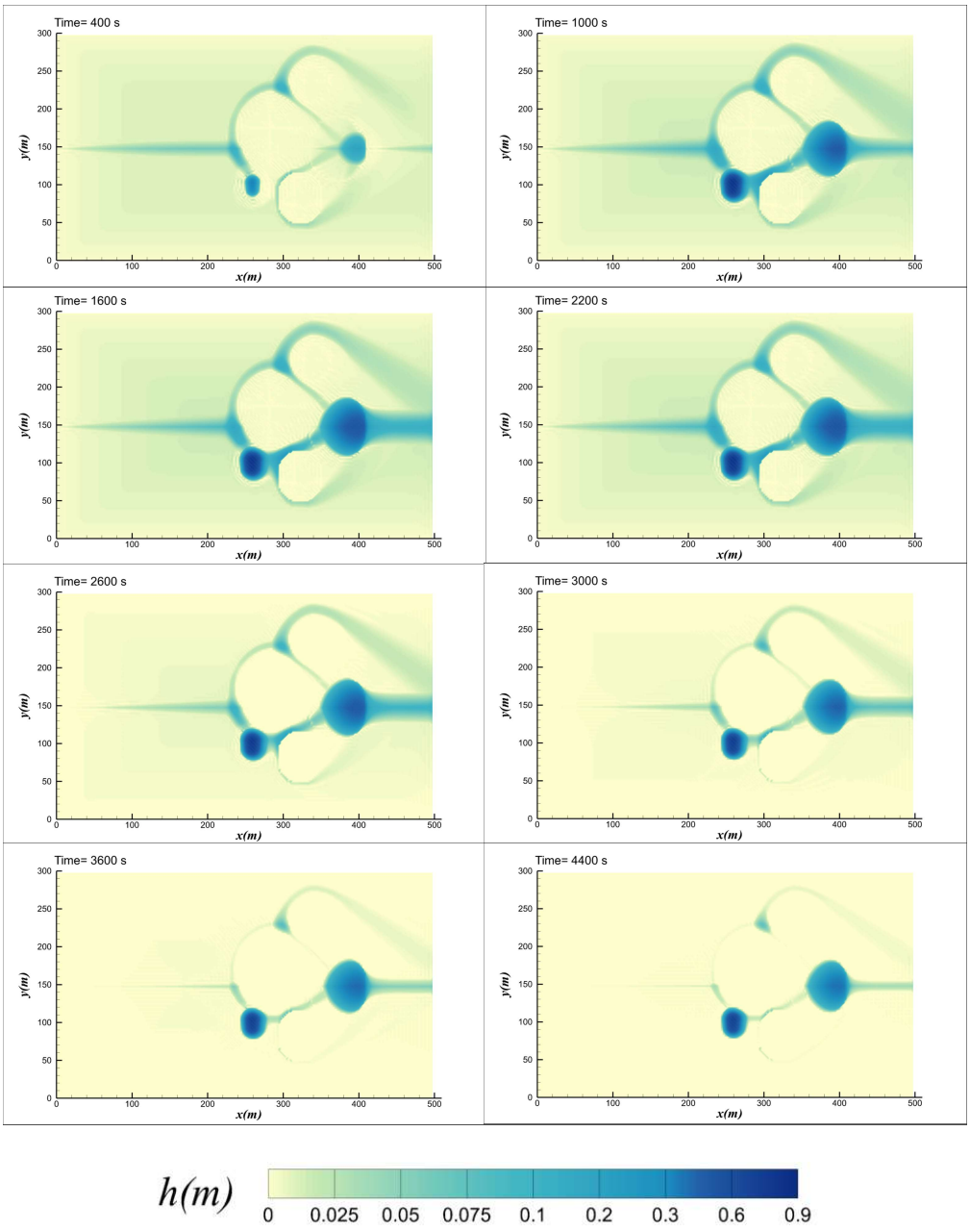

Figure 3.43 2D Water depth contour plots at different times for Test Case-4 from combined solver.

3.4.1.2 Test Case-5: Tilted V-Catchment with Multiple Bumps, Cavities and a Wall

In different from the previous case, a vertical wall is placed in the middle of the solution domain. The location of the wall is defined as wall cells at 85th node in x-direction and between 45th and 75th nodes in y-direction. Three-dimensional shape of the ground geometry is shown in Figure 3.44.

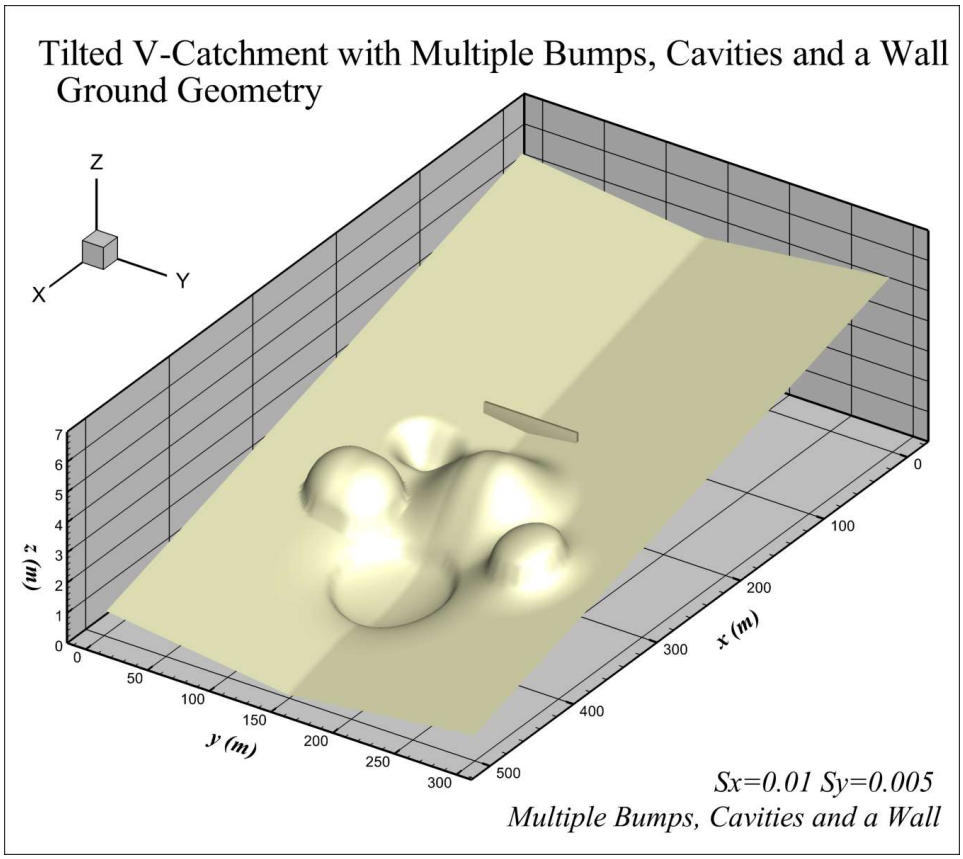

Figure 3.44 3D Ground geometry for Test Case-5.

Solution for this case is obtained only using combined solver for heavy rain condition. Three dimensional water depth plot from downstream and upstream locations is given in Figure 3.45 and Figure 3.46 and solution at different time steps are shown in Figure 3.48.

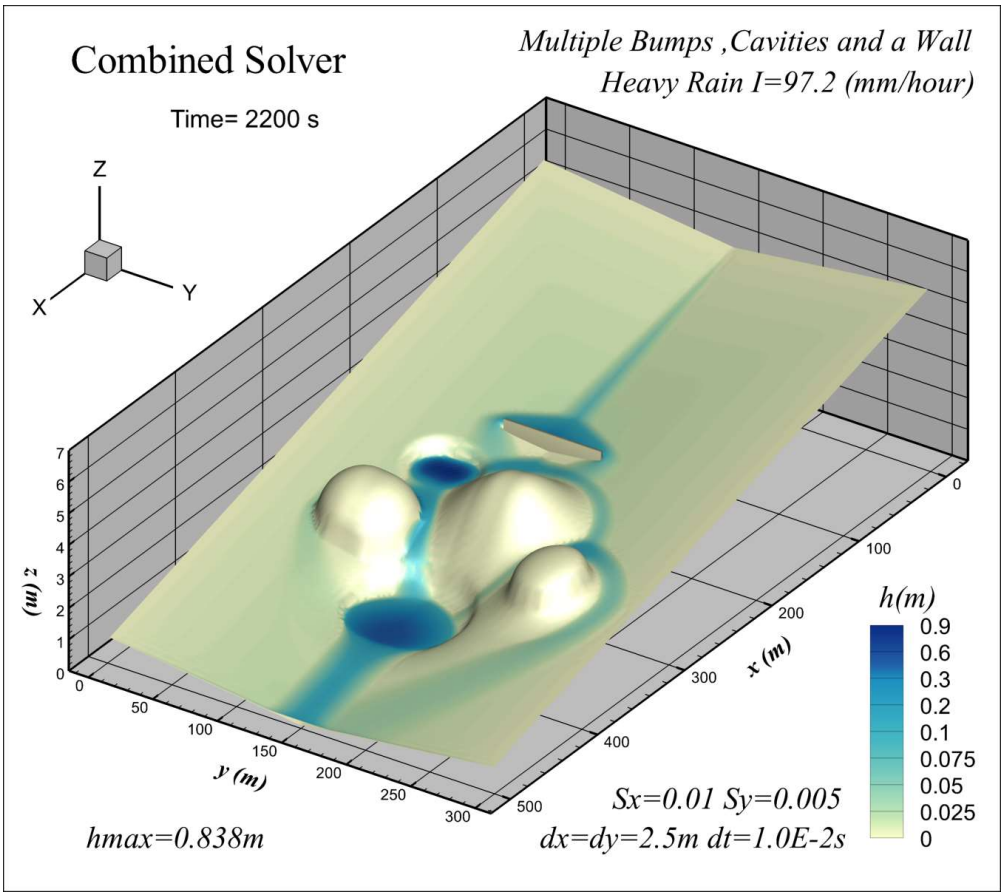

Figure 3.45 3D Water depth plot from combined solver for Test Case-5 at $t = 2200\ s$, downstream view.

Solver is handled wall type boundary condition in domain successfully. Solution is stable and continuity satisfied. Outlet hydrograph plot is compared with previous case solution and shown in Figure 3.47. Latency resulted from the wall can be seen in outlet hydrograph.

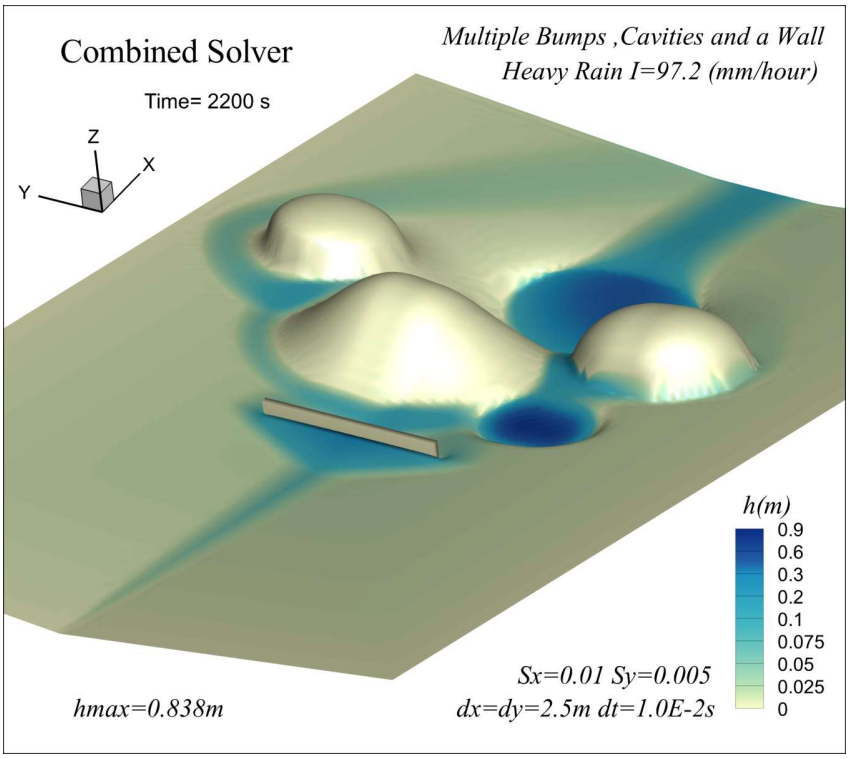

Figure 3.46 3D Water depth plot from combined solver for Test Case-5 at $t = 2200\ s$, upstream view.

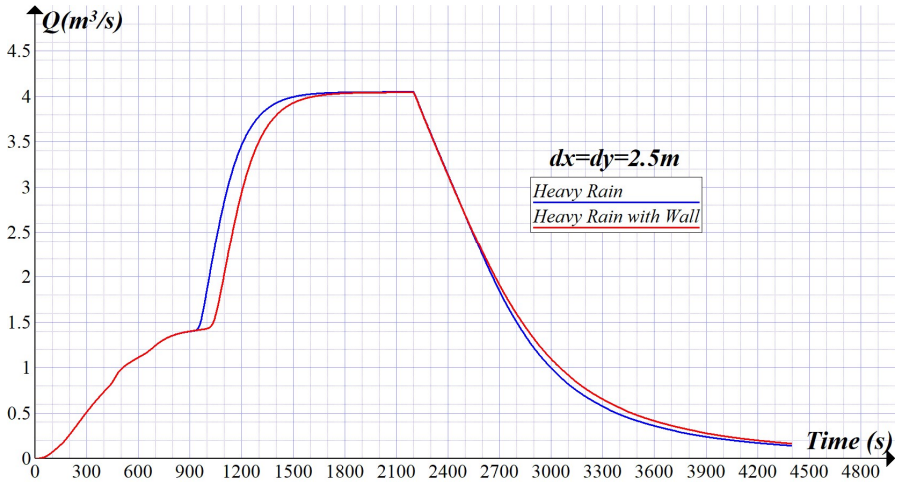

Figure 3.47 Outlet hydrographs for Test Case-5 compared to Test Case-4.

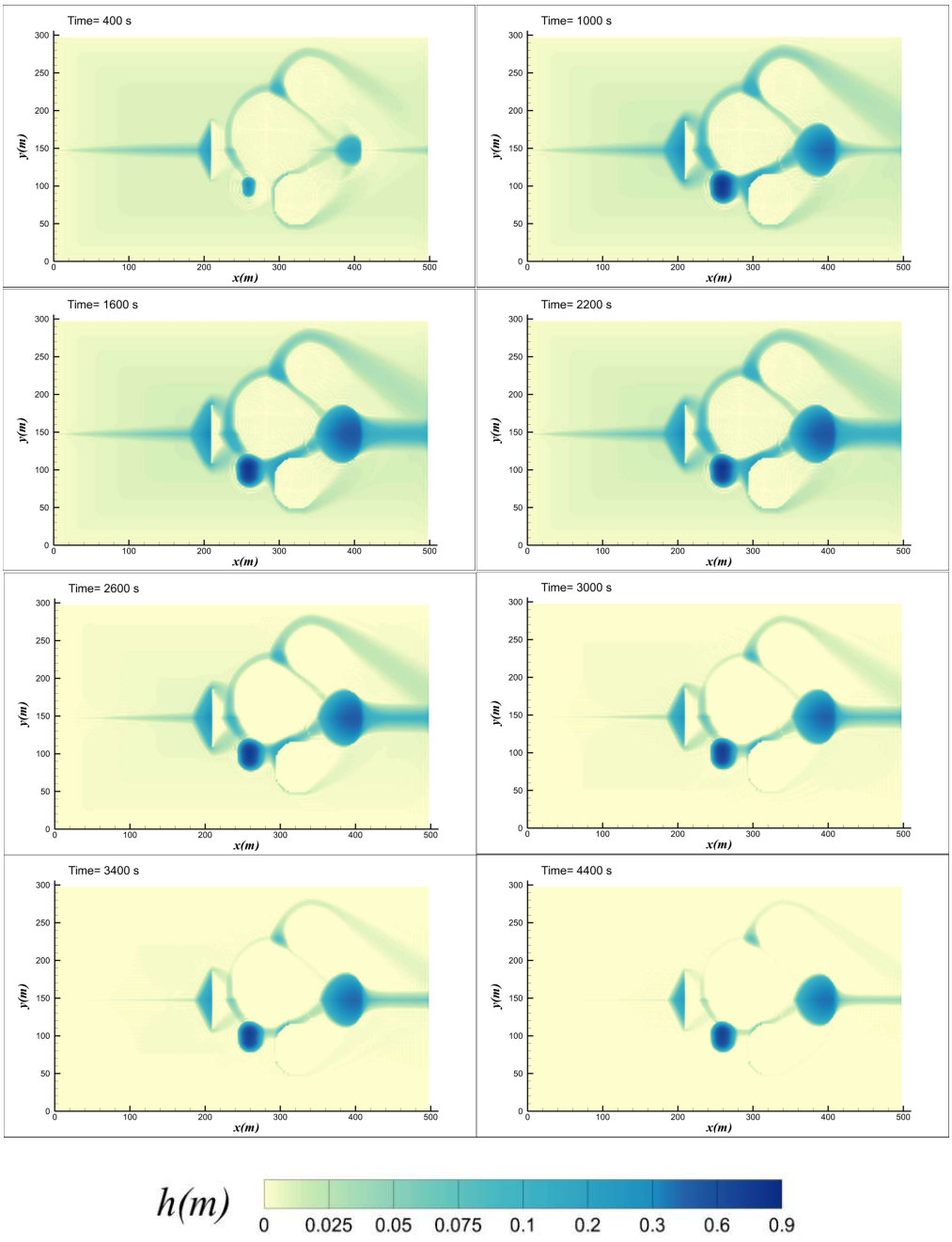

Figure 3.48 2D Water depth contour plots at different times for Test Case-5 from combined solver.

3.5 Accuracy and Grid Requirements

Numerical solutions for one-dimensional model is validated by comparing the results with analytical solution. It is seen that both upwind and central space solutions are in close agreement with analytical solutions. Both of this solutions give reliable results if stability and grid requirements are satisfied. Central space solution has higher order accuracy, and this higher accuracy leads more accurate results.

In two-dimensional solutions, Test Case-1 is solved for grid size as large as 10 m without any problem. Courant number limit for FTCS and combined solvers is 0.25 and for upwind solution is 0.2. Time step sizes violating that condition may cause instability or failure in the solution. Dynamic instability is only observed in local depressions in solutions with insufficient grid size and time step size.

3.6 Discussion of Results

While the two-dimensional solution can be obtained by forward time and central space solution, smaller grid sizes must be used especially in steeper slopes not to cause negative water depths. However, a flow direction sensitive solution like upwind scheme is much more convenient in order to avoid the negative water depths and allow bigger mesh sizes. However, upwind solution requires smaller time-step sizes to maintain numerical stability.

Combined solver which selectively using the central and upwind differencing methods is stable and accurate in all test cases. Solver avoids negative water depth calculation while keeping the numerical stability of central space solution. Both increasing and decreasing water profiles can be solved with this solver accurately.

CHAPTER 4

PARALLELIZATION AND SCALABILITY OF THE SOLVER

Scalability of a solution indicates the ability of an analysis to handle larger problems by adding more computational power. In sequential solutions, solution time of a problem is limited to power of a single thread in the processor. Adding extra processors to the system do not have any effect on the solution time. Thus, sequential solution of a large problem cannot be scaled and increase in domain size cause longer solution times. It makes the solver unpractical in large solutions. In parallelized solutions, in contrary to the sequential solution, the solution time can be reduced by adding processing power to the system to solve larger problems efficiently by dividing the processes to multiple independent chunks, and solution of these independent chunks can be shared between multiple threads of processors.

Parallelization of a solution can be managed using two different techniques, described by the memory configuration of the computer. In shared-memory systems, there is a single memory unit that can be accessible by each thread. In these systems, parallelization can be done with workshare between threads known as fork-join model, and there is no need for communication between threads. This technique is known as Multi-Processing parallelization and can be managed using OpenMP libraries.

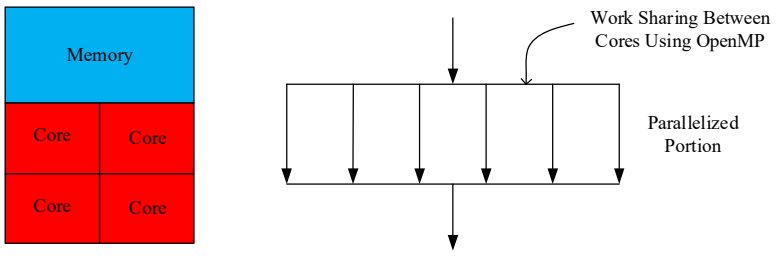

Figure 4.1 Sample configuration in Multi-Processing parallelization is given at the left and timeline of work-sharing process with OpenMP is given at the right.

In a distributed memory configuration, multiple independent computer units are used to work together in a single solution. Sample computer configuration is shown in Figure 4.2. In this system, each core can access its own memory and communication terminal.

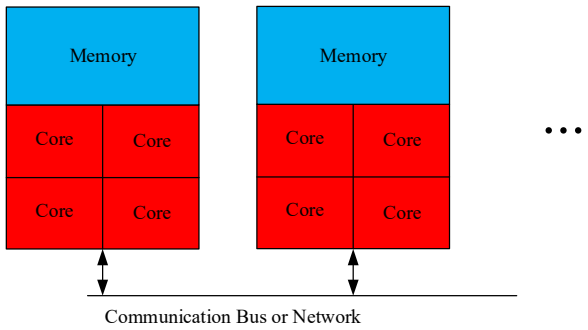

Figure 4.2 Sample configuration for a distributed memory system.

In this configuration, different portions of the domain are decomposed to independent units. Each unit only responsible for the solution of its own domain, and at the end of each time step they need to communicate and send their solutions at the interfaces to the neighbor units. This communication can be applied with MPI (Massage Passing Interface) and can be managed using OpenMPI libraries.

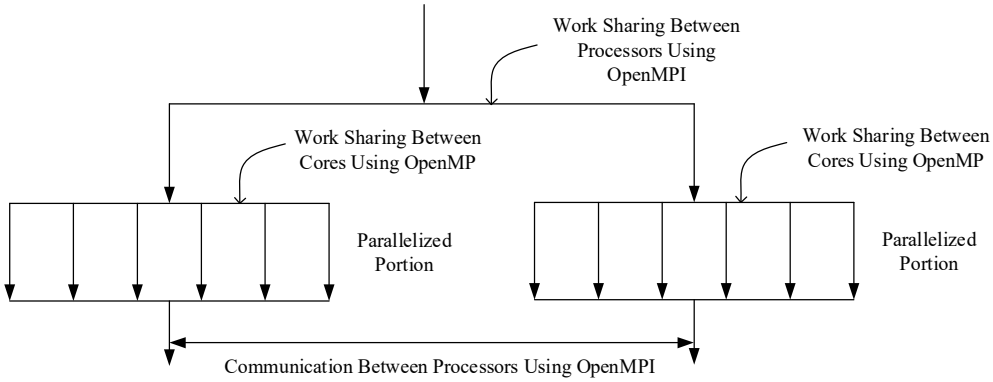

Figure 4.3 Timeline for hybrid parallelization. Workshare and communication between processors are handled by MPI and workshare between processor cores are handled by MP.

In the distributed-memory configuration, each unit stores variables of its own area. With the rough decomposition of solution areas each unit may have to send its solution on all over the interfaces to neighbor node. However, in particular to rainfall-runoff problem, the natural crest line of sub-basins can be selected as the decomposition boundaries using the topography as shown in Figure 4.4. As an assumption discharge at these crest lines can be neglected and this process may reduce the interfaces needs to be shared with neighbor. Using this technique, communication requirements can be reduced and leads less latency in solution. This technique is known as dynamic basin decomposition, and (Li et al., 2011) have developed a solver in this manner.

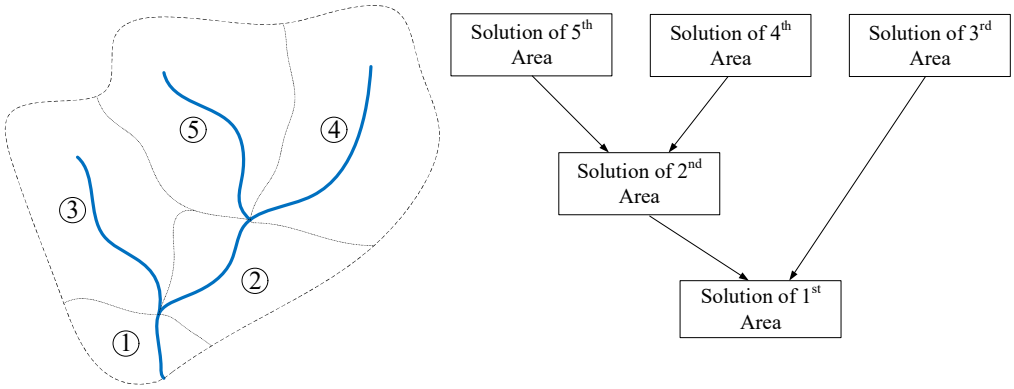

Figure 4.4 Sample solution domain which is divided to 5 unit with dynamic parallelization principle.

Moreover, in the solution of the system shown in Figure 4.4, 5th,4th,3rd area can be solved independently from the whole system and solution comes from these areas can be used for the solution of 2nd and 1st area in another time.

Speedup is the ratio of shortening of elapsed time resulted by parallel solution. Efficiency is the ratio of gained speedup per thread. Speedup and efficiency of a solution can be calculated as:

$$Speedup = \frac{Elapsed\ time\ in\ Sequential\ Solution}{Elapsed\ time\ in\ Parallel\ Solution} \tag{4.1}$$

$$Efficiency = \frac{Speedup}{No.of\ Threads} \tag{4.2}$$

There are two different approaches in the calculation of theoretical speedup by parallelization. From these calculations, theoretical solution time for an analysis can be predetermined.

The first approach is known as Ahmdals Law and it measures the speedup of a fixed size solution by increasing the number of processors. The Ahmdals law shows that the speedup is limited up to the time required by solution of the sequential portion. Theoretically, with an infinite number of processors and without physical limitations, solution time of a fixed size problem can be reduced up to the time required by the solution of sequential portion.

Theoretical speed up from Amdahl's law can be calculated as:

$$Speedup = \frac{1}{fs + fp/P} \tag{4.3}$$

where P is the number of processors used in solution, fs is the ratio of sequential portion of the code and fp is the ratio of parallelized portion of code.

$$fs + fp = 1 \tag{4.4}$$

The second approach is known as Gustafson's law also known as "Fixed time scaling". Gustafson's law measures the speed up of a variable size problem by increasing the number of processors with the same amount of increase in problem size. In variable size solutions, as domain gets larger, parallel portion of the solution increases. In this manner, the processor count can be increased with the domain size to keep the solution time equal. Analysis developed in the scope of this thesis has variable size and behavior in this approach is more important.

Theoretical speed up from Gustafson's law can be calculated as:

$$Speedup = fs + fp * P \tag{4.5}$$

Note that, in practice, as the number of cores increases parallel initialization, memory access time and communication times also increases, so that the real speedup will

never reach to that theoretical speedup. Also, cash memory size of the CPU, memory access time of system, and read-write speed of hard disk in the system are some physical limitations of computers, and these physical limitations directly affect the solution time. Moreover, modern CPU's reduces its frequency when its heat exceeds a certain limit as a safety feature.

4.1 Parallel Speedup Tests

In order to test the parallelization of the solver, a bunch of two-dimensional test cases are performed. In all parallel speedup tests, without any obstruction, the model has only slope in x-direction and for variable domain size tests, the domain is enlarged only in y-direction to eliminate the shape effects. In all solutions, 50000 iterations performed. All solutions are performed without writing any data to the hard disk in main iteration loop to eliminate the hard disk speed limitation and input, output routines that are not parallelized. Also, all solutions are obtained one by one with enough resting and cooling time between solutions.

For the solution of parallel speedup tests, an HP workstation with 24 core 48 thread Intel Xeon E5-2680 V3 2.50GHz processor is used.

4.1.1 Speedup and Efficiency with Increasing No. of Threads

In order to test the parallelization of the solver in Ahmdal's approach, model is solved for two different domain size with increasing number of threads. Small solution is obtained using 200x480 domain and large solution is obtained using 200x1920 domain.

Results in Table 4.1 are plotted in Figure 4.5 with ideal curves calculated from Amdahl's law. It is seen that the solver is 95% to 97.5% parallel in the solution of large domain and 92.5% to 95% parallel in the solution of small domain. It is seen that the increase in domain size increases the parallel portion of the solution.

Table 4.1 Speedup and efficiency with increasing number of threads.

No of Threads	*200x480 Domain*			*200x1920 Domain*		
	Elapsed Time(s)	*Speedup*	*Efficiency*	*Elapsed Time(s)*	*Speedup*	*Efficiency*
Sequential	302.42	1	1	1253.48	1.000	1.000
1	320.50	0.944	0.944	1296.83	0.967	0.967
2	159.12	1.901	0.950	648.29	1.934	0.967
4	90.34	3.348	0.837	353.84	3.543	0.886
8	52.23	5.790	0.724	190.48	6.581	0.823
16	37.47	8.071	0.504	130.21	9.627	0.602
24	35.30	8.567	0.357	106.47	11.773	0.491
32	33.76	8.958	0.280	91.1	13.759	0.430
48	36.29	8.333	0.174	84.96	14.754	0.307

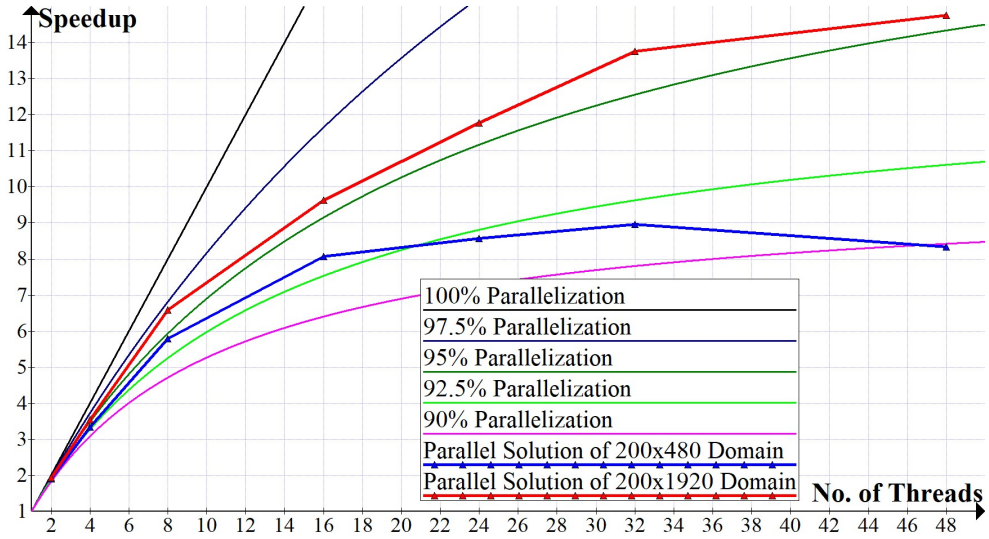

Figure 4.5 Speedup and efficiency with increasing number of threads.

4.1.2 Speedup and Efficiency with Increasing Domain Size in the Same Proportion of No of Threads

In order to test the parallelization of the solver in Gustafson's approach, The same problem is solved with increasing domain size in the same proportion of number of threads.

Table 4.2 Speedup and efficiency with increasing domain size and number of threads.

Grid Size	*Number of Nodes*	*Elapsed Time in Sequential Solution (s)*	*No. of Threads in Parallel Solution*	*Elapsed Time in Parallel Solution (s)*	*Speed up*	*Efficiency*
200x120	24000	74.96	Sequential	-	1	1
200x240	48000	149.00	2	83.17	1.791	0.896
200x480	96000	300.22	4	89.64	3.349	0.837
200x960	192000	644.55	8	97.93	6.582	0.823
200x1440	288000	928.89	12	98.41	9.439	0.787
200x1920	384000	1250.97	16	115.30	10.850	0.678
200x2400	480000	1617.90	20	135.13	11.973	0.599
200x2880	576000	1937.81	24	143.85	13.471	0.561

Results in Table 4.2 are plotted in Figure 4.6 with ideal curves calculated from Gustafson's law. It is seen that the solver is about 80% parallel in Gustafson's approach. It is seen that the solution of larger than the 288000 nodes leads performance issues. It may probably result from the CPU cash memory size limitation. In larger solutions, allocated variable arrays may not fit into the cash memory and memory access time latency. To overcome this limitation the solver can be further optimized for system by dividing the arrays to multiple chunks.

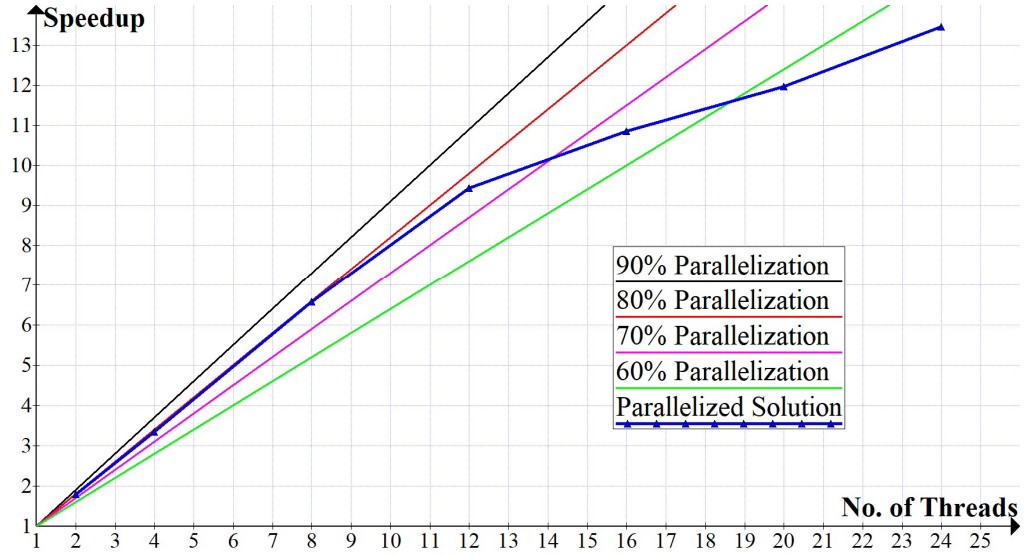

Figure 4.6 Parallelized solution with increasing domain size in the same proportion of the no. of threads.

CHAPTER 5

GEOGRAPHICAL CALCULATIONS

This chapter is about the geographical calculations that are required in the preprocess session before the numerical solution of the governing equations of shallow flows. Flow domain is described by topography and topographic data is obtained from geographical maps. Location of all computational nodes in the Cartesian mesh system used by the solver must be calculated or converted from the geographical coordinates.

5.1 Geodesy

Geodesy is the science field that goals to accurately describe the shape, motion, and size of the Earth. As the Earth is home for all humanity, it is crucial to know the shape and define a certain location on that shape.

5.1.1 The shape of the Earth and Geographic Models

Shape of the Earth is defined as a geoid at sea level all over the world. This sea level estimation is based on gravity force measurements on the Earth's surface. However, the gravity force on the Earth's surface is not homogeneous. So that the sea level on the Earth's surface has some imperfections. Because of that, calculations based on geoidal shape is over complicated. Thus, for more than hundreds of years, geodesists improved some approximated models to describe the shape of the Earth.

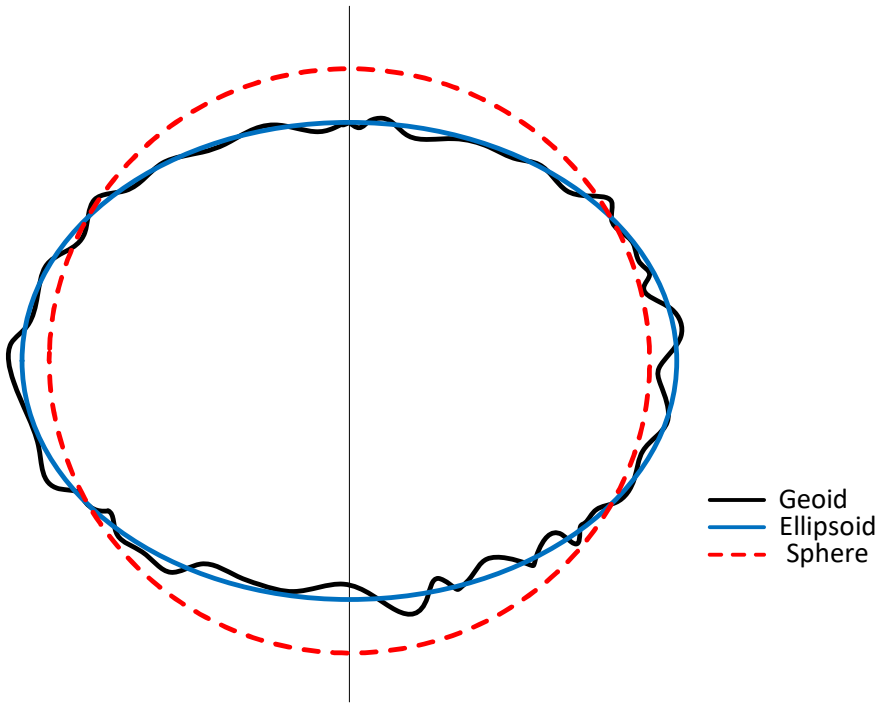

Figure 5.1 Comparison of Geoid, Ellipsoid, and Sphere

As can be seen in Figure 5.1, rough estimation for the shape of the Earth is a sphere. For short distances, the spherical model offers simple calculation methods with reasonable accuracy. For more detailed and accurate calculations, the ellipsoidal model is improved.

5.1.1.1 Spherical Surface Model

The spherical model is the simplest approximation for the shape of the Earth. Calculations on that model are more straightforward compared to calculations on the ellipsoidal model, and the measurements are acceptable for short distances. As the distance increases, the difference between measurements and calculations increases. Thus, it is not convenient to use that model on large areas on the Earth. Spherical trigonometry techniques are used for the calculations. For example, Haversine's formula is a formulation to calculate the length of an arc on a sphere, and it is used for the calculation of the distance between two points on the surface of the Earth.

5.1.1.2 Ellipsoidal Surface Model

The ellipsoidal model is an accurate model that describes the shape of the Earth for lots of applications. With the help of current computer technology, most of our models are based on the ellipsoidal model. Calculations for the ellipsoidal model based on ellipsoidal trigonometry and these calculations are much more complicated compared to the calculations for the spherical model.

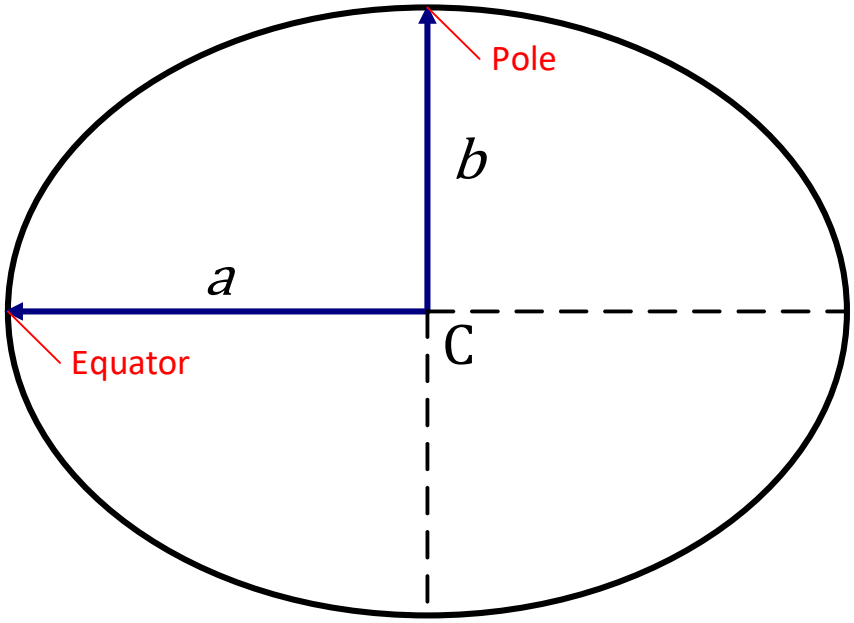

Figure 5.2 Vertical Cross-section of Ellipsoidal Earth

The approximation of an ellipsoid requires two different radiuses. As can be seen in Figure 5.2 a is the equatorial radius (semi-major axis) and b is the polar radius (semi-minor axis).

Flattening and eccentricity of an ellipsoid are the ratios of the equatorial and the polar radiuses and can be calculated from Equations (5.1), (5.2) and (5.3).

$$f = 1 - \frac{b}{a} \tag{5.1}$$

$$e^2 = 1 - \frac{b^2}{a^2} = f(2 - f) \tag{5.2}$$

$$e'^2 = \frac{a^2}{b^2} - 1 = \frac{f(2-f)}{(1-f)^2} \tag{5.3}$$

where a is the equatorial radius, b is the polar radius, f is the flattening ratio, e^2 is the first eccentricity squared and e'^2 is the second eccentricity squared values.

5.1.1.2.1 Geodetic Datums

Calculations, measurements, and defining a point on the surface of an ellipsoid requires a datum point and at least a radius and flattening ratio or an eccentricity value. In order to define the shape of the Earth, geodesists improve approximated ellipsoids and the most common ellipsoidal model is WGS84 (World Geodetic System). This ellipsoid is generally recognized by most of the world. In this geodetic system, the equatorial radius is about 6378137.0 m and the polar radius is about 6356752.3 m and inverse flattening $(1/f)$ is 298.257223563. Also, a mean radius is defined for calculations based on the spherical earth model. That is 6371008.8 m and can be calculated from:

$$R = \frac{2a + b}{3} \tag{5.4}$$

where a is the equatorial radius, b is the polar radius.

There are different ellipsoids to use in different portions of the Earth. For example, while WGS 84 is a worldwide applicable ellipsoid, ED50 ellipsoid is improved especially for use in Europe for better accuracy. Some other datums are listed in Table 5.1.

Table 5.1 Datum used in geographic coordinate systems. (Grafarend & Krumm, 2006)

Name	*a (Equatorial Radius) m*	e^2 *(First Eccentricity Squared)*	*N*
WGS 84			
EUREF89	6378137	0.00669438	10
ETRS89			
ED50	6378388	0.00672267	
WGS 72	6378135	0.006694318	
WGS 66	6378145	0.006694542	
WGS 60	6378165	0.006693422	
GRS 1980	6378137	0.00669438	
GRS 1967	6378160	0.006694605	

5.1.2 Geographic Coordinate Systems

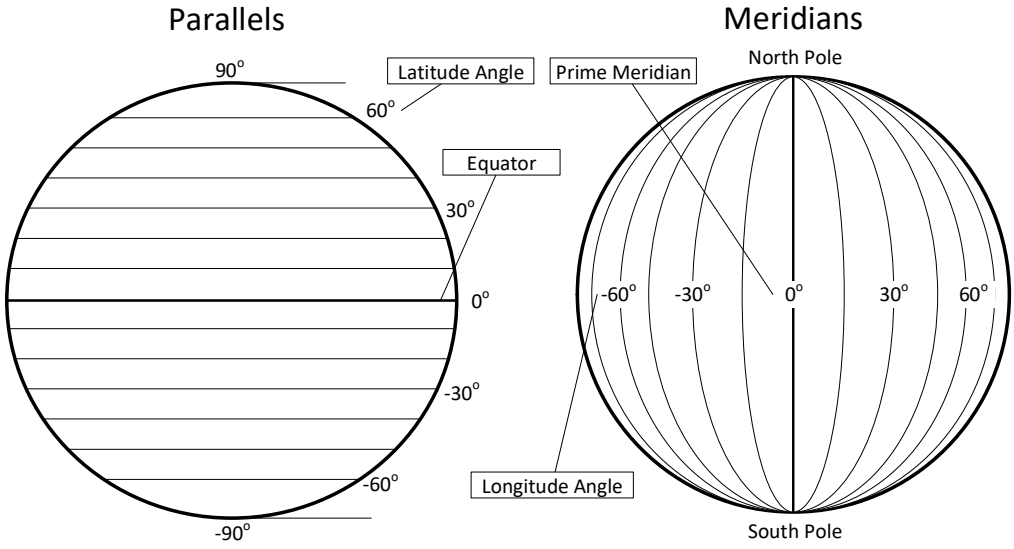

Figure 5.3 Parallels and Meridians

The geographic coordinate system is an angular coordinate system that describes a certain location using two different angles named as latitude and longitude. The latitudinal lines are the horizontal lines parallel to the equator and the longitudinal lines are perpendicular to the latitudinal lines and all of the longitudinal lines are passing through the poles shown in Figure 5.3. In this model latitudinal lines range from -90 to 90 and longitudinal lines range from -180 to 180, in some books longitudinal lines may range from 0 to 360, or instead of negative sign North (N), South (S), East (E), West (W) prefixes might be used with angles.

5.1.3 Elevation

A geographical location indicates only the horizontal location of a point on the surface of the model. There is a third dimension which is the elevation, the perpendicular distance from the reference surface of the model.

There are different elevation descriptions as shown in Figure 5.4. The first one is the elevation from sea level (geoid) named as orthometric height or from reference ellipsoid named as ellipsoid height. The height difference between ellipsoid and geoid is named as geoid height.

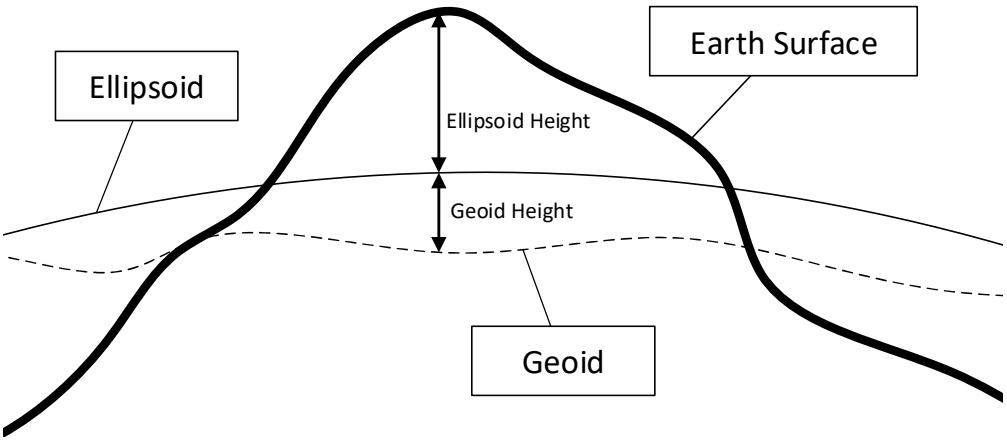

Figure 5.4 Elevation

Satellite-based elevation models indicate the ellipsoid height. As the calculation zones in this thesis are relatively small areas, relative height errors that come from the ellipsoidal approximation between nodes are assumed negligible.

5.1.4 Bearing Angle

Bearing angle is the angular definition of a direction on the surface of the Earth. This angle always has a positive value, and the positive direction is defined in the clockwise direction between the direct path to the north pole and the direction vector on the surface. Bearing angle can be calculated from two different locations, a start and an end location.

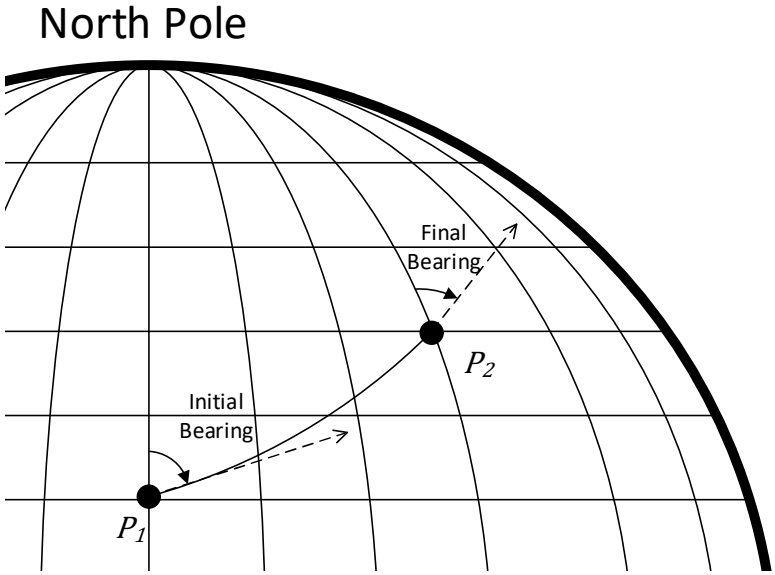

Figure 5.5 Initial and final bearing angle

As can be seen in Figure 5.5, bearing angle at the starting point (P_1) on the path is named as the initial bearing. Note that the bearing angle at the endpoint (P_2) or any other point on the path is different from the initial bearing because of the shape of the Earth unless the two points are on the same longitudinal line.

5.2 Geographic Calculations

5.2.1 Calculation of Distance

There are different algorithms for the calculation of the distance between two points on the Earth.

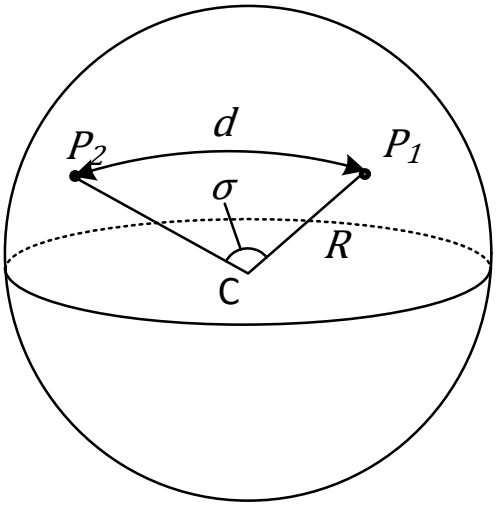

Figure 5.6 Distance between two points on the surface of the sphere

In Figure 5.6, C is the center and R is the radius of the model. The length of the arc between points P_1 and P_2 is d and the central angle of that arc is σ. The length of an arc in the spherical model can be calculated as:

$$d = \sigma R \tag{5.5}$$

5.2.1.1 Haversine Formula

Haversine formulation is an analytical calculation of the distance between two points on a spherical surface that comes from spherical trigonometry. As error for small distances assumed negligible, this formulation is used to calculate the distance between two close points.

Distance between two points can be calculated from the Haversine formula described by the equations below (Veness, 2002).

$$hav(\sigma) = h = hav(\varphi_2 - \varphi_1) + \cos(\varphi_1)\cos(\varphi_2)\, hav(\lambda_2 - \lambda_1) \quad (5.6)$$

$$hav(\theta) = \sin^2\left(\frac{\theta}{2}\right) = \frac{1 - \cos(\theta)}{2} \quad (5.7)$$

$$\sigma = archav(h) = 2\, arcsin\left(\sqrt{h}\right) \quad (5.8)$$

More explicitly;

$$\sigma = 2\, arcsin\left(\sqrt{hav(\varphi_2 - \varphi_1) + \cos(\varphi_1)\cos(\varphi_2)\, hav(\lambda_2 - \lambda_1)}\right) \quad (5.9)$$

$$= 2\, arcsin\left(\sqrt{\sin^2\left(\frac{\varphi_2 - \varphi_1}{2}\right) + \cos(\varphi_1)\cos(\varphi_2)\sin^2\left(\frac{\lambda_2 - \lambda_1}{2}\right)}\right) \quad (5.10)$$

where λ_1 and φ_1 are the longitude and the latitude of the first point, λ_2 and φ_2 are the longitude and the latitude of the second point, and the distance between points can be calculated by using central angle σ from Equation (5.5).

5.2.1.2 Spherical Law of Cosines

Spherical law of cosines is also a method for the calculation of the distance between two points on the spherical surface.

Distance between two points can be found from (Veness, 2002):

$$\sigma = \arccos(\sin\varphi_1 \sin\varphi_2 + \cos\varphi_1 \cos\varphi_2 \cos\Delta\lambda) \quad (5.11)$$

where λ_1 and φ_1 are the longitude and the latitude of the first point, λ_2 and φ_2 are the longitude and the latitude of the second point, and the distance between points can be calculated by using central angle σ from Equation (5.5).

Note that, for short distances $cos\Delta\lambda$ term in Equation (5.11) becomes about 0.999999… . In order to avoid large roundoff errors in calculation, instead of a 32bit floating point variable, a 64bit double precision variable should be used. The

Haversine formula offers more precise calculation for short distances because of the use of sine function instead of cosine.

5.2.1.3 Lambert's Formula for Calculating Long Distances

An ellipsoidal model represents the shape of the Earth much accurately. For short distances, the difference between calculations on spherical and ellipsoidal models is assumed negligible. However, as the distance increases the error comes from the approximation increases. Because of that, Lambert's formula which is based on ellipsoidal approximation is more suitable for calculations between widely separated points.

Distance between two widely separated points can be calculated accurately from the Equation (5.16) (Lambert, 1942).

$$\tan(\beta) = (1 - f)\tan(\phi) \tag{5.12}$$

For the solution of the lamberts formula, the first operation is the reduction of the latitudes ϕ_1 and ϕ_2 to β_1 and β_2 by using Equation (5.12).

$$P = \frac{\beta_1 + \beta_2}{2} \qquad Q = \frac{\beta_2 - \beta_1}{2} \tag{5.13}$$

$$X = (\sigma - sin\sigma)\frac{\sin^2 P \cos^2 Q}{\cos^2 \frac{\sigma}{2}} \tag{5.14}$$

$$Y = (\sigma + sin\sigma)\frac{\cos^2 P \sin^2 Q}{\sin^2 \frac{\sigma}{2}} \tag{5.15}$$

$$d = a\left(\sigma - \frac{f}{2}(X + Y)\right) \tag{5.16}$$

where σ is the central angle, and it can be calculated from Equation (5.10) or (5.11), f is the flattening ratio of the ellipsoid, a is the equatorial radius of the globe, and d is the distance.

5.2.2 Calculation of Bearing Angle

The bearing angle of a path between two locations can be found from (Veness, 2002):

$$\theta = atan2(\sin(\Delta\lambda)\cos(\varphi_2), \cos(\varphi_1)\sin(\varphi_2) - \sin(\varphi_1)\cos(\varphi_2)\cos(\Delta\lambda)) \quad (5.17)$$

where φ_1 is the latitude of the first point, φ_2 is the latitude of the second point, $\Delta\lambda$ is the difference in longitude, and θ is the initial bearing value.

Note that, instead of $arctan$ function, $atan2$ function which can return values from all four quadrants is used.

Since atan2 returns values from -180 to +180 in order to normalize the value the equation below is used.

$$\theta = (\theta + 360)\ mod\ 360 \quad (5.18)$$

In order to find the final bearing angle if it is required, bearing angle from final to start point must be calculated in the reverse direction, and then the conversion equation given below is applied.

$$\theta = (\theta + 180)\ mod\ 360 \quad (5.19)$$

Note that mod in Equation (5.18) and (5.19) is the modulo operation that returns reminder of the division. Value at the left side of the operation is dividend and the right side of the operator is the divisor term.

5.2.3 Calculation of Intermediate Points

Intermediate points are the points located on the shortest path between two points. The location of an intermediate point can be found from Equations (5.25) and (5.26) (Veness, 2002).

$$a = \frac{\sin\big((1-w)\sigma\big)}{\sin(\sigma)} \quad (5.20)$$

$$b = \frac{\sin(w\sigma)}{\sin(\sigma)} \tag{5.21}$$

$$x = \mathrm{a} * \cos(\varphi_1)\cos(\lambda_1) + b * \cos(\varphi_2)\cos(\lambda_2) \tag{5.22}$$

$$y = \mathrm{a} * \cos(\varphi_1)\sin(\lambda_1) + b * \cos(\varphi_2)\sin(\lambda_2) \tag{5.23}$$

$$z = a * \sin(\varphi_1) + b * \sin(\varphi_2) \tag{5.24}$$

$$\varphi_i = atan2(z, \sqrt{x^2 + y^2}) \tag{5.25}$$

$$\lambda_i = atan2(y, x) \tag{5.26}$$

where $\lambda_!$ and φ_1 are the longitude and the latitude of the first point, λ_2 and φ_2 are the longitude and the latitude of the second point, σ is the angular difference, w is the distance ratio (must be in between 0 and 1, 0 for point 1, 1 for point 2), λ_i and φ_i are the longitude and the latitude of the intermediate point.

5.2.4 Calculation of Midpoint

Midpoint is also an intermediate point at the center of the path between two points. Calculation for intermediate points can be simplified by taking w value as 0.5 to find the midpoint. The equation for midpoint is simplified from the intermediate point equations, and it can be calculated from Equations (5.29) and (5.30) (Veness, 2002)

$$B_x = \cos(\varphi_2)\cos(\Delta\lambda) \tag{5.27}$$

$$B_y = \cos(\varphi_2)\sin(\Delta\lambda) \tag{5.28}$$

$$\varphi_m = atan2\left(\sin(\varphi_1) + \sin(\varphi_2), \sqrt{(\cos(\varphi_1) + B_x)^2 + B_y^2}\right) \tag{5.29}$$

$$\lambda_m = \lambda_1 + atan2(B_y, \cos(\varphi_1) + B_x) \tag{5.30}$$

5.2.5 Destination Point

Destination point location from a location, a bearing angle, and a distance can be found from Equations (5.31) and (5.32) (Veness, 2002).

$$\varphi_2 = \arcsin(sin(\varphi_1)\, cos(\sigma) + cos(\varphi_1)\, sin(\sigma)\, cos(\theta)) \tag{5.31}$$

$$\lambda_2 = \lambda_1 + atan2(\sin(\theta)\sin(\sigma)\cos(\varphi_1), \cos(\sigma) - \sin(\varphi_1)\sin(\varphi_2)) \tag{5.32}$$

where $\lambda_!$ and φ_1 are the longitude and the latitude of the first point, σ is the central angle, θ is the bearing angle, λ_2 and φ_2 are the longitude and the latitude of the destination point.

5.3 Projection Techniques

Projection techniques are used to transform the three dimensional surface of the model to a two dimensional flat surface for visualization and mapping purposes. Locations on those projections named as rectangular coordinates as it is a two-dimensional x-y plane version of the model. However, there is no way to project without and error. So that different projection techniques can be used to project different portions of the Earth. There are lots of different projection techniques developed specifically for different portions of the Earth's surface. Each projection aims to create accurate representation as possible and each of them has different approaches and advantages. In this thesis, three of them are used. And the dimensions of the projected map is metric. These projection techniques are also used for calculation besides the visualization.

5.3.1 Cylindrical Projection

Cylindrical projection is the projection of the Earth's surface to a cylinder as shown in Figure 5.7. In this study, equirectangular cylindrical projection is used. Projection cylinder in equirectangular projection intersects at two parallels on the spherical

surface of the Earth known as standard parallels, and the scale of that projection is true on that standard parallels. All meridians and parallels become straight lines perpendicular to each other.

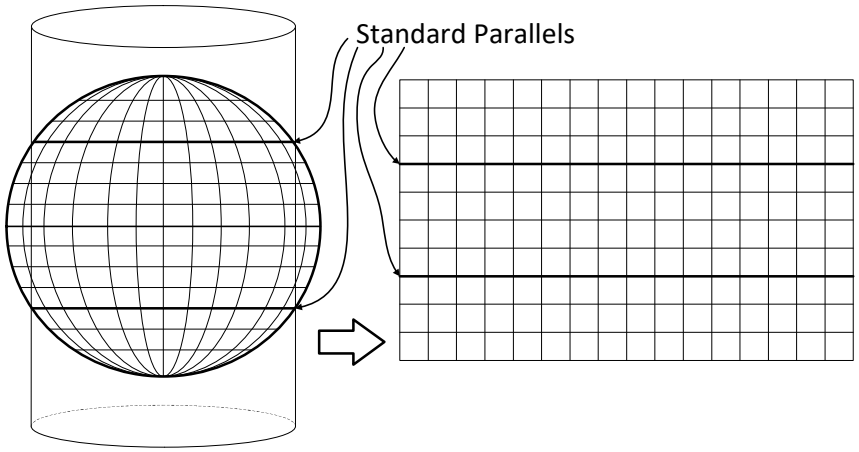

Figure 5.7 Cylindrical Projection

Area between the standard parallels projected in the negative direction which creates squishing effect in the east-west direction, whereas areas between poles and the standard parallels projected in the positive direction which creates stretching effect in the east-west direction. Deformation on the projection rises as the distance from the standard parallels increases and the pole points become to two lines cover the top and the bottom side of the map.

Conversion from a point location on the spherical surface to rectangular coordinate on cylindrical projection plane can be done by using Equations (5.33) and (5.34) (Snyder, 1987).

$$x = R(\lambda - \lambda_0)cos\varphi_1 \tag{5.33}$$

$$y = R(\varphi - \varphi_1) \tag{5.34}$$

Conversion from the rectangular coordinate of a point on cylindrical projection plane to location on the spherical surface can be done by using Equations (5.35) and (5.36) (Snyder, 1987).

$$\lambda = \frac{x}{Rcos\varphi_1} + \lambda_0 \tag{5.35}$$

$$\varphi = \frac{y}{R} + \varphi_1 \tag{5.36}$$

where λ is the longitude and φ is the latitude of the location to projection, φ_1 is the standard parallel where the scale of the projection is true, λ_0 is the central meridian of the map, R is the radius of the globe, and x and y are the horizontal and vertical rectangular metric coordinates of the projected location on the map.

5.3.2 Conic Projection

As a conic projection, Lambert's conformal conic projection (LCC) is used. For this type of projection, the surface of the model is projected to a cone that touches to two standard parallels as shown in Figure 5.8. This projection can be done using both spherical and ellipsoidal models. In this study, only the spherical formulation is used for only visualization.

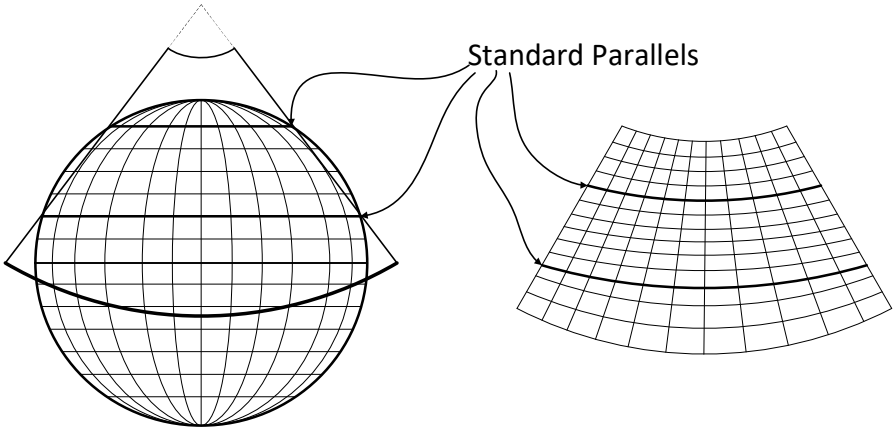

Figure 5.8 Conic Projection

Conversion from a point location on the spherical surface on rectangular coordinate of conic projection plane can be done using Equations (5.37) and (5.38) (Snyder, 1987).

$$x = \rho \sin\big(n(\lambda - \lambda_0)\big) \tag{5.37}$$

$$y = \rho_0 - \rho \cos\big(n(\lambda - \lambda_0)\big) \tag{5.38}$$

where:

$$F = \left(\cos(\varphi_1)\tan^n\left(\frac{\pi}{4} + \frac{\varphi_1}{2}\right)\right)/n \tag{5.39}$$

$$n = \ln(\cos(\varphi_1) / \cos(\varphi_2))/\ln(\tan\left(\frac{\pi}{4} + \frac{\varphi_2}{2}\right) / \tan(\frac{\pi}{4} + \frac{\varphi_1}{2})) \tag{5.40}$$

$$\rho = RF/\tan^n\left(\frac{\pi}{4} + \frac{\varphi}{2}\right) \tag{5.41}$$

$$\rho_0 = RF/\tan^n\left(\frac{\pi}{4} + \frac{\varphi_0}{2}\right) \tag{5.42}$$

where φ_0 and λ_0 are the latitude and longitude of the origin point on rectangular coordinates of the projection. φ_1 and φ_2 are the standard parallels.

Conversion from rectangular coordinate of a point on conic projection plane to location on the spherical surface can be done using Equations (5.37) and (5.38) (Snyder, 1987).

$$\varphi = 2\,arctan\left(\frac{RF}{\rho}\right)^{1/n} - \frac{\pi}{2} \tag{5.43}$$

$$\lambda = \lambda_0 + \frac{\theta}{n} \tag{5.44}$$

where

$$\rho = sign(n)\sqrt{x^2 + (\rho_0 - y)^2} \tag{5.45}$$

$$\theta = arctan\left(\frac{x}{\rho_0 - y}\right) \tag{5.46}$$

5.3.3 Universal Transverse Mercator Projection (UTM)

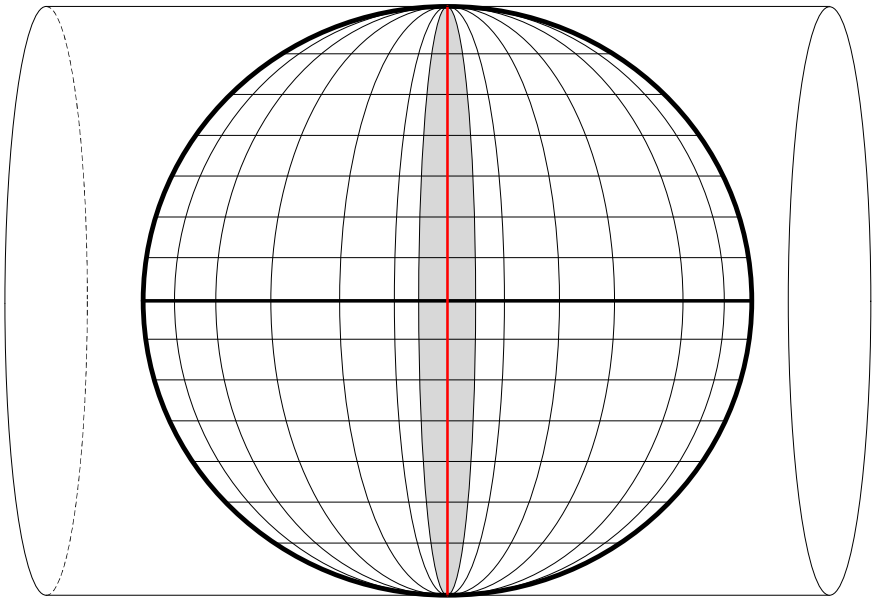

Figure 5.9 Universal Transverse Mercator Projection

UTM projection as shown in Figure 5.9 is a different projection technique that has a true scale on meridians instead of on parallels. It aims to generate accurate maps with reliable distances between different points. For this projection technique, the shape of the Earth is vertically divided into 60 different zones, as shown in Figure 5.10. As there are 360 meridians and all system is divided into 60 different zones, each zone includes 6 meridians. The 3rd meridian from the right (at center) at each zone named as the center meridian of that zone. Each zone projected to a flat surface individually by projecting it on a cylindrical shape that touches to the central meridian. In this projection meridians are not straight lines, they are complex curves, except the central meridians (Snyder, 1987).

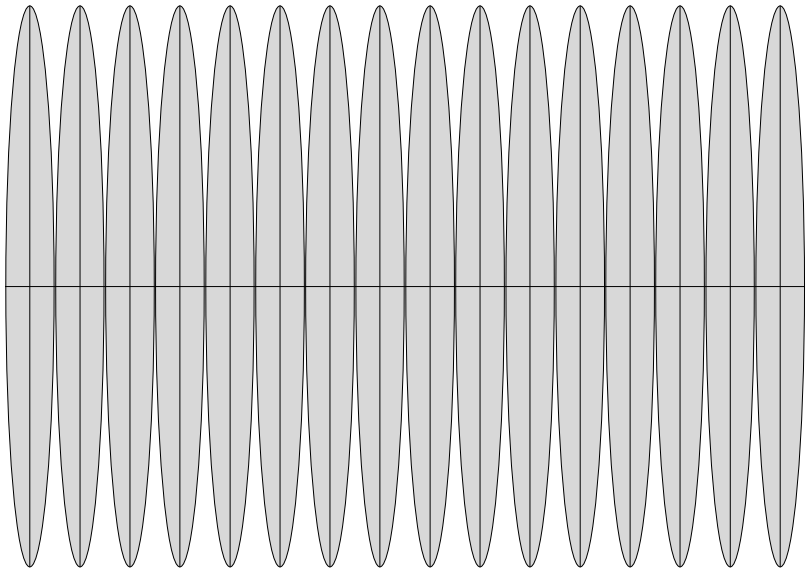

Figure 5.10 Different zones for UTM projection

Definition of a location on that projection requires easting, northing, zone number, and zone letter values as shown in Figure 5.11.

Figure 5.11 Definition of a UTM location

In order to describe all locations in positive quantity, center (0,0) locations in zones are defined at 500 km west from center meridian at the equator, known as false easting. Also, in order to make all northing values positive in the south hemisphere center location is defined at 10000 km south from the equator. It means the zero point for the south portion of that zone is 10000 km south to the north zero point, known as false northing, as shown in Figure 5.12.

$$x = x' + 500{,}000\ m \tag{5.47}$$

$$y = \begin{bmatrix} y' & , \ in\ northern\ hemisphere \\ y' + 10{,}000{,}000\ m & , \ in\ southern\ hemisphere \end{bmatrix} \tag{5.48}$$

where x and y are the easting and northing values respectively. x' and y' values are the coordinates from the false center at the junction of the equator and center meridian.

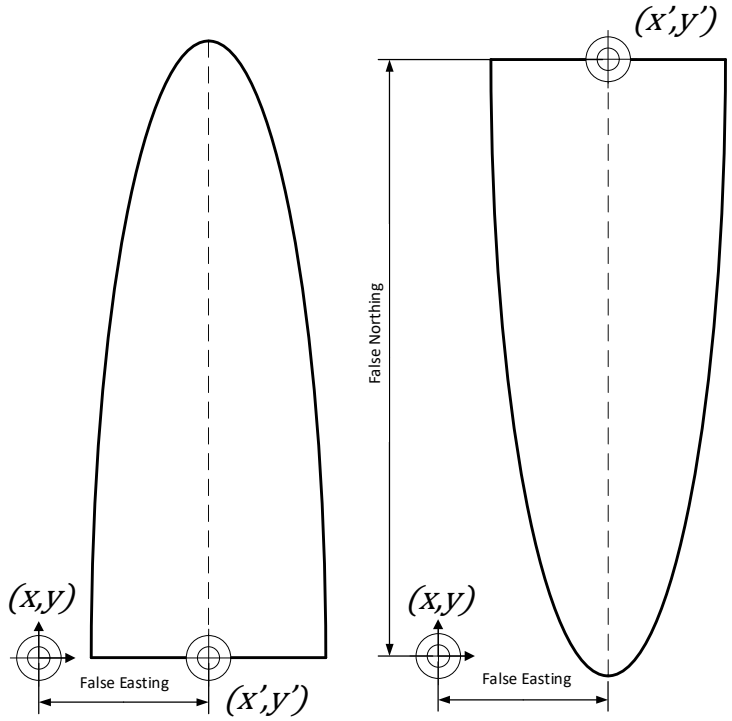

Figure 5.12 False easting and false nothing for northern hemisphere at the left and southern hemisphere at the right

As the maximum angular distance from the standard line for all of the map is 3 degrees maximum, distortion of the projection is much less compared to the other projections. Thus, calculations on that projection are more reliable if both points are in the same zone.

Central meridian (origin longitude) λ_0 can be found from Equation (5.49).

$$\lambda_0 = (ZoneNumber - 1)6 - 180 + 3 \tag{5.49}$$

Zone number of a location can be found from Equation (5.50).

$$ZoneNumber = \frac{\lambda + 180}{6} + 1 \quad (5.50)$$

However, there are some exceptions

- The area between latitude 58 and 54.5 and longitude 8 and 13 is in zone 32.
- The area between latitude 56 and 64 and longitude 3 and 12 is in zone 32,
- The area between latitude 72 and 84 and longitude 0 and 9 is in zone 31,
- The area between latitude 72 and 84 and longitude 9 and 21 is in zone 33,
- The area between latitude 72 and 84 and longitude 21 and 33 is in zone 35,
- The area between latitude 72 and 84 and longitude 33 and 42 is in zone 37,

Conversion can be done with both ellipsoidal and spherical models. In this thesis, all the conversion is made by using the ellipsoidal model equations.

5.3.3.1 UTM Projection Based on Spherical Model

Conversion from a point location on the spherical surface to the rectangular coordinate of UTM projection can be done using Equations (5.51) and (5.52). After the conversion, easting and northing values must be normalized by using Equations (5.47) and (5.48) (Snyder, 1987).

$$x' = Rk_0 \operatorname{arctanh}(B) \quad (5.51)$$

$$y' = Rk_0 \left(\arctan(tan\phi/\cos(\lambda - \lambda_0)) - \phi_0\right) \quad (5.52)$$

$$k = k_0/(1 - B^2)^{1/2} \quad (5.53)$$

where

$$B = \cos(\phi)\sin(\lambda - \lambda_0) \quad (5.54)$$

Conversion from the rectangular coordinate of a point on UTM projection to the location on the spherical surface can be done using Equations (5.55) and (5.56). Before the conversion, false center coordinates must be calculated using Equations (5.47) and (5.48) in reverse (Snyder, 1987).

$$\phi = \arcsin(\sin(D)/\cosh(x'/(Rk_0))) \quad (5.55)$$

$$\lambda = \lambda_0 + \arctan(sinh(x'/(Rk_0))/cos(D)) \quad (5.56)$$

where

$$D = \frac{y'}{Rk_0} + \phi_0 \ \ (in\ radians) \quad (5.57)$$

and k_0 is the scale factor along the central meridian λ_0 which could be taken as 0.9996 for UTM projection. The origin for the zone is (ϕ_0, λ_0).

5.3.3.2 UTM Projection Based on Ellipsoidal Model

Conversion from a point location on the ellipsoidal surface to the rectangular coordinate of UTM projection can be done using Equations (5.58) and (5.59). After the conversion, easting and nothing values must be normalized using Equations (5.47) and (5.48) (Snyder, 1987).

$$x' = k_0 N[A + (1 - T + C)A^3/6 + (5 - 18T + T^2 + 72C - 58e'^2)A^5/120] \quad (5.58)$$

$$y' = k_0[M - M_0 + N\tan(\phi)[A^2/2 + (5 - T + 9C + 4C^2)A^4/24 + (61 - 58T + T^2 + 600C - 330e'^2)A^2/720] \quad (5.59)$$

$$k = k_0[1 + (1 + C)A^2/2 + (5 - 4T + 42C + 13C^2 - 28e'^2)A^4/24 + (61 - 148T + 16T^2)A^6/720] \quad (5.60)$$

where e^2 is the first eccentricity squared which can be calculated from Equation (5.2), e'^2 is the second eccentricity squared which can be calculated from Equation(5.3).

$$e'^2 = e^2/(1 - e^2) \quad (5.61)$$

$$N = a/(1 - e^2\sin^2(\phi))^{1/2} \quad (5.62)$$

$$T = \tan^2(\phi) \quad (5.63)$$

$$C = e'^2 \cos^2(\phi) \tag{5.64}$$

$$A = (\lambda - \lambda_0)\cos(\phi), \qquad with\ \lambda\ and\ \lambda_0\ in\ radians \tag{5.65}$$

$$\begin{aligned} M = a\Bigg[&\left(1 - \frac{e^2}{4} - \frac{3e^4}{64} - \frac{5e^6}{256} - \dots\right)\phi \\ &- \left(\frac{3e^2}{8} + \frac{3e^4}{32} + \frac{45e^6}{1024} + \dots\right) sin\,(2\phi) \\ &+ \left(\frac{15e^4}{256} + \frac{45e^6}{1024} + \dots\right)\sin(4\phi) \\ &- \left(\frac{35e^6}{3072} + \dots\right)\sin(6\phi) + \dots\Bigg] \end{aligned} \tag{5.66}$$

k may also be calculated as:

$$k = k_0[1 + (1 + e'^2 \cos^2(\phi))x^2/(2k_0^2N^2)] \tag{5.67}$$

Conversion from the rectangular coordinate of a point on UTM projection to the location on the ellipsoidal surface can be done using Equations (5.68) and (5.69). Before the conversion, false center coordinates must be calculated using Equations (5.47) and (5.48) in reverse (Snyder, 1987).

$$\begin{aligned} \phi = \phi_1 - (N_1\tan(\phi_1)/R_1)[&D^2/2 \\ &- (5 + 3T_1 + 10C_1 - 4C_1^2 - 9e'^2)D^4/24 \\ &+ (61 + 90T_1 + 298C_1 + 45T_1^2 - 252e'^2 \\ &- 3C_1^2)D^6/720] \end{aligned} \tag{5.68}$$

$$\begin{aligned} \lambda = \lambda_0 + [&D - (1 + 2T_1 + C_1)D^3/6 \\ &+ (5 - 2C_1 + 28T_1 - 3C_1^2 + 8e'^2 + 24T_1^2)D^5 \\ &/120]/\cos(\phi_1) \end{aligned} \tag{5.69}$$

where ϕ_1 is the "footpoint latitude" or the latitude at the central meridian which has the same y coordinate as that of the point (ϕ, λ), e^2 is the first eccentricity squared which can be calculated from Equation (5.2), e'^2 is the second eccentricity squared which can be calculated from Equation (5.3).

where

$$\phi_1 = \mu + \left(\frac{3e_1}{2} - \frac{27e_1^3}{32} + \dots\right)\sin(2\mu) + \left(\frac{21e_1^2}{16} - \frac{55e_1^4}{32} + \dots\right)\sin(4\mu) + \left(\frac{151e_1^3}{96} + \dots\right)\sin(6\mu) + \left(\frac{1097e_1^4}{512} - \dots\right)\sin(8\mu) + \cdots \tag{5.70}$$

and

$$e_1 = [1 - (1 - e^2)^{\frac{1}{2}}]/[1 + (1 - e^2)^{\frac{1}{2}}] \tag{5.71}$$

$$\mu = M/[a(1 - e^2/4 - (3e^4)/64 - (5e^6)/256 - \ \dots\ )] \tag{5.72}$$

$$M = M_0 + y'/k_0 \tag{5.73}$$

$$e'^2 = e^2/(1 - e^2) \tag{5.74}$$

$$C_1 = e'^2 \cos^2(\phi_1) \tag{5.75}$$

$$T_1 = \tan^2(\phi_1) \tag{5.76}$$

$$N_1 = \frac{a}{(1 - e^2 \sin^2(\phi_1))^{\frac{1}{2}}} \tag{5.77}$$

$$R_1 = \frac{a(1 - e^2)}{(1 - e^2 \sin^2(\phi_1))^{\frac{3}{2}}} \tag{5.78}$$

$$D = x'/(N_1 k_0) \tag{5.79}$$

CHAPTER 6

PREPARATION OF INPUT DATA

For the preparation of required input data to the solver, a user-friendly software which is named as MetuMap is developed based on object-oriented programing and written in C# language. The software uses geographical calculation methods explained in Chapter 5. Using this software, topography and satellite imagery for the solution area can be prepared easily. Image processing, interpolation, mesh placing and catchment area detection techniques used by the software are explained in this chapter. The program consists of two main modules.

6.1 Modules and User Interfaces

User interface of the first module named as Mesh Generator is shown in Figure 6.1.

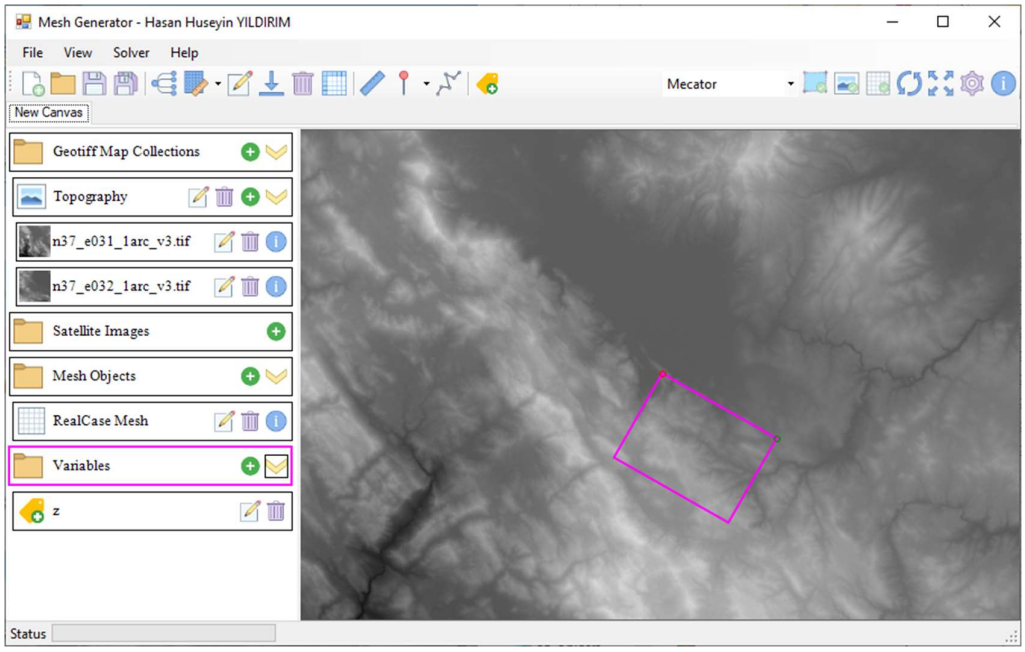

Figure 6.1 User interface of Mesh Generator module.

The Mesh Generator module is used for creating a two-dimensional mesh and placing that mesh on the map. After importing the required DEM (Digital Elevation Map) to the program, user can place mesh on the topographic map and check, modify its location and size visually.

As shown in Figure 6.1, file, view, solver and help buttons are provided at the top of the user interface. These buttons open a list of options to choose from. File button serves options for opening a new project, opening an existing project or saving the current project. As the data used in this program requires large storage, the projects are only stored as linked data packages. When a saved project is opened again the program looks for original data source files and processes these files at the beginning. View button serves options for changing visualization settings. Using view button user can change color grading method, projection method and other options that are used by the software for image processing. Solver and help buttons give required information to the user about the software. Also, at the top of the user interface there are a bunch of buttons. Using these buttons, user can change projection style, on-off satellite image, on-off grid, take simple measurements and place important locations on the map.

There is an organization section at the left side of the window. In this organization section, there are 4 different folders by default. These folders are GeoTiff Map Collections, Satellite Images, Mesh Objects and Variables. Using these sections, user can create new map collections and import relevant data files under these collections, import satellite images, create meshes and create variables linked to map collections.

After placing the computational mesh on the map, user can press mesh detail button which is placed at the top. Then, program opens the second module which is named as Mesh Detail shown in Figure 6.2. In this module, user can define the catchment area and outlet cells of the mesh. Cell type information is required in the solver to imply the boundary conditions on the boundary cells and describe the solution area.

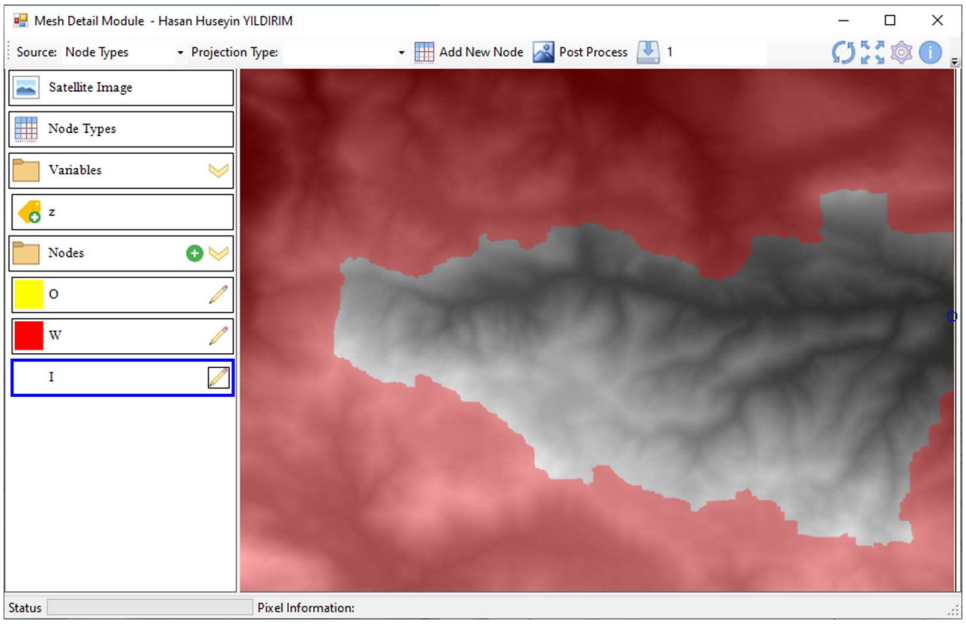

Figure 6.2 User interface of Mesh Detail module.

6.2 Data

Point data in geographical information systems can be specified in three main types in terms of storage and process technique of the data. The first data type is the point cloud data includes all point data samples together in a package without any order and without any standard. Raw versions of most of the satellite-based data are in point cloud data. This type of data must be checked for anomalies and reorganized to create useful data packages. The second data type is vector data. It is used to store point locations in order as a path. It is generally used to store a path or bounds of a closed area. The third one is raster or grid data. This data type stores evenly spaced and regular data. The GeoTiff DEM's used in this thesis is a grid data, stores evenly spaced elevation information.

In the programming side of the software, there are two types of map definitions. The first one is the data map and the second one is the satellite image map. These two map styles contain locational information. All locational information and data are gathered from GeoTiff files using the Bitmricle LibTIFF library which is freely

available and open-source library generally used to process TIFF images. The library allows the program to read the data from GeoTiff file format.

As an image map, satellite imagery stores an image beside the locational information. On contrary to satellite imagery, data map stores only the data besides locational information. This data is used to generate an image. In this example shown in Figure 6.1, the data sets loaded in the program include topographic information and elevation values at each pixel. The program uses a two-dimensional single-precision floating-point variable to save the data at each pixel. Then uses this variable to generate greyscale or colorful image based on the magnitude of the values stored in variable.

6.2.1 Digital Elevation Maps

For preliminary readiness, topographic data must be prepared. For topographic data, DEM is required. DEM data commonly formatted to a GeoTiff. This file format contains locational information and elevation values. GeoTiff file consists of metadata and data sections.

- In the metadata section, origin location, datum information, the physical size of the map and the image, and bit depth of the data is stored. The program uses this information to locate the map on the screen using projection techniques explained in Chapter 5.
- In the data section, all the data is stored in IJ ordered binary form. This data is read by using the bit depth gathered from the metadata section and converted to a floating-point variable array.

Note that, topography data in GeoTiff format actually is not a true 3D shape. It only stores evenly distributed scalar quantities at each pixel of the image, and this information is used to create a single layer of surface as elevation at locations. Shapes that require more than one layer of information like caves, tunnels under the surface or bridges on the surface cannot be stored in this format.

Greyscale colored example of a GeoTiff file is shown in Figure 6.3. In the figure, brighter sections indicate higher elevations. Each pixel color is scaled from white to black from maximum elevation to minimum elevation.

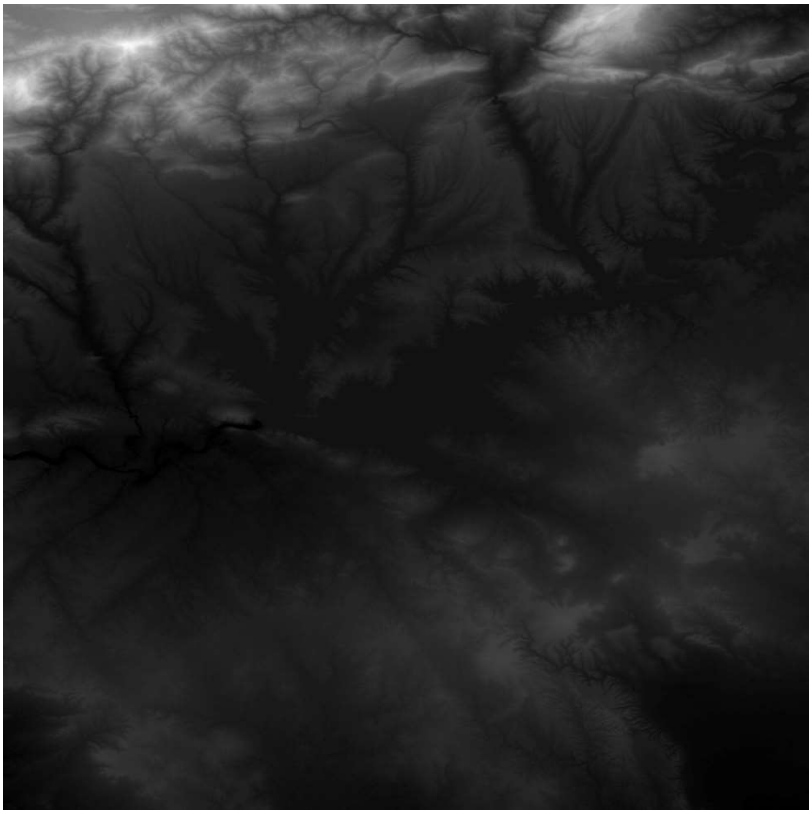

Figure 6.3 Example GeoTiff topographic data from Aster global DEM (N37E38). The area in between 37^{o} and 38^{o} parallels and between 38^{o} and 39^{o} meridians is included. Data is converted to greyscale image.

6.2.1.1 Color Grading for DEM

Color grading methods are used for the visualization of the digital elevation maps. Using color grading methods, each nodal data is mapped into a color palette using linear interpolation and image processing techniques. Color palettes used in this software and output images for a sample data package are shown in Figure 6.4 .

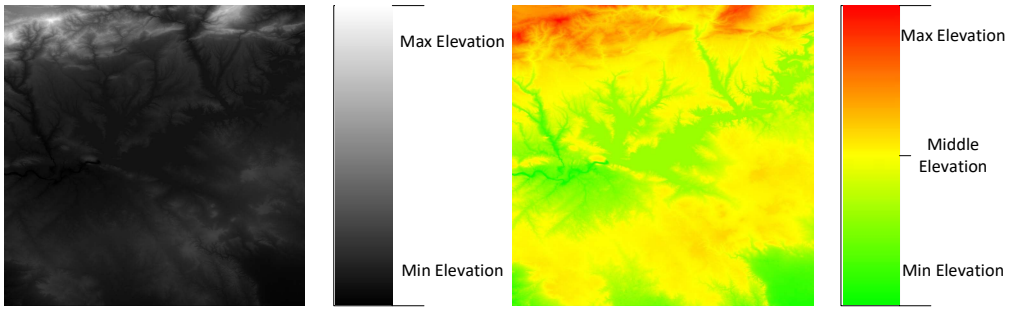

Figure 6.4 Greyscale and green to red color grading.

6.2.1.2 Data Sources for DEM

ASTER Global Dem: Data packages can be downloaded at Earth Data web page. Specification and validation reports can also be found at the product web page. Data packages have portioned into 1°x1° (degree), 1984 World Geodetic System (WGS84) coordinates (latitude, longitude), and stored in 3601x3601 pixel GeoTiff file. Horizontal accuracy is 1 arc-second (~30 m at the equator).

STRM 1 arc-second Global: Supplied by United States Geological Survey (USGS). Data packages can be downloaded at Earth Explorer web page. This data has portioned to 1°x1° sub-maps in resolution of 1 arc-second by 1 arc-second between 50^0 north and 50^0 south parallels, above 50° north and below 50° south latitude 2 arc-second by 1 arc-second and stored in 3601x3601 pixel GeoTiff file.

Some other high-resolution datasets are available up to 12.5m supplied by space agencies. However, these datasets are not used in the scope of this thesis.

6.2.2 Satellite Image

Satellite images for the solution area can be imported to the software. These satellite images are used to allow the user to visually check the location of the mesh. Also, the satellite maps can be used to create land cover map, which includes the land cover information (asphalt, concrete, sand, grass, stone etc.) for solution area using image

processing techniques. Than the surface roughness values for the solution area can be estimated from the land cover maps by decomposing area into different land cover materials and setting roughness values for materials. In this thesis, the solutions are prepared using constant surface roughness. In future work, this option will be improved and used in the solutions. User can directly import surface roughness map to the software and gather surface roughness information. However, this option is not used in real solution cases because of practical reasons.

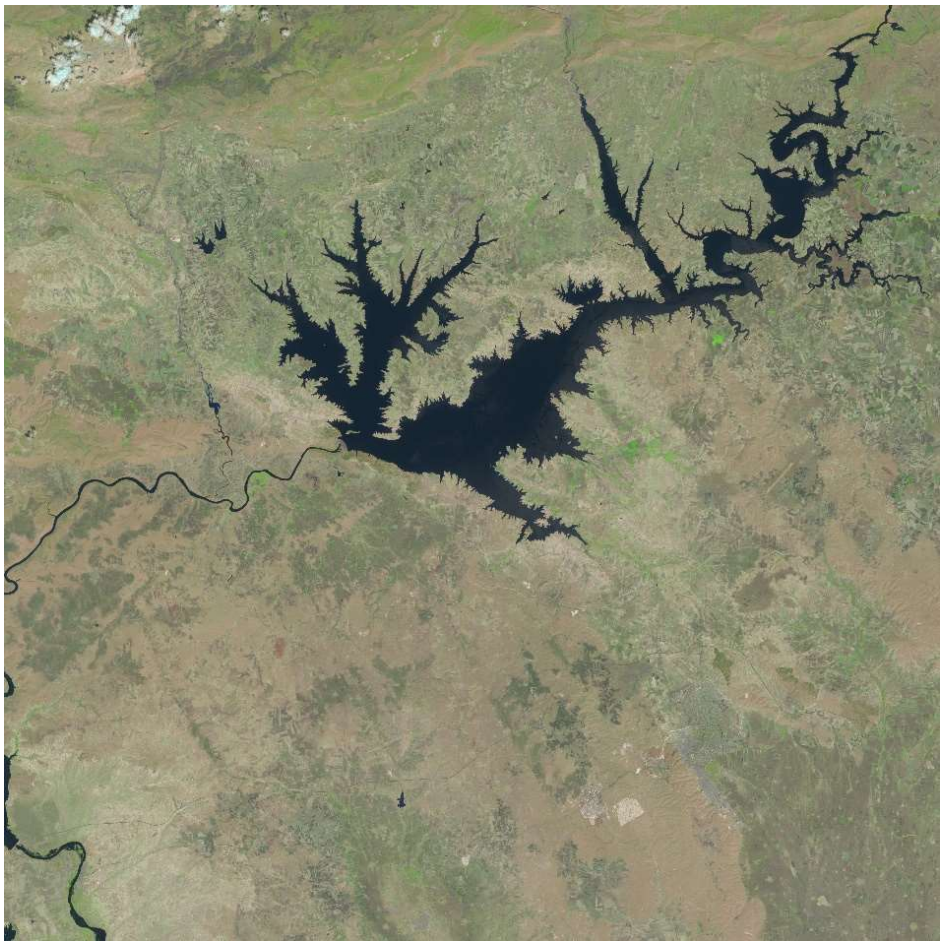

Figure 6.5 Example satellite image from the European Space Agency (ESA) Sentinel-2 Dataset.

6.3 Locating the Mesh

In order to prepare the required inputs for the solver, data points in the Cartesian coordinates of the mesh must be gathered from geographically located data. For this purpose, geographical coordinates must be converted to the Cartesian coordinates or vice versa.

6.3.1 Cartesian Coordinate System

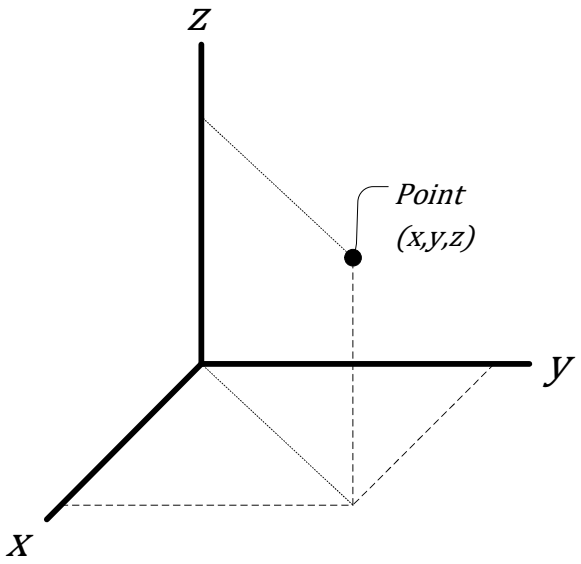

Figure 6.6 Cartesian Coordinate System

The Cartesian coordinate system is a three-dimensional system. All dimensions are perpendicular to each other. In order to specify a point in Cartesian coordinates, the distances from origin must be known for all dimensions.

6.3.2 Conversion Techniques Between Coordinate Systems

As gravity directs to the center of the globe in the geographical model, and in Cartesian coordinates, the gravity force acts only in negative z-direction. The z-

direction in Cartesian coordinates and the perpendicular distance from the surface of the geographical model can be used as the common dimension. Moreover, measurements on that common dimension is already in length so that there is no need for conversion on that dimension. The other two dimensions are the latitude and the longitude of the horizontal location and must be converted from the surface of the geographic model to a flat plane.

In this thesis, two different methods are used for the conversion between geographical location and the Cartesian coordinate system. Fist method is the usage of the rectangular coordinates that came from the projection, and the second method is the usage of a local tangent plane. A perfect conversion between geographic locations and Cartesian coordinates is impossible because of the shape of the Earth, both of these methods have some imperfections.

6.3.2.1 Usage of Rectangular coordinates as x-y plane

All of the projection techniques are applied to convert the surface of the globe as accurately as possible on a 2D flat surface. This flat surface (rectangular coordinates) can be used as the x-y plane of the mesh in Cartesian coordinates. In this type of conversion, the projection equations are used for conversion between geographic and rectangular coordinates, and simple trigonometry is used to find rectangular coordinates of all nodes in the computational mesh system. In this thesis, Universal Transverse Mercator projection is used for this purpose

$$d = \sqrt{{x'_A}^2 + {y'_A}^2} \tag{6.1}$$

$$\theta = \arctan\left(\frac{y'_A}{x'_A}\right) - Bearing\ Angle \tag{6.2}$$

$$x_A = x_c + d\cos(\theta) \tag{6.3}$$

$$y_A = y_c + d\sin(\theta) \tag{6.4}$$

where (x_c, y_c) are the rectangular coordinates of the local center for mesh, (x'_A, y'_A) are the local coordinates of an internal point and (x_A, y_A) are the rectangular coordinates of that internal point. The rectangular coordinate of an internal point on the mesh can be found from Equations (6.3) and (6.4) by using the rectangular coordinate of the center location, bearing angle, and dimensions of the mesh. After the calculation of the rectangular coordinate, the inverse formulation for the projection can be applied to convert that rectangular coordinate to the geographical location.

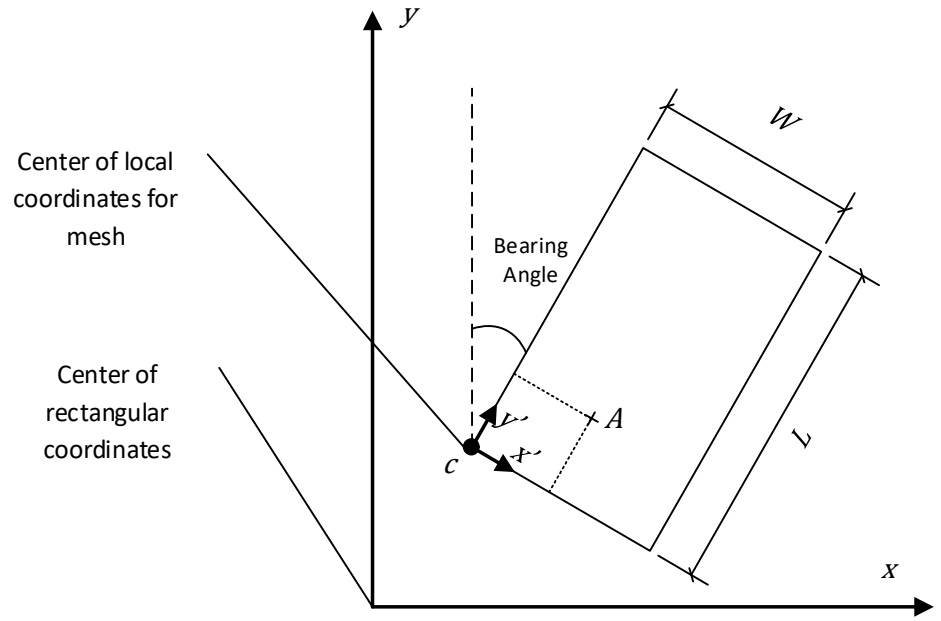

Figure 6.7 Mesh in rectangular coordinates

6.3.2.2 Usage of Local Tangent Plane

Local tangent plane is a flat surface plane tangent at a point on the surface of the model. It can be used to convert the system from the geographic coordinates to Cartesian coordinates, in the similar manner as in the method of azimuthal projection which is used to project the surface of the model to a flat surface. Instead of

projecting all surface, this method aims to choose the locations internal points of the mesh at the correct distance to the tangent point.

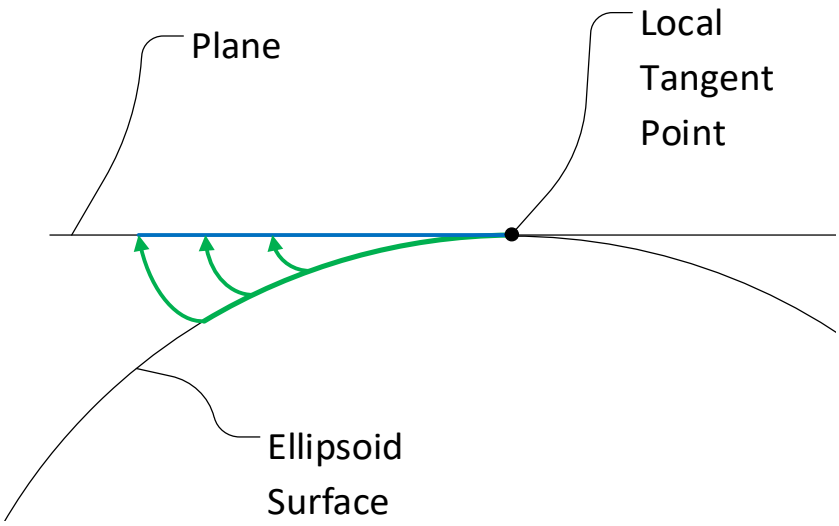

Figure 6.8 Local Tangent Plane

As can be seen in Figure 6.8, This tangent point is the common point between geographic and the Cartesian system. By using that local tangent point, location of any other point can be found from the relative distance and bearing angle from that tangent point, as shown in Figure 6.9. In order to minimize the error in conversion, this point can be selected at the area center of the mesh. From that center point, locations of all internal points can be calculated by using destination point algorithms explained in second chapter.

Distance from the local tangent point and bearing angle can be found from Equations (6.5) and (6.6) using the local coordinates of the local tangent point, bearing angle, and dimensions of the mesh.

$$d = \sqrt{(x'_A - x'_c)^2 + (y'_A - y'_c)^2} \tag{6.5}$$

$$\theta = \arctan\left(\frac{(y'_A - y'_c)}{(x'_A - x'_c)}\right) - Bearing\ Angle \tag{6.6}$$

where (x'_c, y'_c) is the local coordinate of the local tangent point, (x'_A, y'_A) is the local coordinate of an internal point. After this calculation geographic location of that internal point can be calculated from destination point formulation using Equations (5.5) and (5.6).

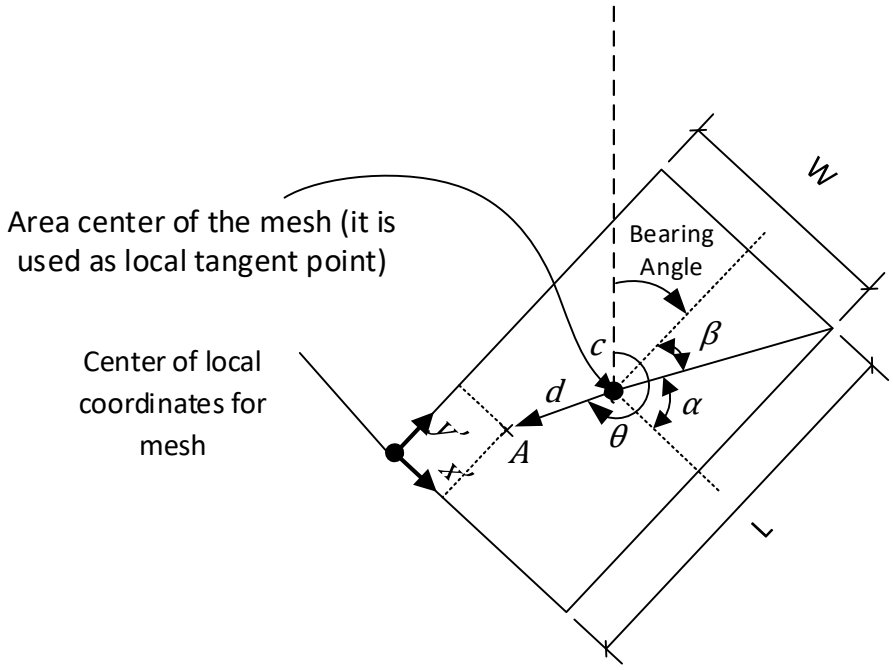

Figure 6.9 Mesh on the local tangent plane

In this method, if the length/width ratio is too far from 1, the area is too large or has uneven shape, multiple tangent points can be used for the calculations. Rectangular coordinates of that area can be obtained accurately using multiple local tangent planes. However, as each local tangent point is only center for its own calculation area. It must be known that, intersections of that planes must be corrected from each neighbor's tangent point. Each tangent point must give the same location for all points at intersections. As this is impossible because of the shape of the earth, location of these points must be chosen by taking the location that leads smallest error. Also, calculations used in this conversion is valid only for the spherical earth model which also introduces some errors.

6.3.3 Interpolation from DEM at Internal Point

After placing the mesh to a suitable location with right angle and finding the locations of all internal points of the computational mesh, interpolation must be done to get the data for all required nodal points. As seen in Figure 6.10, locations of data points and locations of computational mesh grid points do not have to be perfectly matched. Also, solution area may require bearing angle for better placement or for excluding the unnecessary places from the mesh. So that, in order to get the data values at mesh points two-dimensional interpolation must be performed.

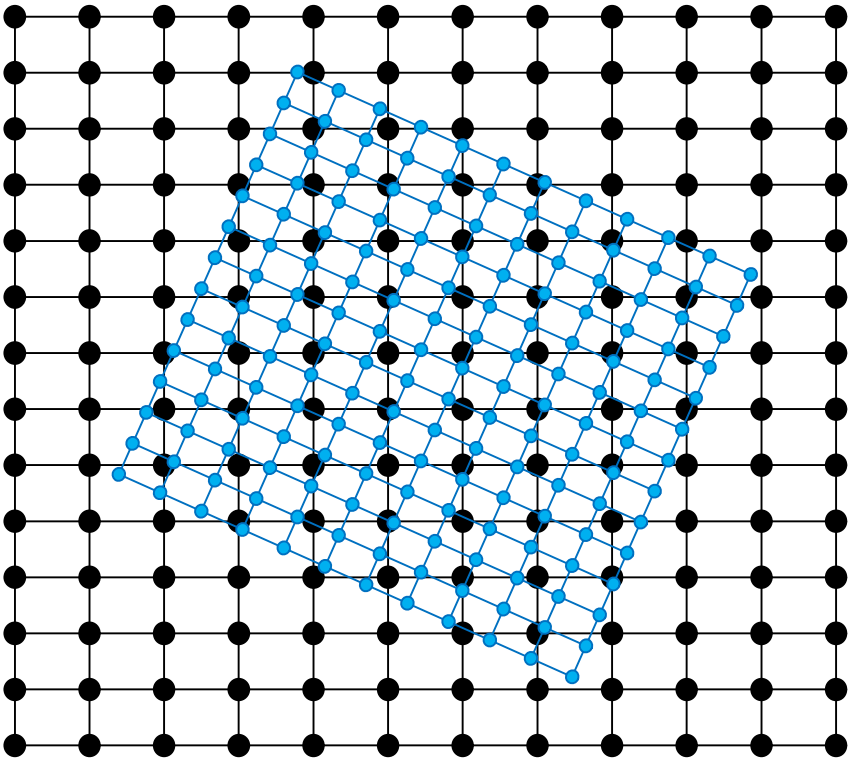

Figure 6.10 Sample data grid and computational mesh grid. Black dots represent the data points and blue dots represents mesh grid points.

There are three simple ways to interpolate a value on 2D plane. The first one is the nearest neighbor value that is simply taking the closest value. The second one is the bilinear and the third one is the bicubic interpolation. As shown in Figure 6.11, in bilinear interpolation, value for an internal point can be calculated by interpolating

the value from 4 data points linearly in x and then in y directions respectively. In bicubic interpolation, this process is done by using 3rd order approximation from 16 points (4 by 4 points includes neighbor's neighbors). The software in this thesis uses only bilinear interpolation technique.

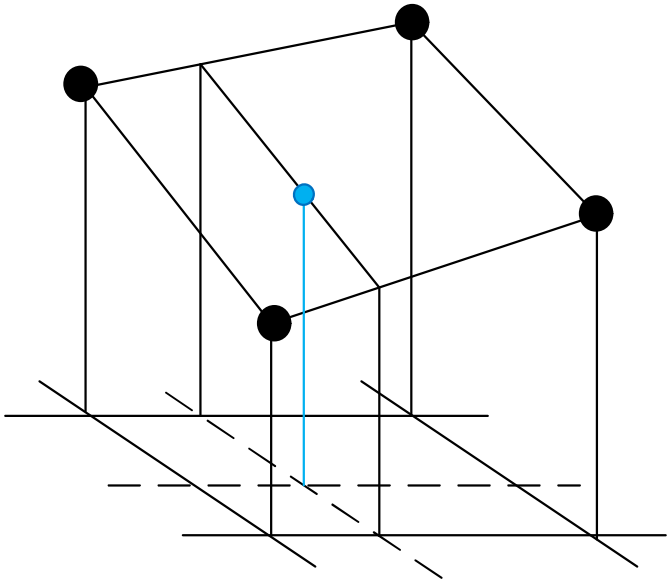

Figure 6.11 Bilinear interpolation

6.3.4 Determination of Catchment Area, Crest Line and Thalweg

In order to define the river basin, topographic model is used. Three characteristics of the basin can be described. The first one is the catchment area which defines the area that discharges its water to same outlet. The second one is the crest line as the boundary of catchment area. Both sides of the crest line discharge rain water into neighboring basins. Third one is the thalweg line of the main river and sub-channels required to perform channel flow computations. However, channel flow computations will not be performed in this study.

In a grid system when fluxes across the cell faces are integrated, all cells must satisfy the continuity equation by discharging the water to a neighbor. As the flow over the land surface has a strong dependence with the slope of the surface, flow direction and distribution of among the faces of a cell can be determined from the slopes of the ground surface.

For the detection of the catchment area, crest line and thalweg line, an algorithm that estimates flow direction at cells is developed and named as Catchment Area Detection algorithm (CAD). This algorithm finds the boundaries of the catchment area automatically.

As the ground shape of the domain may include lots of local minimums, the algorithm firstly must fill the cavities and find the possible discharge point of these cavities by defining a theoretical water surface level. As nodes other than boundaries need to discharge its water to another node, when a node is a local minimum (all of the neighbors have greater value), algorithm increases its theoretical water surface level to 0.01m higher than the neighbor's minimum water surface level until all of the local cavities filled and discharges its water. Then CAD algorithm uses this theoretical water surface level to define the outer boundaries of the catchment and the thalweg line by deciding the flow direction at cells.

Interior points are saved as interior nodes, exterior points (outside of the crest line) are saved as wall boundary and interior points at the borders of the area are saved as outlet boundary for the solver.

At the beginning, user should mark the outlet of the domain as shown in Figure 6.12. In Figure 6.12, yellow strip is defined by user as outlet of the domain and half-transparent reddish area is by default exterior. Then the algorithm looks for new interior points by comparing the theoretical water surface elevations of the neighbors and finds the crest line as the boundary of the catchment. This algorithm runs repeatedly for all of the points in the domain until there is no change in point definitions. Catchment area found by software is shown in Figure 6.13.

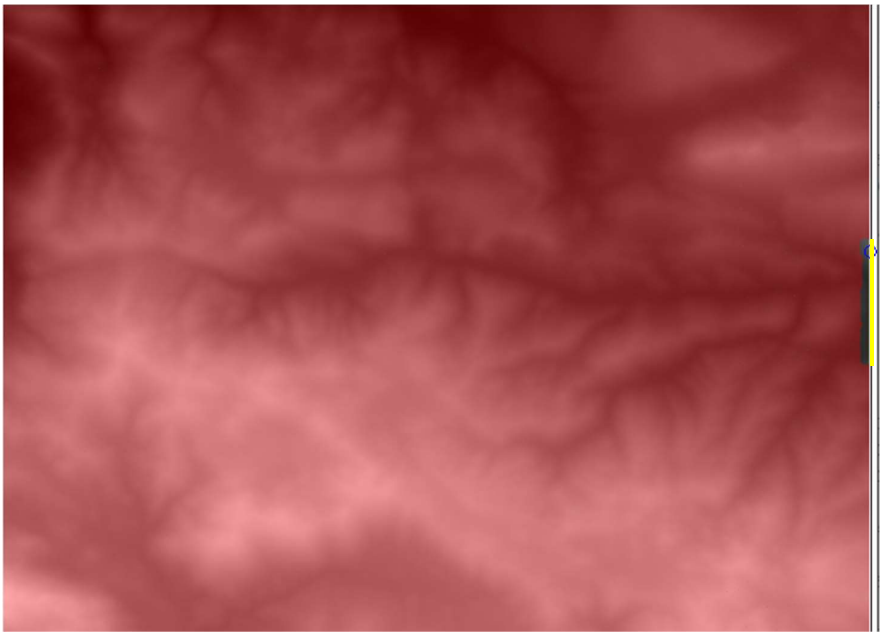

Figure 6.12 User initialization of outlet for catchment area definition.

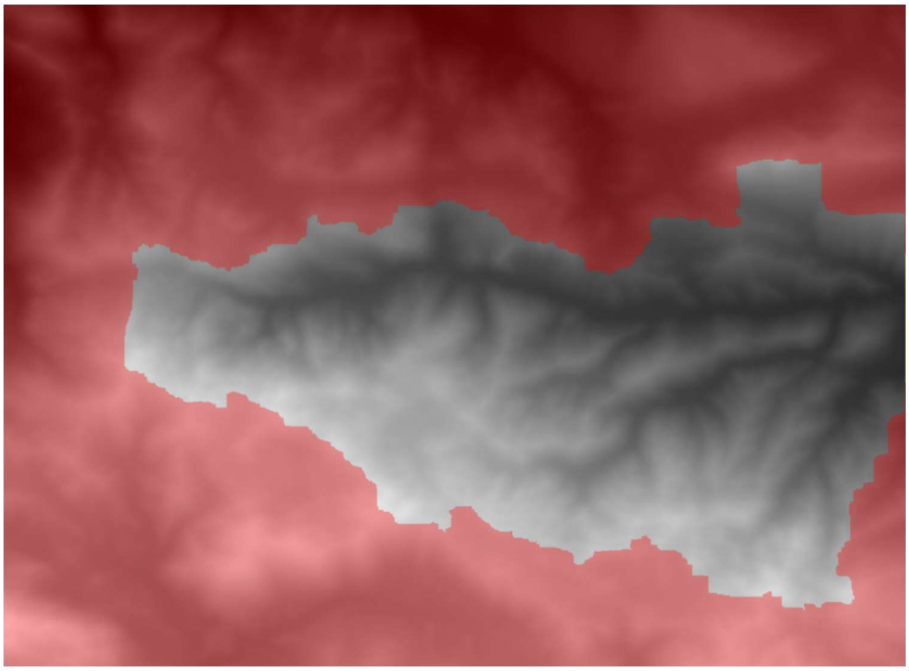

Figure 6.13 Catchment area found after search iterations of the CAD algorithm

CHAPTER 7

REAL CASE SOLUTION

A part of the Çarşamba River basin at Konya Bozkır is studied as a real test case model. The river overflowed on the date of 15th December 2010. The flood event led to damage on Bozkır shire and the villages around the Bozkır. (Buldur & Sarı (2012) indicated that the flood has resulted from the intensive rainfall event right after the snowfall and design of the hydraulic structures were not sufficient to prevent from the damage.

7.1 Location of Study Area

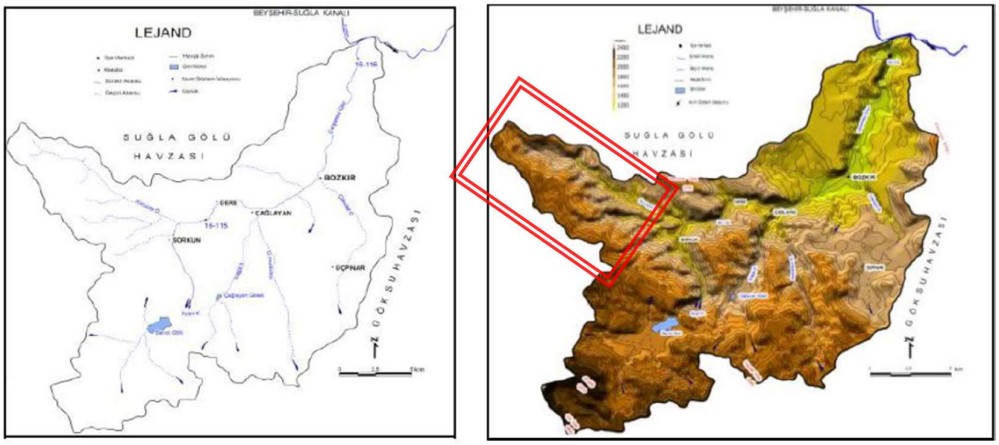

Figure 7.1 Hydrological and topographic map of the Çarşamba River basin (Buldur & Sarı, 2012).

Hydrological and topographic map of the basin of the river is shown in Figure 7.1. The solution area in this analysis is roughly placed on the figure as a red rectangular domain. Study area is a mountainside and the elevations are changing between 2110 to 1080.

The solution area is 15000 m by 11000 m rectangle, and the total physical area of the domain is 165 km^2. Area center of the mesh is located at 37.193 latitude and 32.056 longitude, and the mesh is placed with 30^0 bearing angle. Digital elevation model for the study area is given in Figure 7.2. This elevation model is gathered from the SRTM 1-arc second global DEM data source.

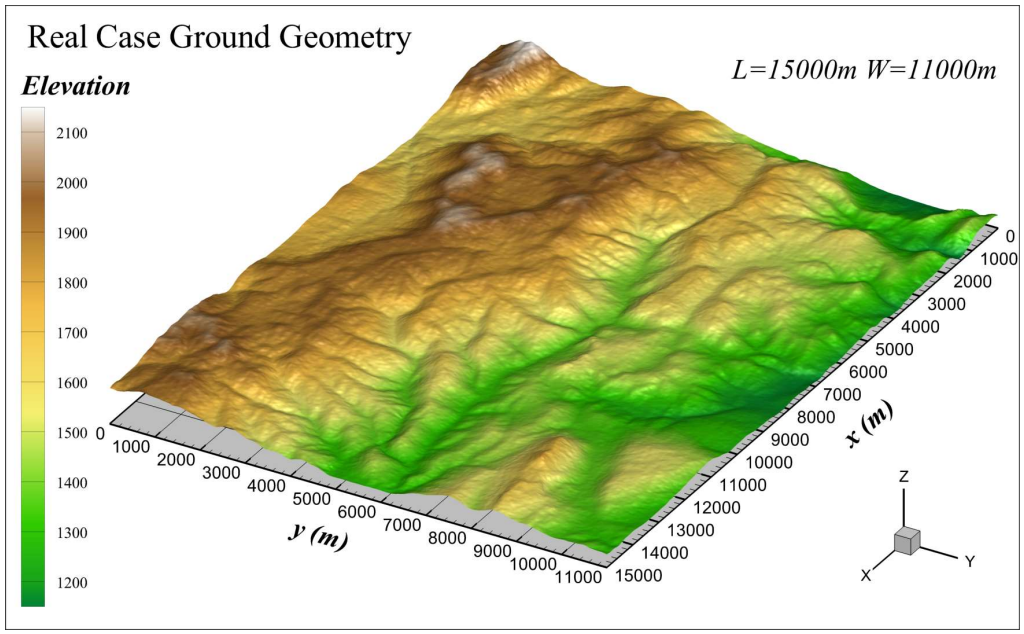

Figure 7.2 Digital elevation model of the study area.

7.2 Catchment Area

Catchment area for the domain is obtained using the methods described in the previous chapter. The catchment area for this basin is shown in Figure 7.3, and it covers about 60 km^2.

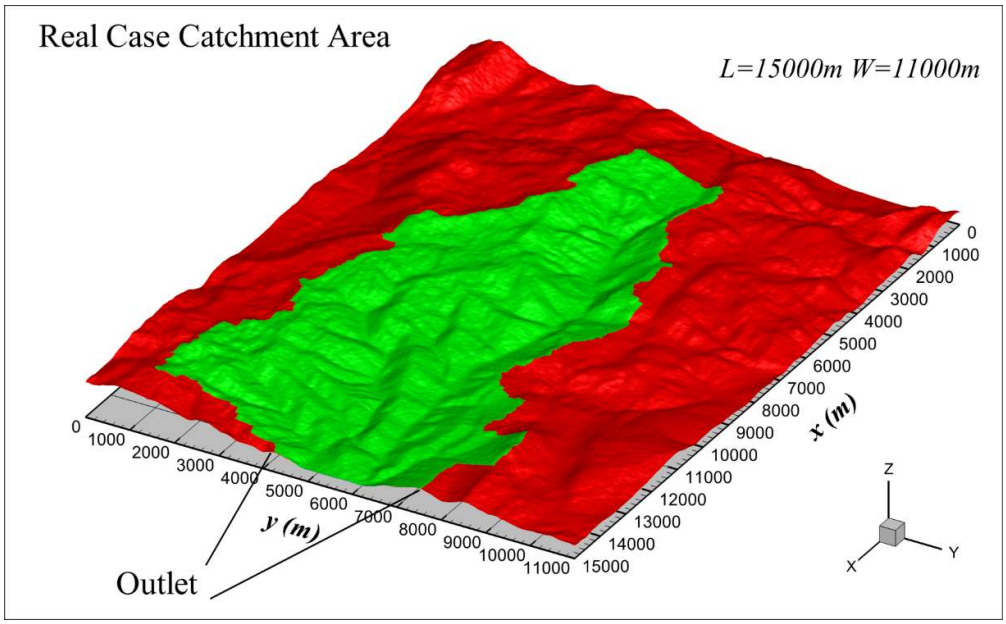

Figure 7.3 Catchment area.

7.3 Results

Two different solutions are obtained. The first solution uses the catchment area only, and the second solution is obtained using all nodes of rectangular domain.

These two solutions are started at the same time and solved with 24 threads each in parallel. The first solution took about 4.7 hours and the second solution took about 7 hours.

The spatial mesh size used is $dx = dy = 10\ m$ and the time step size is $dt = 1.0E - 2s$. The mannings roughness parameter assumed to be uniform over the domain and fixed as $n = 0.02$. The catchment area is exposed to 1 hour duration uniform heavy rain ($I = 2.7E - 5\ m/s$) and simulation is continued for three hours.

Outflow hydrograph for this solution shows that the catchment area algorithm is suitable in these kind of solutions to eliminate unnecessary places from the solution. Combined solver is suitable for the solution over natural terrain.

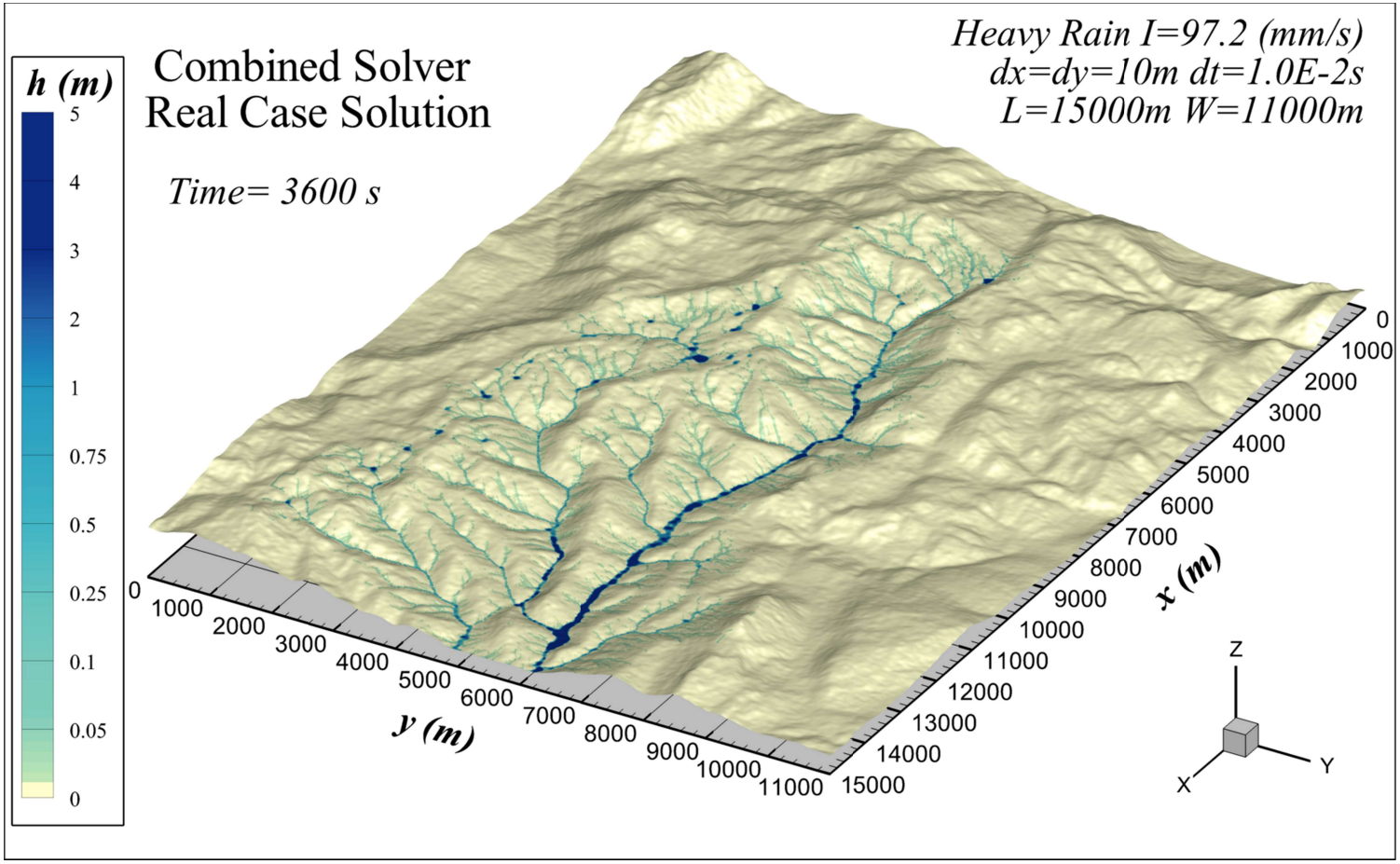

Figure 7.4 Real case solution using only the area defined as interior by the catchment area algorithm.

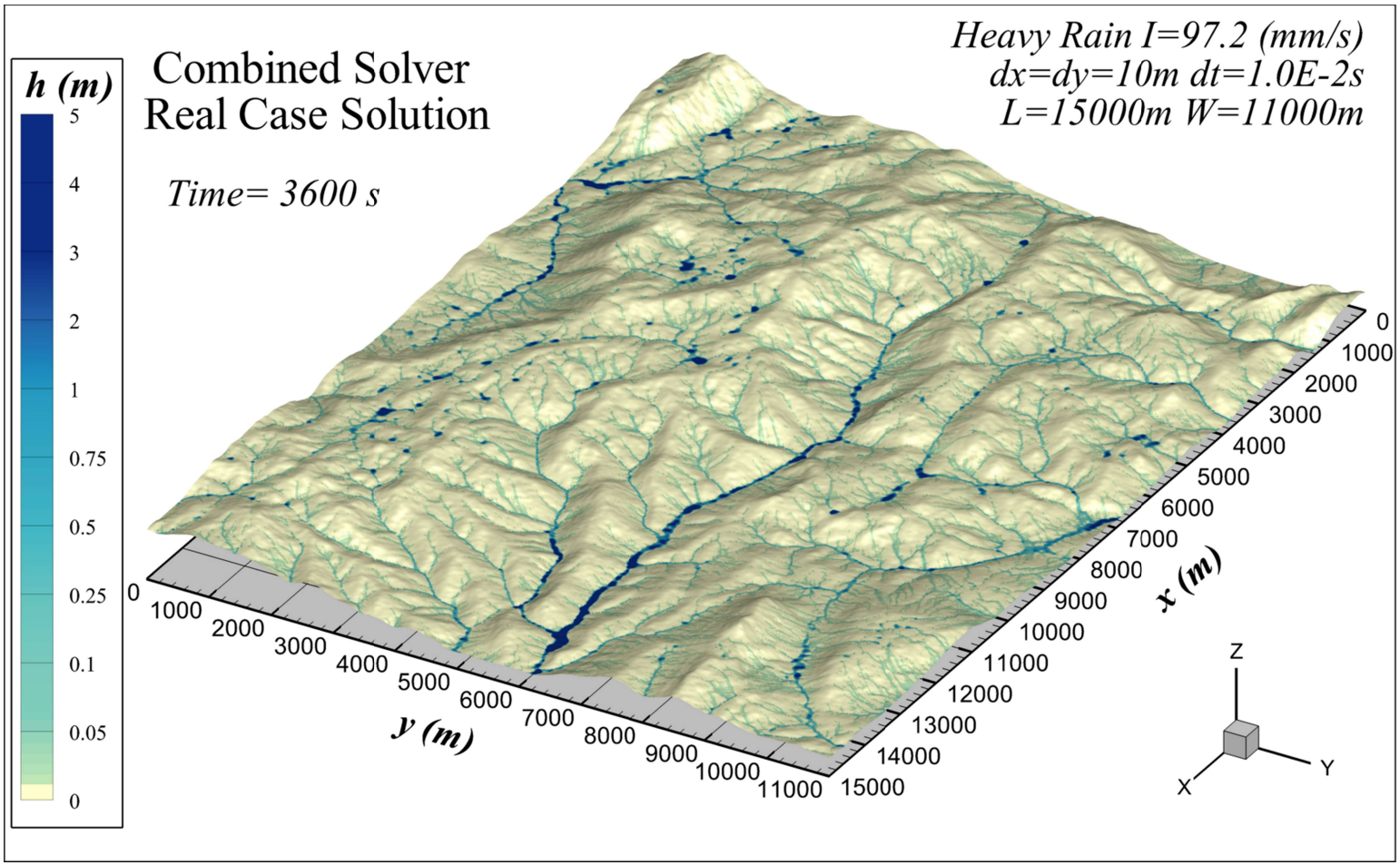

Figure 7.5 Real case solution using all the area defined as interior.

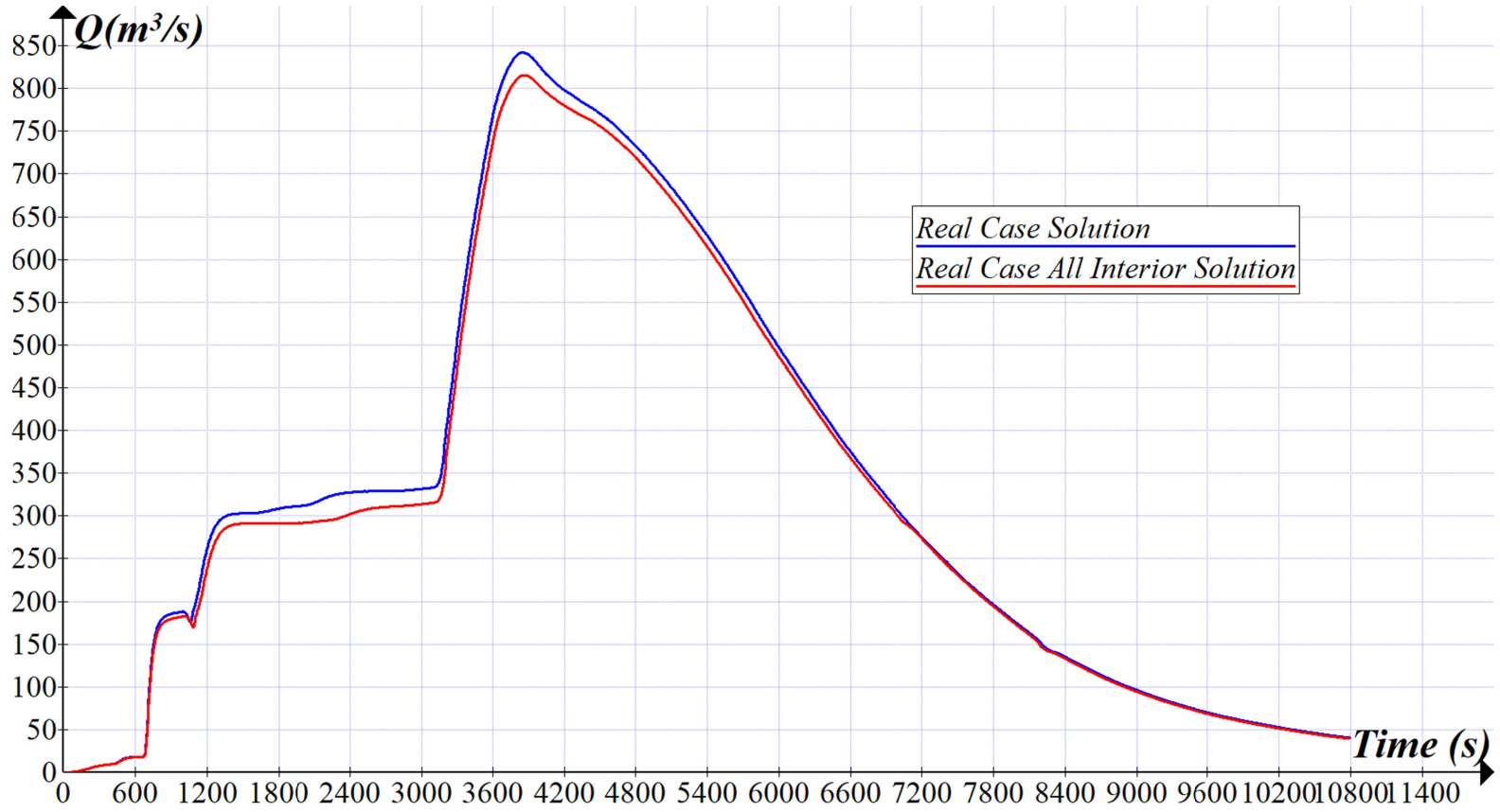

Figure 7.6 Outlet hydrograph of real case solution .

CHAPTER 8

CONCLUSIONS AND RECOMMENDATIONS

A two-dimensional kinematic wave equation solver is developed to compute surface runoff from a fully distributed model. The model solves the continuity equation assuming equilibrium of resistance and gravity forces as a fully developed uniform flow all over the domain regardless of bed geometry and water depth. Thus, it is suitable for small water depths over large two-dimensional catchment areas.

A software module named as Mesh Generator is developed to extract Digital Elevation Models (DEM) from available open-source satellite data. The data from geographical coordinates is transformed to cartesian coordinates to form a computational grid. This module is used for the preparation of the input files from multiple or single satellite-based data.

Another computer module named as Mesh Detail is developed to describe boundaries of the catchment area. A modified version of this module can also be used to determine the Thalveg lines for possible streams in the domain of interest.

Solver is tested with analytical solutions and several 1D and 2D hypothetical cases. Flow around obstructions and flow into cavities with accumulation can easily be simulated. In all cases with different critical circumstances solver was able to generate stable and accurate solutions. Solution over 165 km^2 natural terrain is also obtained without any stability issue or any numerical anomaly.

The developed code is improved to run parallel on multicore workstations to reduce CPU requirements. From parallelization tests, it is observed that the parallelized version of the solver is also stable and highly scalable. The solver can be used for analysis over large domains efficiently using powerful computers.

All solutions are obtained using effective rainfall intensity as a source term in the continuity equation. Empirical formulations for the calculation of infiltration, evaporation etc. are available in the literature. These empirical calculations can easily be adapted to the source term in the continuity equation to make more realistic hydrological modeling. In this thesis, these empirical calculations are not adapted as the main concentration of the study is the development of the methods rather than getting a solution.

Another important input for the solver is the manning roughness value. In this study, solutions are obtained using constant manning roughness value all over the domain. In real cases, this value depends on the land cover. While land cover material can be detected by the human eye, in order to make that process automatic, a software module can be developed to identify surface material from the satellite-based images using image processing techniques.

The kinematic wave modeling used in this study is appropriate for estimation of surface runoff in large domains for small water depths. When water accumulates, the assumption of equal resistance and gravity forces may not be valid, and complete momentum equations should be solved for streams formed in the catchment area. The code developed in this study can prepare input for such a complete dynamic model for the one-dimensional stream flows. Coupling this code with a 1D (or 2D)-streamflow solver may produce more realistic estimates of the time-dependent discharge hydrograph at the outlet of the basin.

REFERENCES

Akyürek, Z., & Şorman, A. Ü. (2002). Monitoring snow-covered areas using NOAA-AVHRR data in the eastern part of Turkey. *Hydrological Sciences Journal*, *47*(2), 243–252. https://doi.org/10.1080/02626660209492927

Bao, H., Wang, L., Zhang, K., & Li, Z. (2017). Application of a developed distributed hydrological model based on the mixed runoff generation model and 2D kinematic wave flow routing model for better flood forecasting. *Atmospheric Science Letters*, *18*(7), 284–293. https://doi.org/10.1002/asl.754

Buldur, A. D., & Sarı, S. (2012). Çarşamba Çayı'nın 15 aralık 2010 tarihli taşkını ve Bozkır'daki (Konya) etkisi. *Marmara Coğrafya Dergisi*, 81–107.

Chanson, H. (2004a). Turbulent dispersion and mixing: 1. Vertical and transverse mixing. In *Environmental Hydraulics of Open Channel Flows* (Issue c, pp. 81–98). Elsevier. https://doi.org/10.1016/B978-075066165-2.50039-4

Chanson, H. (2004b). Unsteady open channel flows: 1. Basic equations. In *Environmental Hydraulics of Open Channel Flows* (Issue Stoker 1953, pp. 185–222). Elsevier. https://doi.org/10.1016/B978-075066165-2.50044-8

Çiftçi, B. B., Kuter, S., Akyürek, Z., & Weber, G.-W. (2017). FRACTIONAL SNOW COVER MAPPING BY ARTIFICIAL NEURAL NETWORKS AND SUPPORT VECTOR MACHINES. *ISPRS Annals of Photogrammetry, Remote Sensing and Spatial Information Sciences*, *IV-4/W4*, 179–187. https://doi.org/10.5194/isprs-annals-IV-4-W4-179-2017

Eagleson, P. S. (1970). *Dynamic hydrology*. New York (N.Y.) : McGraw-Hill. http://lib.ugent.be/catalog/rug01:001323753

Fernández-Pato, J., Caviedes-Voullième, D., & García-Navarro, P. (2016). Rainfall/runoff simulation with 2D full shallow water equations: Sensitivity analysis and calibration of infiltration parameters. *Journal of Hydrology*, *536*,

496–513. https://doi.org/10.1016/j.jhydrol.2016.03.021

Grafarend, E. W., & Krumm, F. W. (2006). *Map Projections*. Springer Berlin Heidelberg. https://doi.org/10.1007/978-3-540-36702-4

Henderson, F. M., & M, H. F. (1966). *Open Channel Flow*. Macmillan. https://books.google.com.tr/books?id=4whSAAAAMAAJ

Jia, Y., Shirmeen, T., A. Locke, M., E. Lizotte Jr., R., & Douglas Shields Jr., F. (2019). Simulation of Surface Runoff and Channel Flows Using a 2D Numerical Model. In *Soil Erosion - Rainfall Erosivity and Risk Assessment*. IntechOpen. https://doi.org/10.5772/intechopen.80214

Kazezyılmaz-Alhan, C. M., & Medina, M. A. (2007). Kinematic and Diffusion Waves: Analytical and Numerical Solutions to Overland and Channel Flow. *Journal of Hydraulic Engineering*, *133*(2), 217–228. https://doi.org/10.1061/(ASCE)0733-9429(2007)133:2(217)

Lambert, W. D. (1942). The distance between two widely separated points on the surface of the earth. *Journal of the Washington Academy of Sciences*, *32*(5), 125–130. http://www.jstor.org/stable/24531873

Li, T., Wang, G., Chen, J., & Wang, H. (2011). Dynamic parallelization of hydrological model simulations. *Environmental Modelling & Software*, *26*(12), 1736–1746. https://doi.org/10.1016/j.envsoft.2011.07.015

Miller, J. E. (1984). Basic concepts of kinematic- wave models. *US Geological Survey Professional Paper*, *1302*. https://doi.org/10.3133/pp1302

Mu, A. (2013). Ecohydraulics. In I. Maddock, A. Harby, P. Kemp, & P. Wood (Eds.), *Climate Change 2013 - The Physical Science Basis* (Vol. 53, Issue 9). John Wiley & Sons, Ltd. https://doi.org/10.1002/9781118526576

Singh, J., Altinakar, M. S., & Ding, Y. (2011). Two-dimensional numerical modeling of dam-break flows over natural terrain using a central explicit scheme. *Advances in Water Resources*, *34*(10), 1366–1375.

https://doi.org/10.1016/j.advwatres.2011.07.007

Singh, J., Altinakar, M. S., & Ding, Y. (2015). Numerical Modeling of Rainfall-Generated Overland Flow Using Nonlinear Shallow-Water Equations. *Journal of Hydrologic Engineering*, *20*(8), 04014089. https://doi.org/10.1061/(ASCE)HE.1943-5584.0001124

Snyder, J. P. (1987). Map projections: A working manual. In *Professional Paper*. https://doi.org/10.3133/pp1395

Tekeli, A. E., Akyürek, Z., Şorman, A. A., Şensoy, A., & Şorman, A. Ü. (2005). Using MODIS snow cover maps in modeling snowmelt runoff process in the eastern part of Turkey. *Remote Sensing of Environment*, *97*(2), 216–230. https://doi.org/10.1016/j.rse.2005.03.013

Veness, C. (2002). Calculate Distance and Bearing between Two Latitude/Longitude Points Using Haversine Formula in JavaScript. In *MIT Open Source* (pp. 1–39). https://www.movable-type.co.uk/scripts/latlong.html

Wang, L.-L., Chen, D.-H., Li, Z.-J., & Zhao, L.-N. (2011). Coupling Green-Ampt infiltration method and two-dimensional kinematic wave theory for flood forecast in semi-arid catchment. *Hydrology and Earth System Sciences Discussions*, *8*(4), 8035–8061. https://doi.org/10.5194/hessd-8-8035-2011

NASA/METI/AIST/Japan Spacesystems, and U.S./Japan ASTER Science Team (2009). ASTER Global Digital Elevation Model [Data set]. NASA EOSDIS Land Processes DAAC. Accessed 2020-08-21 from https://doi.org/10.5067/ASTER/ASTGTM.002

USGS. Shuttle Radar Topography Mission (SRTM) 1 Arc-Second Global [Data set]. USGS EROS Archive. Accessed 2020-08-21 from https://doi.org/10.5066/F7PR7TFT

ESA. Sentinel-2 [Data set]. USGS EROS Archive. Accessed 2020-08-21 from https://doi.org/10.5066/F76W992G